INFORMATION TO USERS

This manuscript has been reproduced from the microfilm master. UMI films the text directly from the original or copy submitted. Thus, some thesis and dissertation copies are in typewriter face, while others may be from any type of computer printer.

The quality of this reproduction is dependent upon the quality of the copy submitted. Broken or indistinct print, colored or poor quality illustrations and photographs, print bleedthrough, substandard margins, and improper alignment can adversely affect reproduction.

In the unlikely event that the author did not send UMI a complete manuscript and there are missing pages, these will be noted. Also, if unauthorized copyright material had to be removed, a note will indicate the deletion.

Oversize materials (e.g., maps, drawings, charts) are reproduced by sectioning the original, beginning at the upper left-hand corner and continuing from left to right in equal sections with small overlaps. Each original is also photographed in one exposure and is included in reduced form at the back of the book.

Photographs included in the original manuscript have been reproduced xerographically in this copy. Higher quality 6" x 9" black and white photographic prints are available for any photographs or illustrations appearing in this copy for an additional charge. Contact UMI directly to order.

UMI

A Bell & Howell Information Company
300 North Zeeb Road, Ann Arbor MI 48106-1346 USA
313/761-4700 800/521-0600

Modelling Sea Ice as a Granular Material, with Applications to Climate Variability

Louis-Bruno Tremblay

Department of Atmospheric and Oceanic Sciences
McGill University
Montreal, Canada

December 1996

A thesis submitted to the faculty of
Graduate Studies and Research
in partial fulfilment of the requirements of the degree of
Doctor of Philosophy

0-612-30406-X

Abstract

A new dynamic sea-ice model based on granular material rheology is presented. The sea-ice model is coupled to both a mixed-layer ocean model and a 1-layer thermodynamic atmospheric model which allows for an ice-albedo feedback. Land is represented by a 6-meter thick layer with a constant base temperature. A 10-year integration including both thermodynamic and dynamic effects and incorporating prescribed climatological wind stress and ocean current data was performed in order for the model to reach a stable periodic seasonal cycle. The commonly observed lead complexes, along which sliding and opening of adjacent ice floes occur in the Arctic sea-ice cover, are well reproduced in this simulation. In particular, shear lines extending from the western Canadian Archipelago toward the central Arctic, often observed in winter satellite images, are present. The ice edge is well positioned both in winter and summer using this thermodynamically coupled ocean-ice-atmosphere model. The results also yield a sea-ice circulation and thickness distribution over the Arctic which are in good agreement with observations. The model also produces an increase in ice formation associated with the dilatation of the ice medium along sliding lines. In this model, incident energy absorbed by the ocean melts ice laterally and warms the mixed layer, causing a smaller ice retreat in the summer. This cures a problem common to many existing thermodynamic-dynamic sea-ice models.

The origin and space-time evolution of Beaufort Sea ice anomalies are studied using data and the sea-ice model described above. In particular, the influence of river runoff, atmospheric temperature and wind anomalies in creating anomalous sea ice condition in the Beaufort Sea is studied. The sea-ice model is then used to track the position of an ice anomaly as it is transported by the Beaufort Gyre and the Transpolar Drift Stream out of the Arctic Basin. The results indicate that wind anomalies are the dominant factor responsible for interannual variability in the Beaufort Sea ice cover, whereas temperature and river runoff play a larger role for longer time scale fluctuations. The results also show that sea-ice anomalies originating in the western Beaufort Sea can survive a few seasonal cycles and still account for a significant amount of ice export into the Greenland Sea via Fram Strait. This is a non-negligible contribution to the fresh water budget in this area when compared to fluctuations due to variable wind speed and direction.

It can be inferred from driftwood data collected in the Canadian Arctic Archipelago that very different sea-ice drift patterns were present in the Arctic Ocean during the Holocene. In this study, the sea-ice model described above is used to examine the different modes of Arctic sea-ice circulation during this period, and also to infer characteristics of century-to-millenial scale changes in Arctic atmospheric circulation. The model is forced with prescribed ocean currents, air temperatures and with 1968 (strong negative NAO index) and 1984 (strong positive NAO index) winds, two years with drastically different winter sea level pressure patterns, to assess how sensitive the ice-drift pattern is to the atmospheric forcing. The simulation results show that both a weak Beaufort Gyre with a broad eastward shifted Transpolar Drift Stream (NAO index < 0), and a wide Beaufort Gyre with a narrow westward shifted Transpolar Drift Stream (NAO index > 0) can be reproduced, which Dyke et al. inferred from a radiometric analysis of the driftwood data. Based on the simulation results, the driftwood record also suggests that for long periods (centuries to millenia) of the Holocene, the atmospheric circulation resembled that of a negative or positive NAO index and abruptly changed from one state to the other.

Résumé

Nous présentons un nouveau modèle dynamique de glace marine basé sur la théorie des matériaux granulaires. Celui-ci est couplé à un modèle de couche limite de l'océan et un modèle thermodynamique à une couche de l'atmosphère. Les continents sont représentés par une couche de 6 mètres d'épaisseur ayant une température constante à la base. Nous intégrons le modèle océan-glace-atmosphère, forcé par des vents climatologiques et des courants océaniques stationnaires, pour une période de 10 ans afin d'atteindre un état d'équilibre. Les lignes de fracture, souvent présentes en Arctique, et le long desquelles les blocs de glace glissent ou roulent les uns sur les autres, sont bien simulées par le modèle. Plus particulièrement, les zones de cisaillement allant de l'ouest de l'archipel canadien vers l'Arctique centrale, souvent présentes sur les images satellites durant l'hiver, sont reproduites par le modèle. Ce modèle couplé océan-glace-atmosphère simule bien la position de la limite des glaces tant en hiver qu'en été . Le mouvement des glaces ainsi que la distribution spatiale de l'épaisseur des glaces sont aussi en accord avec les observations. De plus, nous obtenons une formation accrue de glace le long des lignes de fracture due au phénomène de dilatation. Dans ce modèle, l'énergie absorbée par l'océan contribue à la fonte latérale des glaces marines et au réchauffement de la couche limite ce qui entraîne une retraite des glaces beaucoup moins importante en été. Ceci constitue une amélioration considérable par rapport aux modèles dynamique-thermodynamique de glace existants.

Nous étudions l'origine et l'évolution temporelle des anomalies de glace marine dans la mer de Beaufort à l'aide de données et du modèle de glace marine précité. En particulier, nous quantifions l'importance relative, sur la formation d'anomalies de glace dans la mer de Beaufort, des quatre facteurs suivants: les variations de la décharge des rivières, de la température atmosphérique et des vents. Nous utilisons ensuite le modèle de glace pour suivre la trajectoire des anomalies de glace qui se déplacent dans le tourbillon de Beaufort et le courant de dérive transpolaire. Les résultats nous indiquent que les anomalies dans les vents constituent le facteur dominant responsable de la variabilité inter-annuelle de la couverture de glace de la mer de Beaufort; la température de l'air et l'apport d'eau douce des rivières jouent un rôle plus important dans les fluctuations de la couverture de glace

sur des périodes plus longues. Les résultats nous montrent aussi que les anomalies de glace peuvent survivre quelques cycles saisonniers et contribuer de façon importante à la quantité de glace exportée dans la mer du Groenland par le détroit de Fram. Ceci constitue un apport non-négligeable d'eau douce comparé aux fluctuations dues aux anomalies dans la force des vents et leur direction.

Nous pouvons déduire de l'analyse des débris de bois dans l'archipel arctique que des modes de circulation de glace marine très différents ont existé dans l'océan Arctique durant l' holocène. Dans cette étude, nous utilisons le modèle de glace précité, pour étudier les différents modes de circulation des glaces durant cette période ainsi que les variations sur des échelles de temps allant du siècle au millénaire de la circulation atmosphérique en Arctique. Le modèle est forcé par des courants océaniques stationnaires, des températures atmosphériques climatologiques (mensuelles) et des vents de 1968 et 1984 pour déterminer la sensibilité de la circulation des glaces aux forçages des vents; ces deux années ont des moyennes climatologiques hivernales complètement différentes: une (1968) avec un indice NAO fortement négatif et l'autre, avec un indice NAO fortement positif. Dans le cas d'un indice NAO négatif, nous obtenons un tourbillon de Beaufort de dimensions réduites avec un large courant de dérive transpolaire; dans l'autre cas, nous obtenons un large tourbillon de Beaufort avec un courant de dérive transpolaire faible. Ceci est en accord avec les analyses radiométriques des débris de bois de Dyke et al.. En tenant compte des résultats des simulations, une nouvelle interprétation des analyses des débris de bois est possible, i.e. durant de longues périodes de l'Holocène (allant du siècle au millénaire), la circulation atmosphérique était semblable à celle d'un indice NAO positif ou négatif, avec des changements brusques d'un état à l'autre.

À François, qui m'a donné le goût des sciences ...

Contents

List of Figures

List of Tables

Remerciements

Je tiens à remercier mon directeur de thèse, le Professeur Lawrence A. Mysak, d'avoir accepté de diriger ce travail de recherche. Il m'a laissé une très grande liberté dans le choix de mon sujet de recherche et a toujours su me faire profiter de ses nombreux contacts dans le domaine. Je le remercie en outre pour ses commentaires constructifs concernant les chapitres 5 et 6, la revision détaillée du manuscrit, les équipements informatiques qu'il a mis à ma disposition et son soutien financier lors de ma dernière année de recherche. Je remercie également le Docteur Gavin A. Schmidt pour ses conseils judicieux et de nombreuses discussions qui m'ont été tres utiles tout au long de mon doctorat.

Ma reconnaissance va également aux Docteurs Kolumban Hutter et Nico Gray pour la revision et les suggestions quant à l'amélioration des chapitres 2, 3 et 4, au Docteur Jean Côté pour son aide lors de l'implantation numérique du modèle, au Docteur Art Dyke, pour avoir proposé une application paléoclimatique intéressante de mon modèle de glace marine ainsi que pour la revision du chapitre 6, au Docteur Grant Ingram pour la revision du chapitre 5, et au Docteur David Straub pour des discussions utiles concernant la dynamique des océans (appendices B et C). Je remercie également mademoiselle Silvia Venegas, pour ses commentaires pertinents concernant la présentation des résultats du chapitre 5, et messieurs Halldór Björnsson, Martin Charron et Paul Vaillancourt pour de nombreuses discussions intéressantes autour d'une bonne bière.

Je tiens à souligner l'aide financière que m'a apportée le Conseil de Recherche en Sciences Naturelles et en Génie du Canada (CRSNG) ainsi que le Fonds pour la Formation de Chercheurs et l'Aide à la Recherche par l'entremise de bourses d'étude. Les subventions de recherche provenant du Service d'Environnement Atmosphérique et du CRSNG, accordées à Lawrence Mysak, sont aussi grandement appréciées.

En dernier lieu, je remercie Isabel Faille pour sa patience et sa tolérance envers un conjoint trop souvent préoccupé par une thèse toujours plus longue à terminer.

Statement of originality

A new sea-ice rheology which treats the ice as being a granular material is presented (chapters 2, 3 and 4). The approach is motivated by observations of the sea ice cover on scales of tens to hundreds of kilometres, which shows deformation (lead) patterns typical of granular material. Unlike most sea-ice models now used in the community, this model has both a sound physical basis and is still simple enough to be used in climate studies of the high latitudes. Other rheologies such as the cavitating fluid rheology with and without added shear strength (Flato and Hibler, 1992), can be derived as special cases of the present approach. The model is coupled thermodynamically to an atmosphere, which contrasts with most detailed Arctic modelling studies in which the air temperature is prescribed and therefore sets the ice edge position and part of the thickness distribution. Finally, the source code for this model is completely original. This work has been accepted for publication in the Journal of Physical Oceanography (September 1996). The very positive reviews stated that the paper represents "... real progress in the modelling of sea-ice-atmosphere interactions ..." (reviewer A) and " ... great contribution to physical oceanography ..." (reviewer B).

Measured atmosphere-ice drag coefficients vary widely (one order of magnitude), depending on the ice cover roughness and the atmospheric stability. However, most sea-ice modelling studies use drag coefficients at the bottom of this range, representative of smooth ice cover and stable atmospheric stratification. The influence of using variable drag coefficients that are dependent on the ridge-related surface roughness are presented in appendix D. This work has been accepted for publication in the Annals of Glaciology (September 1996).

In chapter 5, the sea-ice model is used to simulate the anomalous sea-ice conditions in the Beaufort Sea in 1965. Results are compared with observations for the same period. This work will be submitted to the Journal of Climate.

In chapter 6, the sea-ice model is used to study the widely different sea-ice drift patterns present during the Holocene, as inferred from an analysis of driftwood collected on the raised beaches of the Canadian Arctic Archipelago. This work will be submitted for publication in Geophysical Research Letters.

Chapter 1

Introduction

The presence of sea ice in the polar regions has a substantial influence on regional as well as global climate. Firstly, sea ice is highly reflective and therefore reduces the amount of solar radiation absorbed by the surface at high latitudes. Secondly, it acts as an insulator, reducing the amount of heat, moisture and momentum flux between the ocean and the atmosphere. Thirdly, the release (absorption) of heat during ice formation (melt) is an important factor in the atmospheric energy budget. Finally, the transport of ice from one region to another constitutes a flux of freshwater which strongly influences the circulation in the Arctic Ocean and surrounding seas (eg., deep water formation in the northern North Atlantic).

Because of the enormous difficulties in making extensive measurements in ice-covered waters, our knowledge of the physical aspects of the Arctic and Antarctic relies heavily on the numerical modelling of these regions. To model the ice behaviour accurately, it is now recognized that both thermodynamic and dynamic processes must be included and allowed to interact with other components of the climate system. For example, the ridging of ice in a convergence zone and lead opening in a region of divergence strongly influences the distribution of heat lost from the ocean to the atmosphere, which in turn strongly affects the atmospheric circulation. The latter would affect the winds which then feed back on the ice motion. Further, in the Arctic, where the sea-ice motion is restricted by the presence of continental boundaries, strong interactions between ice floes take place and influence the basin-wide ice circulation. Consequently, a good understanding of the forces (or stresses) generated during ice interactions and the deformation (or strain) that follows are of primary importance.

As a first step in the modelling of sea ice, assumptions about the nature of the material must be made in order to specify the relationship between the internal ice stresses and the deformation field[1], which is necessary in order to have a closed system of equations. Past approaches have included modelling the ice as a Newtonian fluid (Laikhtman, 1958; Ruzin, 1959; Campbell, 1965; Glen, 1970), a cavitating fluid (Doronin, 1970; Flato and Hibler, 1992), an inviscid incompressible fluid (Rothrock, 1973), an elastic-plastic material (Coon *et al.*, 1974) and a viscous-plastic material (Hibler, 1979). In the above, the cavitating fluid and different plastic models involve non-linear rheologies, whereas the Newtonian and inviscid incompressible fluid models have linear rheologies. In the first half of the century, sea ice models ignored the interactions between ice floes, or only considered a simple frictional law in lieu of an internal ice stress term. In the following, a historical review of the constitutive relations used in large-scale sea-ice modelling is presented.

In his sea-ice drift study, based on data collected from the Fram, Nansen (1902) considered the effects of the earth's rotation (Coriolis effect), the wind stress and the water drag. Following the standard Ekman spiral theory, the ice-water drag was assumed to act at a constant angle of 45° (ocean turning angle) from the ice drift direction. This resulted in a systematically larger calculated angle between the sea-ice drift and the wind direction than what was observed. The neglect of the internal ice stress term in this study was not critical since the Fram was anchored on an ice floe in the Transpolar Drift Stream, a region where relatively little ice interaction takes place.

A few decades later, in a sea-ice drift study on the North Siberian shelf, the ice interaction term was considered for the first time (Sverdrup, 1928). It was parameterized as a simple frictional law with a linear dependence on the sea-ice velocity. The ice-water drag term, however, was ignored, an approximation based on observations of the ocean mixed-layer density profile. Good results were obtained in the study area (Siberian shelf), but the model failed to predict the ice motion correctly in other regions. Curiously, this approach is equivalent to a free-drift solution with a linear ice-water drag law and a zero ocean turning

---

[1] These relations are called the constitutive equations and the branch of physics concerned with these relations is called rheology, from the Greek words rhei (flow) and logos (science).

angle.

In the above and other studies, the ice stresses were assumed to be a function of the sea-ice velocity rather than the deformation field (or strains). Strictly speaking, this does not constitute a parameterization of the ice floe interactions. The first attempts at really considering the ice interaction term were made in the late fifties. These models assumed the ice to be a highly viscous film of Newtonian fluid at the ocean-atmosphere interface (Laikhtman, 1958; Ruzin, 1959; Campbell, 1965). The ice interaction term was written as the Laplacian of the sea-ice velocity multiplied by a coefficient of shear viscosity with a linear dependence on the local measured ice thickness. To allow for a more mobile pack ice in the summer, Campbell (1965) suggested the use of a coefficient of viscosity dependent on sea-ice temperature[2]. This yielded a sea-ice drift pattern close to that observed, when the coefficient of eddy viscosity was as high as 10^8 m^2/sec. However, unrealistically large sea-ice convergence was present in the Beaufort Sea since the pressure gradient term (∇P), which would normally tend to oppose convergent motion, was not taken into account.

Campbell and Rasmussen (1972) later proposed adding a bulk viscosity coefficient (a stress term proportional to the sea-ice divergence) to reduce the sea-ice convergence observed in the previous work. This idea was more formally derived in a rheological model presented by Glen (1970). The proposed constitutive relations turned out to be equivalent to the general deformation law for a Newtonian compressible flow. The pressure gradient term, however, was still ignored in this new approach and a certain amount of convergence was always present.

Although the addition of a bulk viscosity is an improvement, modelling sea ice as a conventional fluid implies that there are floe interactions in both convergent and divergent flow, which is contrary to observations, which show that sea ice offers very little resistance to diverging motion. This is due to the fact that sea ice is a densely fractured material and its tensile strength is practically zero. To better simulate this effect, Nikiforov et al. (1970) proposed to model the pack ice as a cavitating fluid[3], or a fluid with two phases, consisting

---

[2] More recent modelling studies take this into account by considering the percentage of a grid cell covered by water. In the summer, melting occurs and the ice concentration decreases, resulting in an easily deformable pack ice.

[3] Cavitation refers to the fact that cavities form in the fluid. The term was first used in fluid applications

of ice and water. When the ice concentration is 100 % (no leads present), sea ice can resist any compressive load, i.e., it is considered incompressible or non-divergent. On the other hand, when tensile loads are acting on the material, the sea ice opens up and cavitates without offering any resistance; in this mode, the sea-ice concentration decreases and the motion is described by the free-drift equations. In addition, the resistance of the material to shear motion (shear viscosity) is assumed to vary linearly with ice concentration (Doronin, 1970). When the ice concentration increases, so does the probability of ice floe interaction. This results in an increase in the shear viscosity. To close the system of equations, an evolution equation for ice concentration is used. This model allowed not only for a better representation of the internal ice stress term, but also for the calculation of open water areas (leads) in the ice field (an important feature influencing the ocean-atmosphere heat flux) and for a definition of the ice edge position in terms of a pre-defined ice concentration cutoff. The resistance to compressive load, however, is infinite and is not achieved through a pressure gradient term term but in a rather artificial manner.

The pressure gradient term (internal ice pressure term) is certainly an important ingredient in a realistic sea-ice model, and it was first introduced explicitly by Rothrock (1973). He assumed the ice to be compact everywhere and consequently modelled the pack ice motion as an incompressible fluid. He further assumed the ice to be inviscid. Such a fluid can only resist normal stresses (through the pressure term) and offers no resistance to shearing motion. The simulated ice drift patterns were realistic using this model, but the ice velocity tended to be too high, presumably due to the absence of shear viscosity. In this problem, the solution of the ice internal pressure is defined to within a constant. The constant was chosen such that the minimum ice pressure was a negligibly small positive number.

In the above, the concept of sea ice having a shear viscosity with simple dependence on thickness or concentration was introduced. Also, the inclusion of a pressure term or a bulk viscosity to resist converging motion was discussed. With a pressure term included, the sea ice is incompressible and no mechanical buildup of ice is allowed in ridging zones, for example. With a bulk viscosity included, however, any convergent wind forcing would produce

---

where cavitation occurs when the fluid pressure drops below its vapour pressure; at this time vapour bubbles begin to appear in the fluid, which is observed, for example, in the wake of a marine propeller.

a convergence in the sea-ice drift motion. Observations show that reality lies somewhere between those two extremes: compressive loads below a certain critical value are sustained with hardly any convergence, whereas compressive loads above the critical value will lead to convergence and the formation of ridges. Measurements also show that the energy expanded in building a ridge is rate independent and is an irreversible process (Parmerter and Coon, 1973). All of this is indicative of a plastic behaviour[4]. Moreover, there exist strong similarities between the pack ice when seen from high altitudes and other material such as gravel, sand, clays which have all been modelled successfully using plasticity theories. In the seventies, a large body of work on sea ice was done as part of the Arctic Ice Dynamics Joint Experiment (AIDJEX) program and the plastic approach to sea ice modelling was adopted. This approach constituted a major improvement over previous ones and is still used by most ice modellers today.

To model sea ice as a plastic material, two requirements are necessary. Firstly, a yield criterion is required to establish the difference between small loads resulting in tiny recoverable (elastic) deformations and large loads resulting in large permanent (plastic) deformations. The yield criterion is determined from the capacity of the material to resist compressive, tensile and shear loads. Secondly, two flow rules are necessary to describe the resulting elastic and plastic deformations. The relationship between stresses and deformation in the elastic regime is well known from the field of mechanics of material (Popov, 1952); however in the plastic regime, different types of materials require different flow rules and much work is still underway to try to establish the best approach.

In 1974, Coon et al. (1974) developed the elastic-plastic sea ice model which incorporated all the above ingredients. The resistance of the material in shear is proportional to the normal stress at the shearing plane[5], the ice resistance to tensile forces is zero and the free drift equations still applies to divergent ice flow. Also, the pressure term is included and allows for convergent motion if the normal load exceeds the yield criteria, and small deformations

---

[4] A plastic deformation is a permanent deformation, i.e. the material will not recover its original shape upon removal of the load; i.e. the process is irreversible.

[5] This is called the Mohr-Coulomb yield criteria; this is equivalent to static friction between two dry surfaces.

are considered elastic and recoverable. Their yield criterion was considered to be a function of sea ice thickness and concentration, i.e. thin and loose ice is considered to be more easily deformable than thick and compact ice. Evolution equations for ice thickness (continuity equation) and concentration are used to close the problem. This is the first model to provide a coupling between the ice resistance in compression (yield criteria) and the continuity equations through the ice thickness and concentration. The elastic-plastic approach yielded a more successful simulation of the ice velocity field and thickness distribution. However, the choice of flow rule and yield curve results in excessive divergence (or dilatation) during shearing deformation (Spencer, 1964); this leads to an overestimate in the heat loss from the ocean to the atmosphere as more open water areas form. Also, the history of the state of strain of the ice must be stored since elastic strain is reversible, making the numerical treatment of the resulting set of dynamical equations very complicated (it usually requires a Lagrangian approach).

Hibler (1979) proposed a viscous-plastic model as a simplification of the elastic-plastic approach. The yield curve used in this study is a crude approximation of the one used by Coon et al. but is much simpler mathematically: it allows the stresses to be written in terms of the strain rates explicitly. The resulting constitutive relations have the same form as for a viscous compressible fluid but with a non-linear dependence of the shear and bulk viscosities on the strain rates. In this model, small elastic deformations are approximated by creeping flow (viscous behaviour) (Hibler, 1977), which allows the use of the standard Eulerian approach. This constitutes the main improvement of this new model. In practical term, this is simply achieved by specifying the coefficient of viscosity to a large but finite constant value when tiny deformations occur. The choice of yield curve and flow rule used by Hibler, however, can lead to unphysical effects. In particular, the presence of strong divergent flow may be possible even though the average normal stress, or internal ice pressure, is negative (in compression). Also, ice is allowed to have some tensile strength. Both of these violate the author's original assumptions that the internal ice pressure is zero for divergent flow and that sea ice has no tensile strength.

Recently, a reformulation of the cavitating fluid rheology of Doronin was presented (Flato and Hibler, 1992) in which the internal ice pressure is calculated explicitly. The sea ice is assumed to have no shear strength, no tensile strength and a maximum compressive strength that is a function of ice concentration and thickness. This allows for sea ice convergent motions (ridging) when the normal load exceeds the critical value. This constitutes an improvement over Doronin's approach which simply forced the solution to be non-divergent without explicitly calculating the pressure gradient term. In the cavitating fluid approach, the mathematical formulation and implementation is simple. However, the ice velocity tends to be too high due to the absence of frictional forces between the floes. But this shortcoming can turn into an advantage for certain climatic applications in which the wind is underestimated due to the use of bi-weekly or monthly averaged winds.

In this thesis, we consider the ice to be a slowly deforming granular material (a collection of ice floes), and we use a simplified version of the double sliding model developed by Balendran and Nemat-Nasser (1993). This is motivated by observations of the Arctic sea-ice cover which show a distinct lead pattern at various scales that is typical for that type of material (Erlingsson, 1988). This model incorporates some features of the previous ice models (the failure curve of Coon et al. (1974) and the creeping flow approximation of small elastic deformation of Hibler (1977)), but invokes a more general treatment of the deformation rule. In particular, the opening of leads (dilatation) associated with shearing deformation (Stern *et al.*, 1995), a feature which is not simulated in Hibler's model and which is overestimated in Coon et al.'s model, follows naturally from the present formulation and eliminates the need for its parameterization as proposed by Stern et al. The extension of the cavitating fluid model to include shear strength (Flato and Hibler, 1992) can also be derived as a special case of the present formulation.

Another important aspect of the present model relates to the treatment of the atmosphere and ocean. In most previous studies (Hibler and Walsh, 1982; Holland *et al.*, 1993), sea-ice models and coupled sea-ice–ocean models were run with prescribed atmospheric temperature and humidity distributions. This boundary condition on temperature largely determines, a priori, the ice thickness distribution and ice edge position (the air temperature has a strong ice-cover signature, i.e. the air is warm over water and much cooler over ice-covered seas). In the present study, the sea-ice model is coupled thermodynamically to a mixed-layer ocean and an atmosphere model which allows for an ice-albedo feedback. This is a more stringent test on the validity of the full sea-ice model. Also, the energy exchange between the ocean mixed-layer and the ice is done through sensible heat transfer. Consequently, the mixed-layer is allowed to warm even when ice is present in the vicinity (Maykut and Perovitch, 1987). This will have an influence on the ice retreat in the warm season.

The next chapter presents supporting evidence for using the present sea-ice rheological model, along with the complete description of the model equations for the sea ice, ocean and land. In chapter 3, the numerical scheme is described. In chapter 4, the model results at the end of a 10-year integration are compared with satellite observations and submarine sonar data. In the last two chapters, climatic applications of the model are presented. Chapter 5 presents results on the formation and evolution of ice anomalies in the Beaufort Sea on the interannual time scale. Chapter 6 attemps to hindcast the different ice drift patterns on century-to-millenial time-scales in the Holocene that have been inferred by driftwood samples collected in the Canadian Arctic Archipelago. The main conclusions drawn from the simulation results are presented in chapter 7.

Chapter 2

Governing equations

2.1 Sea-ice momentum, continuity and energy equations

The governing equations for sea ice, derived from conservation principles, are presented in this section along with appropriate boundary conditions. The momentum balance for the two-dimensional horizontal motion of sea ice can be written as

$$\rho_i h \frac{d\boldsymbol{u}_i}{dt} = -\rho_i h f \boldsymbol{k} \times \boldsymbol{u}_i + A(\boldsymbol{\tau}_a - \boldsymbol{\tau}_w) + \nabla \cdot \boldsymbol{\sigma} - \rho_i h g \boldsymbol{\nabla} H_d, \qquad (2.1)$$

where ρ_i is the sea-ice density, h the mean ice thickness, f the Coriolis parameter, $\boldsymbol{k}$ a unit vector normal to the ice surface, $\boldsymbol{u}_i$ the ice velocity, A the ice concentration (percentage of a grid cell covered by ice), $\boldsymbol{\tau}_a$ the wind shear stress on the top ice surface, $\boldsymbol{\tau}_w$ the ocean drag on the sea-ice flow, σ_{ij} ($\boldsymbol{\sigma}$)the vertically integrated internal ice stress (normal or shear) acting on a plane which is perpendicular to the i-axis and in the j-direction, g the gravitational acceleration and H_d the sea-surface dynamic height. Following Gray and Morland (1994), the wind stress and water drag are multiplied by the ice concentration to account for the fact that water may be present in a grid cell. This, however, has a minor effect on the results. The air ($\boldsymbol{\tau}_a$) and water ($\boldsymbol{\tau}_w$) stresses are obtained from a simple quadratic law with constant turning angle (McPhee, 1975),

$$\begin{aligned}
\boldsymbol{\tau}_a &= \underbrace{\rho_a C_{da}|\boldsymbol{u}_a^g|}_{C'_{da}}\ (\boldsymbol{u}_a^g \cos\theta_a + \boldsymbol{k} \times \boldsymbol{u}_a^g \sin\theta_a), && (2.2)\\
\boldsymbol{\tau}_w &= \underbrace{\rho_w C_{dw}|\boldsymbol{u}_i - \boldsymbol{u}_w^g|}_{C'_{dw}}\ \left[(\boldsymbol{u}_i - \boldsymbol{u}_w^g)\cos\theta_w + \boldsymbol{k} \times (\boldsymbol{u}_i - \boldsymbol{u}_w^g)\sin\theta_w\right], && (2.3)
\end{aligned}$$

where ρ_a and ρ_w are the air and water densities, C_{da} and C_{dw} the air and water drag coefficient, $\boldsymbol{u}_a^g$ and $\boldsymbol{u}_w^g$ the geostrophic wind and ocean current and θ_a and θ_w the wind and water turning angles. In the above equation for the wind shear stress, the ice speed is considered small compared to the wind speed and is therefore neglected.

The ice strength in this model is a function of both the mean ice thickness h and ice concentration A (percentage of a grid cell covered by ice). For this reason, a conservation law for both quantities, derived by averaging the two-dimensional continuity equation, is necessary:

$$\begin{aligned}
\frac{\partial h}{\partial t} + \nabla \cdot (h\boldsymbol{u}_i) &= S_h + K_h \nabla^2 h, && (2.4)\\
\frac{\partial A}{\partial t} + \nabla \cdot (A\boldsymbol{u}_i) &= S_A + K_A \nabla^2 A, && (2.5)
\end{aligned}$$

where K_h and K_A are the diffusion coefficients for ice thickness and concentration and, S_h and S_A are the thermodynamic source terms given by:

$$S_h = \frac{1}{\rho_i L_f}\begin{cases} A\,(Q_{ia} - Q_{oi}) + (1-A)\,Q_{oa}, & T_o = T_{of},\ Q_{oa} > 0 \\ A\,(Q_{ia} - Q_{oi}), & T_o > T_{of} \end{cases} \qquad (2.6)$$

$$S_A = \frac{1}{\rho_i L_f}\begin{cases} (1-A)\,Q_{oa}/h_0, & T_o = T_{of},\ Q_{oa} > 0 \\ A\,\rho_i L_f S_h/2h, & S_h < 0 \end{cases} \qquad (2.7)$$

where L_f is the latent heat of fusion, Q_{ia} and Q_{oa} the net ice and oceanic heat fluxes to the atmosphere due to longwave ($Q_{lw-up}, Q_{lw-down}$), sensible (Q_{sens}), latent heating (Q_{lat}) and shortwave radiation (Q_{sw}) (see figure 2.1), Q_{oi} the sensible heat flux from the water to the ice, h_0 a fixed demarcation thickness between thin and thick ice (Hibler, 1979) and, T_o and T_{of} the temperature and freezing point temperature of the ocean. In equation 2.5, the ice concentration is restricted to lie between zero and one using a mechanical sink term.

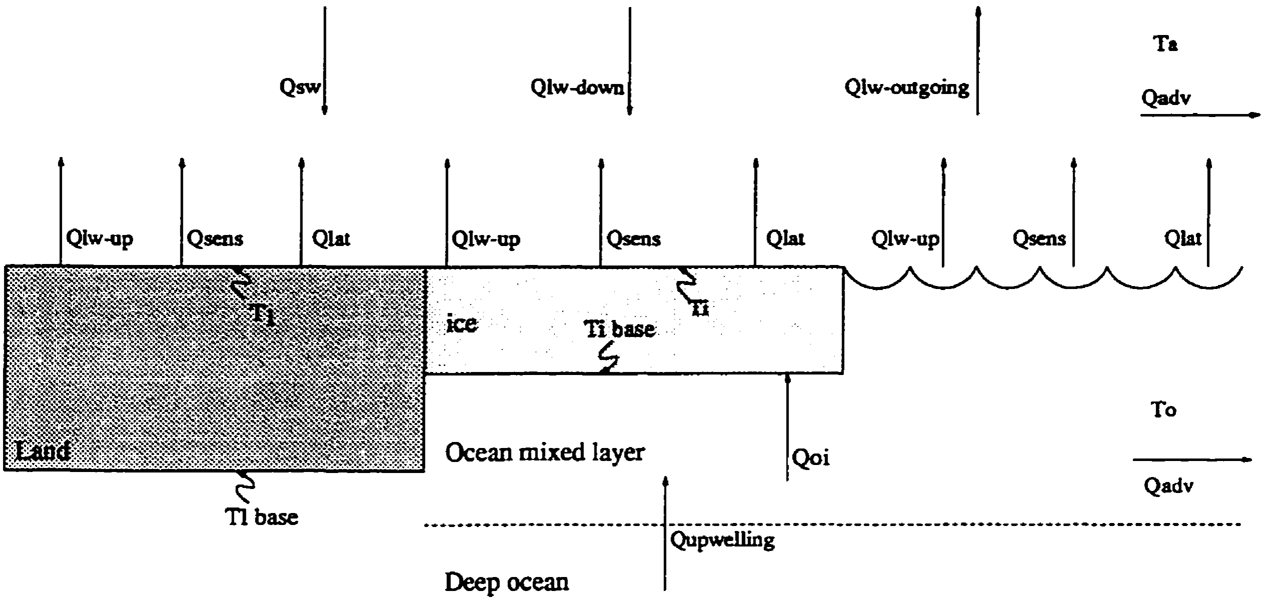

Figure 2.1: Heat fluxes over a grid cell. Ocean-atmosphere, ice-atmosphere, land-atmosphere and ocean-ice heat fluxes are defined positive upward. Note that the short wave energy absorbed by the surface depends on the surface albedo. The terms Q_{adv} for the atmosphere and ocean are given in equations 2.11 and 2.12

In most existing ice thermodynamic models, incident energy absorbed by the ocean mixes horizontally and melts ice until no ice is present in a grid box. In this manner, the ocean temperature can only rise above freezing point after all ice is melted. In the present model the ocean is allowed to warm up even though ice is present in a grid cell. The transfer of heat between the ocean and the ice is achieved through sensible heating in a similar manner as between the ice and the atmosphere. Under winter growth conditions, the formation of ice due to Q_{oa} will only occur once the ocean temperature reaches freezing point. During the melting period, incident energy absorbed by the ocean will partly warm up the mixed layer and partly be used to melt ice. Measurements by Maykut and Perovich (1987) suggest that 80 % of the incident energy on the ocean will warm up the mixed layer. This will give a more realistic ice retreat during the melting season.

For the case of ice-atmosphere heat transfer, the various heat fluxes are defined as

$$\begin{gathered} Q_{sw} = Q_0(1-\alpha_a)\,(1-a_a)\,(1-\alpha_i) \\ Q_{sens} = \rho_a C_{sens}|\boldsymbol{u}_a| C_{pa}(T_i - T_a), \quad Q_{lat} = \rho_a C_{lat}|\boldsymbol{u}_a| L_s(q_i - q_a) \\ Q_{lw-down} = \epsilon_a \sigma T_a^4, \quad Q_{lw-up} = \epsilon_i \sigma T_i^4 \end{gathered} \tag{2.8}$$

where Q_0 is the daily averaged flux of solar radiation (Zillman, 1972), α_a and α_i the atmospheric and ice albedo, a_a the atmospheric absorptivity to shortwave radiation, C_{sens} and C_{lat} the sensible and latent heat transfer coefficients, ϵ_a and ϵ_i the atmospheric and ice emissivities, σ the Stefan-Boltzmann constant, C_{pa} the specific heat of air, L_s the latent heat of sublimation, T_a and T_i the air and ice temperature and, q_i and q_a the atmospheric and ice surface (assumed saturated) specific humidities which are given by

$$q_i = q_s = \frac{0.622\ e_{sat}}{P_s - 0.378\ e_{sat}}, \qquad q_a = 0.8\ q_s, \tag{2.9}$$

where

$$e_{sat} = 611 \times 10^{A_1 \frac{T_s - 273.13}{T_s - A_2}},$$

and P_s is the sea-level pressure (considered constant). In equation 2.9, the relative humidity of the atmosphere is considered constant (80%), and the dependence of A_1 and A_2 on ice concentration is ignored. In the present study, similar expressions (equations 2.8 and 2.9) are used for the ocean-atmosphere and ocean-ice heat transfers.

Up to this point, the momentum and continuity equations have been presented. A thermodynamic equation for the ice is also needed to determine the ice surface temperature. The three-dimensional energy equation for the ice takes the form

$$\rho_i C_{pi} \left(\frac{\partial T_i}{\partial t} + \nabla \cdot (\boldsymbol{u}_i T_i) \right) = K_i \nabla^2 T_i, \tag{2.10}$$

where C_{pi} is the ice specific heat capacity and K_i the ice thermal conductivity.

2.2 Atmosphere, ocean and land models

The sea-ice model is coupled above, to a 1-layer thermodynamic model of the atmosphere, and below, to an ocean mixed-layer. Also, the continents are represented by a 6-meter thick layer of conducting material with constant base temperature. The relevant conservation of energy equations are used to compute the temperature of the atmosphere (T_a), ocean (T_o) and land (T_l); these take the form

$$\begin{aligned}
\rho_a C_{pa} H_a \left(\frac{\partial T_a}{\partial t} + \nabla \cdot (\boldsymbol{u}_a^g T_a)\right) &= \lambda\left[(1-A)Q_{oa} + AQ_{ia}\right] + (1-\lambda)Q_{la} \qquad (2.11)\\
&\quad - Q_{lw-out} + K_a \nabla^2 T_a,\\
\rho_w C_{pw} H_o \left(\frac{\partial T_o}{\partial t} + \nabla \cdot (\boldsymbol{u}_w^g T_o)\right) &= -(1-A)Q_{oa} - AQ_{oi} + Q_{upwelling} \qquad (2.12)\\
&\quad + K_o \nabla^2 T_o,\\
\rho_l C_{pl} \frac{\partial T_l}{\partial t} &= K_l \nabla^2 T_l, \qquad (2.13)
\end{aligned}$$

where ρ_l is the land density, C_{pw} and C_{pl} the specific heat capacities for water and land, H_a and H_o the atmosphere scale height and the ocean mixed layer depth, λ a land mask parameter (equal to 0 over land and to 1 otherwise), Q_{la} the energy flux to the atmosphere from the land due to longwave, sensible, latent heating and shortwave radiation, Q_{lw-out} the longwave radiation lost to space, $Q_{upwelling}$ the energy flux into the mixed layer from the upwelling of warm water from the deep ocean, K_a and K_o the atmosphere and ocean diffusion coefficients, K_l the land thermal conductivity and T_l the land temperature. In the above equations, the advective terms are represented as Q_{adv} in figure 2.1. To calculate $Q_{upwelling}$, it is assumed that when ice forms it rejects all of its salt; for a salinity and temperature difference of 5 ppt and 2 C° between the deeper ocean and surface waters, this results in heat flux into the mixed layer approximately equal to 10 % of the latent heat flux released during ice formation.

2.3 Sea-ice rheology

In order to close the system of equations, the stresses ($\boldsymbol{\sigma}$) must be written in terms of the basic variables describing the ice behaviour. In mathematical form this is written as follows:

$$\sigma_{kl} = f_{kl}(u_{i,j}, h, A, T_i),$$

where $u_{i,j} = \partial u_i / \partial x_j$ is the velocity gradient consisting of a symmetric part $\dot{\epsilon}_{ij} = (u_{i,j} + u_{j,i})/2$, the stretching (strain rate) tensor and an antisymmetric part $\dot{\Omega}_{ij} = \frac{1}{2}(u_{i,j} - u_{j,i})$, the spin (angular velocity) tensor, and T_i is the ice temperature. In the model proposed here, the dependence of the stresses on $\dot{\Omega}_{i,j}$ and ice temperature will be ignored. These equations are called the constitutive relations and are material dependent. Thus, assumptions about the type of material and its behaviour in deformation must first be postulated.

The sea-ice cover consists of many floes and is assumed to be a large scale granular material in slow continuous deformation. A granular material is a collection of a large number of discrete solid grains (eg., ice floes) with accompanying interparticle voids. These voids are usually filled with fluid such as air or water, and strictly speaking, the flow of a granular mass is a multi-phase flow. However, for closely packed material or when the density of the interstitial fluid is small compared to the particle density, the transfer of momentum is done mainly by the particles and the flow can be considered as a dispersed single-phase flow rather than a two-phase flow. The flow of sea-ice is considered to fall in the former category.

Depending on the local stress conditions, sea-ice can behave as an elastic solid, a plastic solid or a fluid. During its elastic-solid behaviour, sea-ice can resist large forces induced by winds and ocean currents in the presence of boundaries, with relatively small deformation (compared to plastic deformation). However, much of this resistence occurs at frictional bonds between the floes, and as such the ice strength is limited by the loads those bonds can take. When the force transmitted across intergranular contact points exceeds certain critical values for compressive, shear and tensile loads (failure criterion), the structure collapses and it starts to flow. When the compressive load limit is reached the floes override one another forming a ridge (Hopkins, 1994); when the tensile load limit is reached (equal to zero, no cohesion) the floes drift freely without interacting with one another; and when the shear load limit is reached, the failure consists of a group of several floes sliding or rolling relative to one another along **sliding lines** roughly aligned with the stress characteristics in the material. Examples of such sliding lines are shown in figure 2.2 for different length scales. Earlier work by Marko and Thompson (1977) explained the presence of those features by brittle material fracture. Later, Pritchard (1988) demonstrated that plastic models used for sea-ice modelling can explain the presence of such lead patterns. For sea ice, the relative ice speed across sliding lines is small, and the different floes remain in contact during deformation, allowing friction to act. This is termed the quasi-static flow regime (see Babic *et al.* (1990) for a detailed classification). In the rapid flow regime, the interactions between the floes are

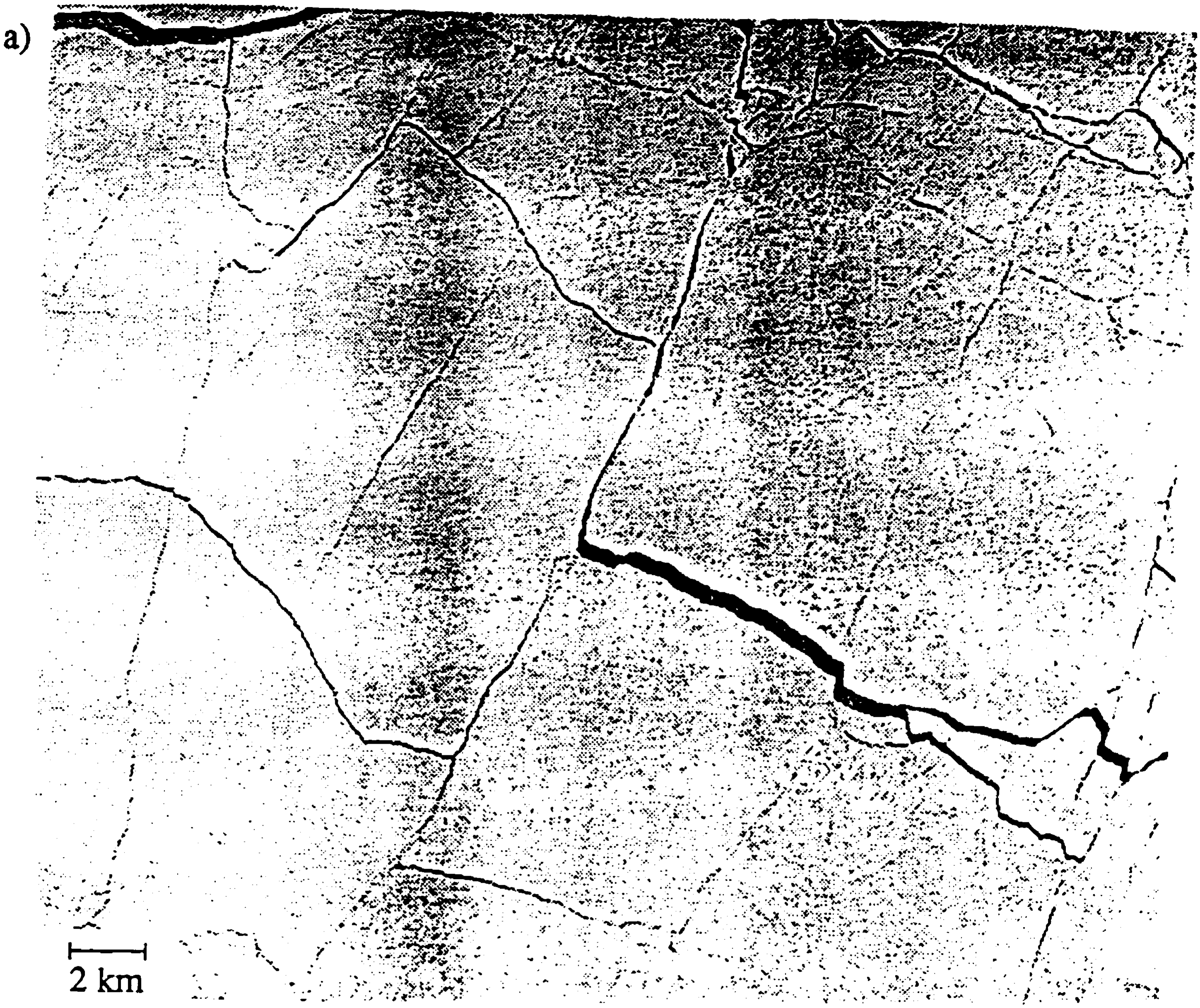

Figure 2.2: (a) Photograph of the Arctic pack ice taken at an altitude of 6.1 km (adapted from Coon *et al.*, 1974); (b) Satellite picture of the pack ice north of Greenland and Ellesmere Island (adapted from Kozo *et al.*, 1992); and (c) SSM/I brightness temperature of the Arctic (NSIDC data).

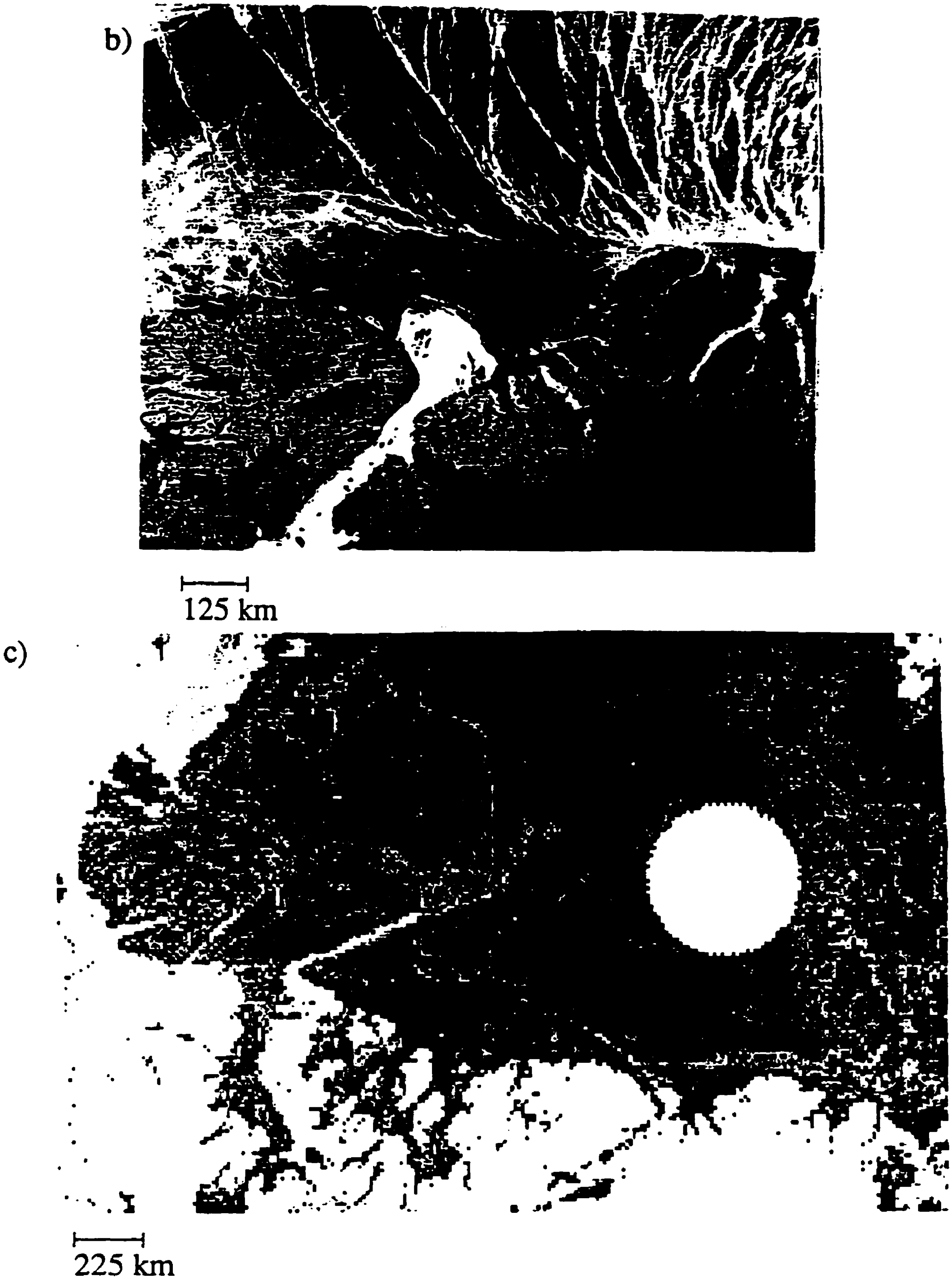

Figure 2.2: continued

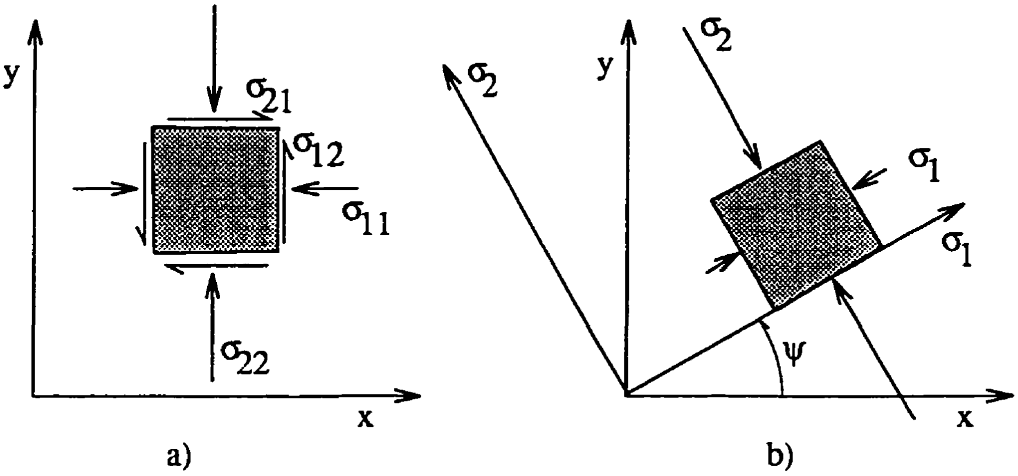

Figure 2.3: State of stress at a point in model coordinates, (a), and principal stress coordinates, (b).

modelled as inelastic collision. This type of approach has been used in the ice margin region where the floe speeds are typically larger (Shen *et al.*, 1986). For a review on high speed granular flow, see Campbell (1990) and Hutter and Rajagopal (1994).

From the above considerations, we derive macroscopic constitutive relations, based on the microscopic behaviour of the floes, that model the large scale motion of sea ice. The model presented here is based on the double sliding model of Balendran and Nemat-Nasser (1993), in which inelastic deformation is assumed to consist of two superimposed shear deformations along sliding lines obtained from the Mohr-Coulomb failure criterion, or ridging when the average normal stress at a point exceeds the ice strength in compression. However, the elastic deformation, the dependence of the stresses on the rotation tensor and the variable internal angle of friction are neglected (the deformation history of the material is ignored). These simplifications make this model suitable for climate studies which involve longer time scales.

Consider the stresses acting on an ice element, as shown in figure 2.3–a (compressive stresses are defined as negative). Since the stress tensor is symmetric, it will always be possible to diagonalize it with a pure rotation of the coordinate axes (see figure 2.3-b). The stresses acting on the rotated element are the maximum and minimum normal stresses acting at a point and are called the principal stresses (σ_1 and σ_2); the shear stresses acting on the rotated element vanish identically. The principal stresses can also be interpreted as the eigenvalues of the stress tensor matrix, and the angle of rotation ψ between the two coordinate systems can be deduced from the rotation matrix composed of the two normalized eigenvectors. These new coordinate axes will provide a useful reference to determine the failure criterion of a given material. Mathematically, they can be written in terms of the two stress invariants, the average normal stress (or pressure) p and the maximum shear stress q, as follows:

$$\sigma_1 = -p + q, \qquad \sigma_2 = -p - q,$$

where

$$p = -\frac{\sigma_{ii}}{2}, \qquad q = \left(\frac{\sigma'_{ij}\sigma_{ij}}{2}\right)^{1/2}, \qquad \sigma'_{ij} = \sigma_{ij} + p\delta_{ij},$$

and the angle ψ between the x-y and the principal stress axes satisfies the following relation:

$$\tan 2\psi = \frac{2\sigma_{12}}{\sigma_{11} - \sigma_{22}}. \tag{2.14}$$

Similar expressions can also be derived for the strain rate tensor $\dot{\epsilon}$. The strain rate invariants, $\dot{\epsilon}_1$ and $\dot{\epsilon}_2$, can be physically interpreted as the divergence and the maximum shear strain rate at a point (see Ukita and Moritz (1995) for a review).

2.3.1 Failure criterion

In the following, we consider the planar deformation of sea ice (two-dimensional horizontal flow of cylindrical ice floes), with occasional overriding of adjacent ice floes. First, a failure criterion is required to specify the transition between elastic-solid and plastic-solid/fluid behaviour. This will lead us into section 2.3.3, where constitutive relations that model the resulting deformation are given.

For sea-ice deformation along a sliding line, the failure criterion, based on Coulomb's friction law, can be written as follows:

$$\tau_s = -\sigma_s \tan\phi, \tag{2.15}$$

where ϕ is the effective angle of friction and τ_s and σ_s are the shear and normal stresses acting on the sliding plane (see figure 2.4). The above expression is exactly equivalent to dynamic friction between two dry surfaces where the frictional force is proportional to

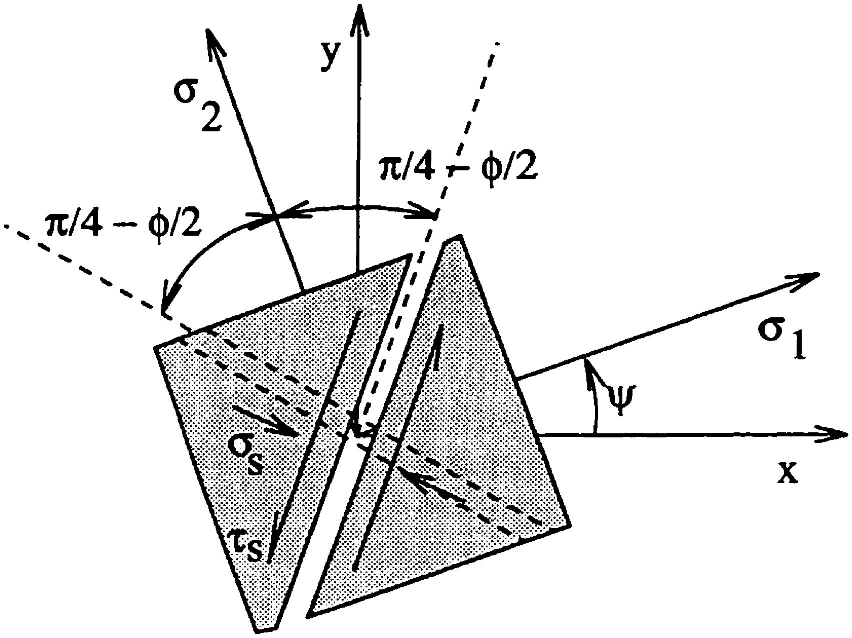

Figure 2.4: The orientation of the sliding lines (dashed) with respect to the x-y and σ_1–σ_2 coordinate systems. The second sliding line is shown as a double dashed line for the sake of clarity.

the normal force; the constant of proportionality is the coefficient of friction ($\tan\phi$). For stress ratios $\tau/(-\sigma)$ less than the effective angle of friction, sea ice behaves as an elastic solid, and when the stress ratio is equal to $\tan\phi$, it flows like a fluid. There are two planes on which this stress ratio reaches its maximum value, and they are situated symmetrically about the greater principal stress axis (σ_2) at angles of $\pm(\pi/4 - \phi/2)$ (figure 2.4). Writing the stresses σ_s and τ_s in terms of the stress invariants, the sliding criterion (equation 2.15) can be rewritten as:

$$q = p\sin\phi, \tag{2.16}$$

with

$$\tau_s = q\cos\phi, \qquad \sigma_s = -(p - q\sin\phi). \tag{2.17}$$

In the above equation, the pressure p is limited to a maximum value P_{max}, which is a function of the local ice thickness and concentration. This can be parameterized as follows (Hibler, 1979):

$$P_{max} = P^{*}h\ \exp[-C(1-A)],$$

where P^{*} is the ice strength per meter ice thickness and C is the ice concentration parameter. Note that for typical values of C, P_{max} can be considered equal to zero for A equal to zero.

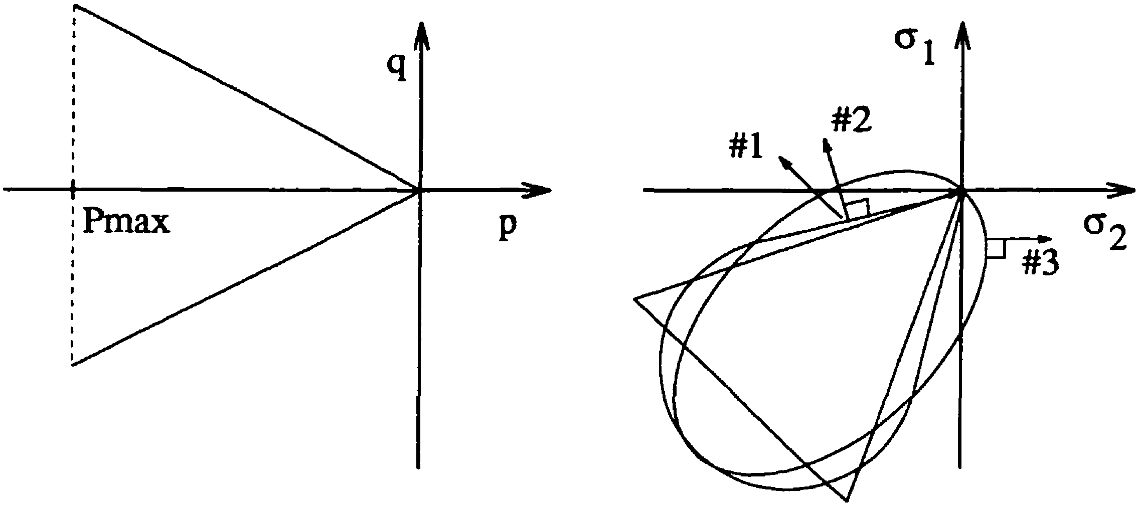

a) b)

Figure 2.5: Mohr-Coulomb failure criterion in stress invariant space, (a). Mohr-Coulomb failure criterion, and the ice-cream-cone and elliptical yield curve in principal stress space, (b). Note that the principal stress space is orientated at 45 degrees from the stress invariant space. Also, for $\dot{\Omega}_{i,j} = 0$, the principal axes of strain coincide with the principal axes of stress.

When p reaches this maximum value, the ice can no longer support the compressive load and the floes override each other, i.e. a ridge forms. The failure (yield) criterion described above (equation 2.15) is shown in figure 2.5a, in stress-invariant space, and in figure 2.5b, in principal stress space, and is equivalent to the straight portion of the ice-cream-cone yield curve, favoured by Coon (1974). The elliptical yield curve used by Hibler (1979) was chosen in an attempt to represent the ice-cream-cone yield curve of Coon, yet keeping mathematical simplicity. Note, however, that the ellipse lies in part in the positive principal stress quadrant and therefore has some tensile strength (cohesion).

The failure criterion marks the boundary between elastic and inelastic (plastic) behaviour of sea ice. When the stresses lie within the yield curve, sea ice behaves as an elastic solid and negligibly small deformation occurs; when the stresses lie on the yield curve, there are three possible motions: (1) sliding can take place along a sliding line (solid line in figure 2.5a), (2) ridging can occur when the maximum pressure is reached (dashed line in figure 2.5a) or (3) free drift can occur when all stresses are zero. From equation 2.16, the stress tensor in the x-y coordinate system can be written in terms of p and ψ as follows:

$$\boldsymbol{\sigma} = \begin{bmatrix} -(p - p\sin\phi\cos 2\psi) & p\sin\phi\sin 2\psi \\ p\sin\phi\sin 2\psi & -(p + p\sin\phi\cos 2\psi) \end{bmatrix}. \tag{2.18}$$

It remains to relate the angle ψ to the strain rate tensor $\dot{\epsilon}$ and to propose a closure scheme to solve for the pressure p. It should be appreciated that shear deformation along sliding lines leads to a rearrangement of the ice floes, and consequently, to a redistribution of the contact normal between individual floes. This causes a change in the material's resistance to shear deformation (a change in ϕ) and may lead to densification or dilatation (larger or smaller ice concentration) of the material, depending on the orientation of the contact normals. The next subsection discusses the link between the effective angle of friction (ϕ), the dilatation, and the resulting deformation in the ice field.

2.3.2 Dilatation

Deformation of a granular mass comes from the relative displacement of individual granules along planes tangent to the ice floes at an active contact normal (see dashed lines in figure 2.6). The angle between those planes (microscopic plane of motion) and the macroscopic sliding plane is called the angle of dilatancy and is denoted by δ. Normal forces at contacting points with positive angle of dilatancy (figure 2.6a) tend to oppose relative motion and contribute to the overall resistance of the material to shear deformation, and those with negative angle of dilatancy (figure 2.6b) tend to assist motion and reduce the resistance of the material to shear motion. Also, from the orientation of the microscopic plane of motion and the macrospcopic sliding plane, we note that a positive angle of dilatancy leads to a dilatation of the material (shear + divergence) whereas a negative angle of dilatancy leads to a densification of the material (shear + convergence). Therefore, the macroscopic angle of friction of a granular material (or its resistance to shear motion) depends not only on the type of material but also on the distribution of the contact normal, and is closely related to dilatation/densification; however, the microscopic angle of friction (μ) between two distinct floes is considered a constant property of the material.

A relationship between the effective angle of friction (ϕ), the ensemble average angle of

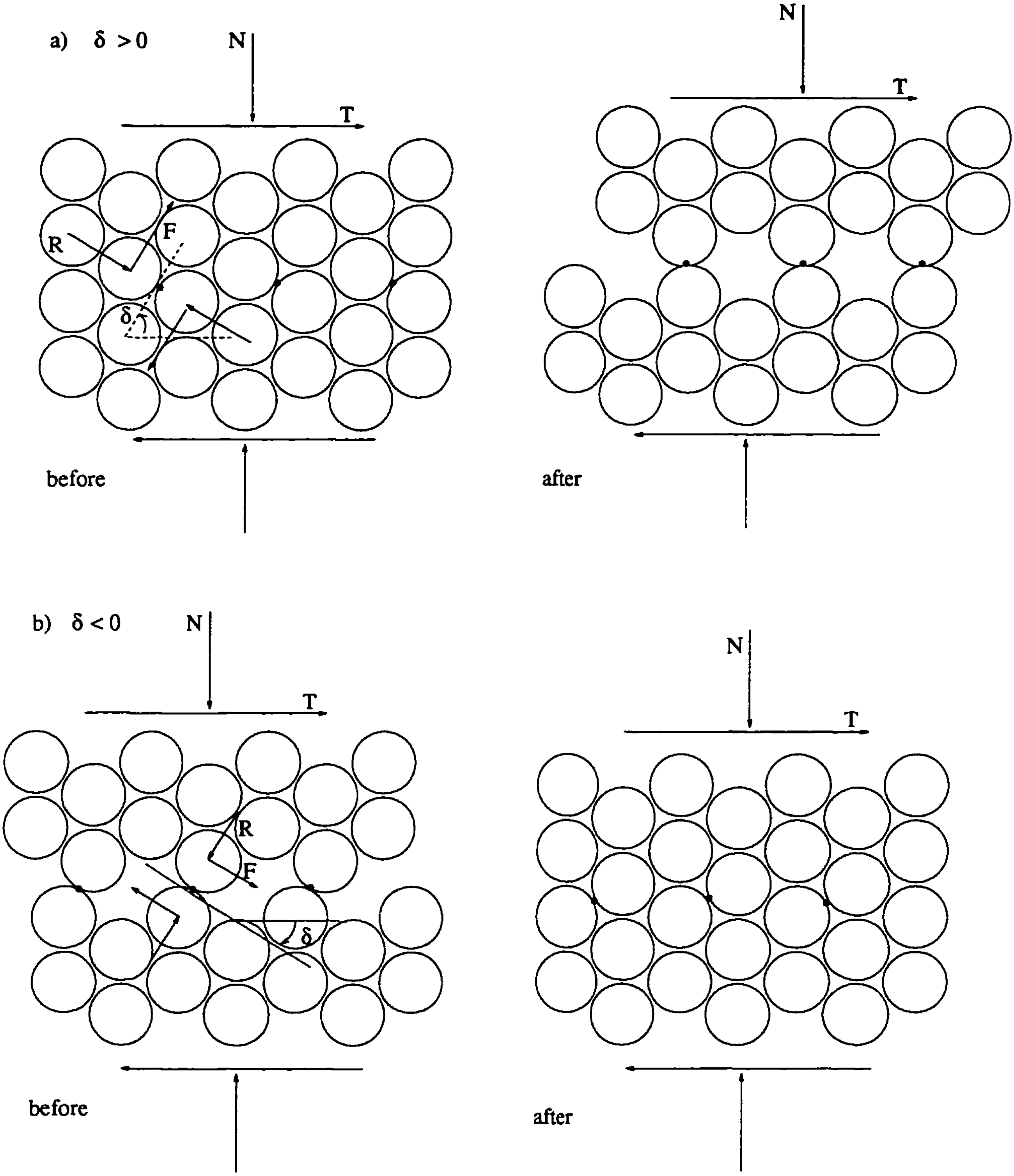

Figure 2.6: Forces acting on ice floes for positive, (a), and negative angle of dilatancy, (b).

dilatancy over a grid cell (δ) and the microscopic angle of friction (μ) is presented. For $\delta > 0$, the forces on the microscopic plane (R, F) can be written in terms of the forces in the macroscopic plane (N, T) as follows:

$$F = T\cos\delta - N\sin\delta, \qquad R = T\sin\delta + N\cos\delta, \tag{2.19}$$

where $T = A_s\tau_s$, $N = A_s\sigma_s$ and A_s is the area of the sliding plane. Similar relations can be written for a negative angle of dilatation. When sliding occurs, the frictional force F is related to the normal force R by (as in equation 2.15)

$$F = R\tan\mu. \tag{2.20}$$

From equations 2.17, 2.19 and 2.20, the macroscopic angle of friction (ϕ) can be related to the angle of dilatancy δ and the microscopic angle of friction (μ) by

$$\phi = \delta + \mu.$$

In the initial stage of deformation, more and more contact normals with positive angles of dilatancy are formed, while contact normals with negative angle of dilatancy are continually lost. This leads to an initial dilatation of the material (opening of leads) and an associated increase of resistance to shear motion (ϕ). With time, positive contact normals are eroded and the overall angle of dilatancy and macroscopic angle of friction remain constant. The possibility of detecting leads from SSM/I brigthness temperature data with a 10 km resolution (figure 2.2) shows that adjacent ice floes not only slide on one another along leads but also move apart, uncovering warm ocean water underneath. Sea-ice divergence calculated from synthetic aperture radar (SAR) images (Stern *et al.*, 1995) clearly indicate that opening and closing of leads is present during shear deformation. SAR images also show that some lead opening is due to tidal motions, which are not necessary associated with shearing motions. In this model, this effect comes naturally from considering the microscopic behaviour of sea ice in shear deformation and does not rely on parameterization.

To close the problem, an evolution equation for the effective angle of friction ϕ is required. Examples of evolution equations for various types of material are given in Balendran and Nemat-Nasser (1993). For this application, the effective angle of friction is assumed to have reached its saturation value and therefore it will be considered constant. This constant is set at 30 degrees, based on observation made by Overland and Pease (1988).

2.3.3 Constitutive relations

In this subsection, the constitutive equations relating the stresses ($\boldsymbol{\sigma}$) to the strain rates ($\dot{\boldsymbol{\epsilon}}$) are presented. The strain rate can be separated into a plastic and an elastic part ($\dot{\boldsymbol{\epsilon}} = \dot{\boldsymbol{\epsilon}}^p + \dot{\boldsymbol{\epsilon}}^e$). In the model proposed here, only the plastic deformations are kept since the elastic deformations are typically much smaller.

It is assumed that the plastic deformation is due to shearing along the sliding lines and that the rate of shearing is denoted by $\dot{\gamma}$. Note that the rate of shearing is the same on both sliding lines; this follows from the no rotation assumption $\dot{\boldsymbol{\Omega}} = \mathbf{o}$ (see beginning of subsection 2.3 above). Axial strain rate is also present on the sliding lines due to the dilatation/densification of the material. The resulting strain rate tensor in a coordinate system aligned along a sliding line ($\alpha = 1, 2$) takes the following form:

$$\dot{\boldsymbol{\epsilon}}^\alpha = \begin{bmatrix} 0 & \dot{\gamma} \\ \dot{\gamma} & \dot{\gamma}\tan\delta \end{bmatrix} \qquad \alpha = 1, 2. \tag{2.21}$$

The strain rate tensor in the x-y coordinate system is the sum of the $\dot{\boldsymbol{\epsilon}}^\alpha$, $\alpha = 1, 2$, rotated by an angle of $\psi \pm (\pi/4 - \phi/2)$, respectively. Depending on the value of δ, deformation varies from pure shear deformation ($\delta = 0$) to shear deformation with more or less divergence ($\delta > 0, \delta < 0$). This is shown graphically in figure 2.5b (#1) where the orientation of the arrow is such (45°) that the principal strains are equal in magnitude but opposite in sign (non-divergent flow, $\dot{\epsilon}_1 + \dot{\epsilon}_2 = 0$). By comparison, the normal flow rule (#2) used in conjunction with the Mohr-Coulomb yield curve, results in excessive dilatation (Spencer, 1964), with $\dot{\epsilon}_1$ positive and larger in magnitude than $\dot{\epsilon}_2$ ($\dot{\epsilon}_1 + \dot{\epsilon}_2 > 0$, divergent flow). When used with the elliptical yield curve, strong divergent flow results whenever the stress state lies in the first half of the ellipse, where the normal to the yield curve projects onto one or both positive principal strain axes (Figure 2.5b #3). This situation is not realistic and is avoided in the present model. Finally, it is interesting to note that the divergence associated with shearing motion is in effect a new thermodynamic source term in both continuity equations and provides a means of forming thicker ice without the need to ridge thick multi-year ice.

The following relationships can be derived from the total strain rate in the x-y coordinate system:

$$\begin{aligned}
\dot{\epsilon}_{kk} &= \dot{\gamma}\,\tan\delta, && (2.22)\\
\dot{\epsilon}_{11} - \dot{\epsilon}_{22} &= 2\dot{\gamma}\,\frac{\cos(\phi-\delta)}{\cos\delta}\cos 2\psi, && (2.23)\\
2\dot{\epsilon}_{12} &= 2\dot{\gamma}\,\frac{\cos(\phi-\delta)}{\cos\delta}\sin 2\psi. && (2.24)
\end{aligned}$$

From equations 2.23 and 2.24, the angle ψ can be written in terms of the deformation field in the following manner:

$$\tan 2\psi = \frac{2\dot{\epsilon}_{12}}{\dot{\epsilon}_{11} - \dot{\epsilon}_{22}}. \qquad (2.25)$$

This ratio of strain rates also measures the angle between the principal axes of strain rate and the x-y coordinate axes (see subsection 2.3.1). This indicates that the principal stress axes coincide with the principal strain rate axes; i.e., the extreme values of axial strain rates $(\dot{\epsilon}_1, \dot{\epsilon}_2)$ will occur where the extreme normal stresses (σ_1, σ_2) are acting. This is not precisely the case in practice, but follows from the no-rotation argument $\dot{\Omega} = o$. Finally, 2.22 can be used to close the system of equations and solve for p:

$$\dot{\epsilon}_{kk} = \dot{\gamma}\,\tan\delta, \quad \text{where} \quad 0 < p < P_{max}. \qquad (2.26)$$

In the above equation, $\dot{\gamma}$ is taken as the maximum shear strain acting at a point. For $\delta = 0$, the above equation reduces to the closure scheme proposed by Flato and Hibler (1992). Substituting 2.25 into 2.18, the final constitutive equations are obtained:

$$\sigma_{ij} = -p\delta_{ij} - \eta\dot{\epsilon}_{kk}\delta_{ij} + 2\eta\dot{\epsilon}_{i,j}$$

where

$$\eta = \min\left(\frac{2p\,\sin\phi}{\sqrt{(\dot{\epsilon}_{11} - \dot{\epsilon}_{22}) + 4\dot{\epsilon}_{12}}}, \eta_{max}\right).$$

For small deformation $(\dot{\epsilon}_1, \dot{\epsilon}_2)$, the coefficient of friction is constant $(\eta = \eta_{max})$ and sea ice behaves as a very viscous fluid.

2.4 Scale analysis

Non-dimensionalization of the governing equations gives a typical order of magnitude for each term by introducing appropriate scales for the various quantities involved [1]. This gives a basis for neglecting certain terms and allows for a simpler numerical schemes of the resulting set of equations.

The characteristic quantities for this problem are the ice thickness $[H]$, the length of the physical domain $[L]$, the ice and ocean current velocities $[U]$, the wind speed $[U_a]$, various temperature differences $[\Delta T]$ and the characteristic time associated with the momentum and thermodynamic $[t_f]$ forcing. Thus we write $u_i = [U]u_i{}^*$, $u_a = [U_a]u_a{}^*$ etc., where the starred quantities are dimensionless and of order one in magnitude. A summary of the characteristic scales and physical parameters and constants used in this study is presented in Table 2.1 and appendix A. The momentum equation 2.1 can be written in terms of the starred variables as follows (the order of magnitude of each term is given below):

$$\underbrace{\frac{\rho_i[H][U]}{[t_f]}}_{10^{-4}\mathrm{N/m^2}}\, h^* \frac{\partial \boldsymbol{u}_i{}^*}{\partial t^*} + \underbrace{\frac{\rho_i[H][U]^2}{[L]}}_{10^{-5}\mathrm{N/m^2}} h^* \boldsymbol{u}_i^* \nabla \boldsymbol{u}_i^* \;=\; \underbrace{-\rho_i[H]f[U]}_{10^{-2}\mathrm{N/m^2}} h^* \boldsymbol{k} \times \boldsymbol{u}_i^* + \underbrace{\rho_a C_{da}[U_a]^2 A}_{10^{-2}\mathrm{N/m^2}} \boldsymbol{\tau}_a^* -$$

$$\underbrace{\rho_w C_{dw}[U]^2 A}_{10^{-2}\mathrm{N/m^2}} \boldsymbol{\tau}_w^* + \underbrace{\frac{P_{max}[H]}{[L]}}_{10^{-2}\mathrm{N/m^2}} \nabla \boldsymbol{\sigma}^* - \underbrace{\rho_i[H]f[U]}_{10^{-2}\mathrm{N/m^2}} h^* \boldsymbol{\nabla} H_d^*.$$

This indicates that each term can potentially be important in large scale sea ice dynamic problem, except for the advection term which only becomes significant for much smaller length scale (< 1 km). Also, for wind forcing averaged over 5 days (4×10^5 sec) or more, the acceleration term can be neglected; i.e. the ice is in balance with the external forcing. Note that the Coriolis effect should be considered in sea ice simulation of the Arctic, unlike in Antarctica where the ice thickness is approximately 70 cm and only accounts for approximately 10 % of the momentum balance (Martinson and Wamser, 1990). So, for large scale climate studies in the Arctic using monthly mean wind stresses and time-independent ocean current, both the acceleration and the advective term can be safely neglected in the momentum equations.

---

[1] Note that the scaling parameters are chosen such that the resulting non-dimensional variables vary between 0 and 1.

Table 2.1: Characteristic quantities involved in the governing equations.

Variable	symbol	value
Ice concentration	A	1
Ice thickness	$[H]$	5°m
Length	$[L]$	10^6 m
Thermodynamic ice concentration growth	$[S_A]$	0.1 day^{-1}
Thermodynamic ice thickness growth	$[S_h]$	1 cm/day
Forcing time scale	$[t_f]$	3 months
Ice and ocean velocity	$[U]$	5 cm/sec
Wind speed	$[U_a]$	5 m/s
Incoming shortwave radiation	$[Q_{sw}]$	350 W / m^2
Cutoff thickness between thick and thin ice	h_0	10 cm
Ice-atmosphere specific humidity difference	$[\Delta q_{ia}]$	1×10^{-4}
Ocean-atmosphere specific humidity difference	$[\Delta q_{oa}]$	1×10^{-3}
Horizontal temperature difference	$[\Delta T_h]$	5 Celsius
Vertical temperature difference	$[\Delta T_v]$	30° Celcius
Atmosphere temperature difference	$[\Delta T_a]$	30° Celcius
Land temperature difference	$[\Delta T_l]$	5° Celcius
Ocean temperature difference	$[\Delta T_o]$	5° Celcius
Ice-atmosphere temperature difference	$[\Delta T_{ia}]$	2° Celsius
Ocean-ice temperature difference	$[\Delta T_{oi}]$	1° Celsius
Ocean-atmosphere temperature difference	$[\Delta T_{oa}]$	30° Celsius

The continuity equations (equations 2.4 and 2.5) for sea ice can be written in non-dimensional form as follows:

$$\underbrace{\frac{[H]}{[t_f]}}_{1\mathrm{cm/day}} \frac{\partial h^*}{\partial t^*} + \underbrace{\frac{[H][U]}{[L]}}_{1\mathrm{cm/day}} \nabla \cdot h^* u_i^* = \underbrace{[S_h]}_{1\mathrm{cm/day}} S_h^* + \underbrace{\frac{K_h[H]}{[L]^2}}_{10^{-3}\mathrm{cm/day}} \nabla^2 h^* \tag{2.27}$$

$$\underbrace{\frac{1}{[t_f]}}_{10^{-1}\mathrm{day}^{-1}} \frac{\partial A}{\partial t^*} + \underbrace{\frac{[U]}{[L]}}_{10^{-2}\mathrm{day}^{-1}} \nabla \cdot A u_i^* = \underbrace{[S_A]}_{10^{-1}\mathrm{day}^{-1}} S_A^* + \underbrace{\frac{K_A}{[L]^2}}_{10^{-5}\mathrm{day}^{-1}} \nabla^2 A \tag{2.28}$$

In equation 2.27, a characteristic ice buildup of 70 cm over 2 months is used to evaluate the time dependent term (Maykut and Untersteiner, 1971). The scaling of the continuity equations shows that both thermodynamic and dynamic processes are equally important in the growth of mean sea ice thickness, whereas thermodynamic effects dominates in the ice concentration evolution equation for an ocean-atmosphere heat flux characteristic of winter conditions. In 2.27 and 2.28, the diffusion terms are only non-negligible when large gradients are present over length scale comparable to the grid size ($\approx$ 100 km). The characteristic source terms S_h and S_A in the above equation are obtained from a heat budget calculation made over the Arctic (Maykut and Untersteiner, 1971). The same results can obtained from equations 2.6, 2.7 and 2.32.

The non-dimensional ice energy equation (2.10) can be written as follows

$$\underbrace{\frac{\rho_i C_{pi}[\Delta T_v]}{[t_f]}}_{10^0\mathrm{W/m^3}} \frac{\partial T_i^*}{\partial t^*} + \underbrace{\frac{\rho_i C_{pi}[\Delta T_h][U]}{[L]}}_{10^{-1}\mathrm{W/m^3}} \nabla \cdot (\boldsymbol{u}_i^* \, T_i^*) = \underbrace{\frac{K_i[\Delta T_h]}{[L]^2}}_{10^{-11}\mathrm{W/m^3}} \nabla^2_{2D} T_i^* + \underbrace{\frac{K_i[\Delta T_v]}{[H]^2}}_{10^0\mathrm{W/m^3}} \frac{\partial^2 T_i^*}{\partial z^{*2}}$$

In this equation, the horizontal diffusion of heat term is always negligible compared to the vertical one due to the large aspect ratio of the sea ice cover. The advective term can also be ignored for typical horizontal temperature gradients present in the central Arctic. In the ice edge region, these gradients can be much larger, but the ice is much thinner and the advective term is still negligible in front of the vertical diffusion of heat term. For large ice thickness ($[H] = 5$m), the time dependent term and the vertical heat transfer by conduction through the ice are of the same order of magnitude; i.e. the heat storage in the ice is non-negligible. For ice thickness smaller than 2.5 m, the vertical diffusion of heat term is one order of magnitude larger and the steady state assumption is valid. In the present work, the time dependent term is neglected in the ice energy equation. This is valid for a large part of the Arctic; however, in some regions, the ice can be as thick as 6 m, and this simplification is expected to result in a slight shift in the phase of the seasonal cycle (Holland, 1993).

The scaled energy equations for the atmosphere ($\lambda = 1$), ocean and land (equations 2.11–2.13) are presented together:

$$\begin{aligned}
\rho_a C_{pa} H_a \left(\underbrace{\frac{[\Delta T_a]}{[t_f]}}_{10^1\,\mathrm{W/m^2}} \frac{\partial T_a^*}{\partial t^*} + \underbrace{\frac{[U_a][\Delta T_h]}{[L]}}_{10^2\,\mathrm{W/m^2}} \nabla \cdot (\boldsymbol{u}_a^* T_a^*) \right) &= \underbrace{(1-A)Q_{oa}}_{10^1\,\mathrm{W/m^2}} + \underbrace{AQ_{ia}}_{10^2\,\mathrm{W/m^2}} \qquad (2.29)\\
&\quad - \underbrace{Q_{lw-out}}_{10^2\,\mathrm{W/m^2}} + \underbrace{\frac{K_a[\Delta T_h]}{[L]^2}}_{10^1\,\mathrm{W/m^2}} \nabla^2 T_a^*,\\
\rho_w C_{pw} H_o \left(\underbrace{\frac{[\Delta T_o]}{[t_f]}}_{10^2\,\mathrm{W/m^2}} \frac{\partial T_o^*}{\partial t^*} + \underbrace{\frac{[U][\Delta T_h]}{[L]}}_{10^2\,\mathrm{W/m^2}} \nabla \cdot (\boldsymbol{u}_w^* T_o^*) \right) &= \underbrace{-(1-A)Q_{oa}}_{10^1\,\mathrm{W/m^2}} - \underbrace{AQ_{oi}}_{10^2\,\mathrm{W/m^2}} \qquad (2.30)\\
&\quad + \underbrace{Q_{upwelling}}_{10^0\,\mathrm{W/m^2}} + \underbrace{\frac{K_o[\Delta T_h]}{[L]^2}}_{10^{-2}\,\mathrm{W/m^2}} \nabla^2 T_o^*,\\
\underbrace{\frac{\rho_l C_{pl}[\Delta T_l]}{t_f} \frac{\partial T_l}{\partial t}}_{10^1\,\mathrm{W/m^3}} &= \underbrace{\frac{K_l[\Delta T_h]}{[L]^2}}_{10^{-11}\,\mathrm{W/m^3}} \nabla^2_{2D} T_l^* \qquad (2.31)\\
&\quad + \underbrace{\frac{K_l[\Delta T_v]}{[H_l]^2}}_{10^1\,\mathrm{W/m^3}} \frac{\partial^2 T_l^*}{\partial z^{*2}}
\end{aligned}$$

The order of magnitude of the terms on the left hand side of the above equations include the thermal capacity of the material ($\rho C_p H$); the terms on the right hand side are described in more details in the next paragraph. For time scales associated with the thermodynamic forcing larger than 10 days, the time dependent term in the atmosphere energy equation is negligible; i.e. the atmosphere is always in equilibrium with its surrounding. This is due to its low thermal capacitance. In the ocean and land case, the thermal inertia is much larger and the time dependent terms remain. In this thesis, the time dependent term in the energy equation for the atmosphere will be neglected. This fact will be used later to obtain a simpler numerical solution of the ice-ocean-atmosphere system. The order of magnitude of the terms on the right hand side of the equations are evaluated as follows (see equation

2.8):

$$\begin{aligned}
Q_{oa} &= \underbrace{4\sigma T_{fp}^3[\Delta T_{oa}]}_{10^2\,\mathrm{W/m^2}}(T_o^* - T_a^*) + \underbrace{\rho_a C_{pa} C_{sens}[U_a][\Delta T_{oa}]}_{10^2\,\mathrm{W/m^2}}(T_o^* - T_a^*) + \underbrace{\rho_a C_{lat}[U_a] L_e[\Delta q]}_{10^1\,\mathrm{W/m^2}} Q_{lat}^* \\
&\quad + \underbrace{Q_0(1-\alpha_a)(1-a_a)(1-\alpha_o)}_{10^2\,\mathrm{W/m^2}} Q_{sw}^*, \\
Q_{oi} &= \underbrace{\rho_w C_{pw} C_{sens}[U][\Delta T_{oi}]}_{10^2\,\mathrm{W/m^2}}(T_i^* - T_o^*), \qquad (2.32) \\
Q_{ia} &= \underbrace{4\sigma T_{fp}^3[\Delta T_{ia}]}_{10^1\,\mathrm{W/m^2}}(T_i^* - T_a^*) + \underbrace{\rho_a C_{pa} C_{sens}[U_a][\Delta T_{ia}]}_{10^1\,\mathrm{W/m^2}}(T_i^* - T_a^*) + \underbrace{\rho_a C_{lat}[U_a] L_s[\Delta q]}_{10^0\,\mathrm{W/m^2}} Q_{lat}^* \\
&\quad + \underbrace{Q_0(1-\alpha_a)(1-a_a)(1-\alpha_i)}_{10^2\,\mathrm{W/m^2}} Q_{sw}^*,
\end{aligned}$$

where the difference in longwave radiation terms are linearized about the ocean freezing point temperature T_{fp}. The estimates of the various heat flux components are in good agreement with measurements made in the Arctic (Maykut and Untersteiner, 1971).

Chapter 3

Numerical scheme

The numerical scheme used to solve the governing equations for the thermodynamics of the atmosphere, ice, ocean and land is presented in this section. Since the time dependent terms in the ice momentum equation and the atmospheric energy equation are neglected, the ice field and the atmosphere are always in balance with the external forcing. In addition, the coupling between the atmosphere, ice and ocean model components is only through the thermodynamic equations as the wind and ocean currents are prescribed quantities. These restrictions greatly simplify the solution procedure. The ice thickness, concentration and ocean temperature fields are first calculated by time stepping the continuity equations (2.4 and 2.5) and the ocean energy equation 2.12. Given the h and A fields, the ice velocity field satisfying the momentum equations (2.1) can be calculated. The ice surface, land surface and atmosphere temperature are obtained in a similar manner from the new T_o field. The grid used in this model is the Arakawa C-grid, where all the scalar quantities are positioned in the centre and the vector quantities on the sides (see figure 3.1-a). This allows the conservation of mass equation to be solved using a mass-conserving numerical scheme.

3.1 Momentum equation

The description of the numerical solution for the momentum equation parallels the one used in Flato and Hibler (1992). The ice thickness and concentration used in the solution of the momentum equation are first calculated from equations 2.4 and 2.5 using a simple forward-

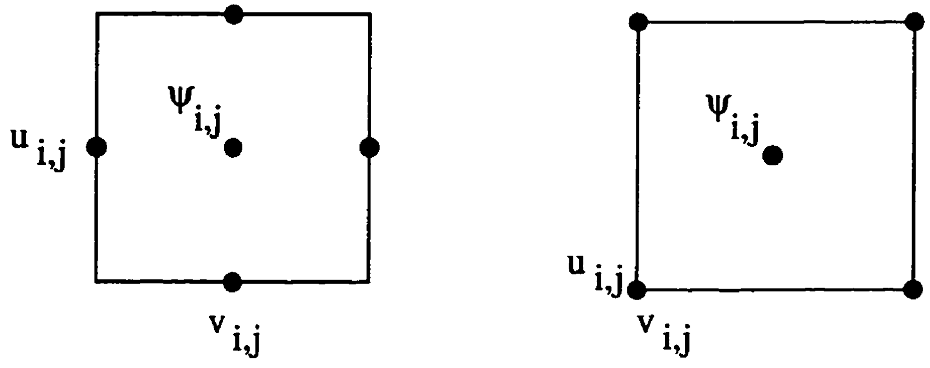

a) b)

Figure 3.1: Location of the scalar and vector quantities on the Arakawa C-grid, (a), and B-grid, (b). Ψ can represent the mean ice thickness (h), ice concentration (A), air temperature (T) and internal ice pressure (p).

in-time, upwind finite-difference scheme. Neglecting the acceleration term and expressing the sea surface tilt in terms of the geostrophic ocean current ($f\boldsymbol{u}_w^g = g\ \boldsymbol{k} \times \nabla H_d$), the momentum equation (2.1) can be written as follows:

$$A(\boldsymbol{u}_i - \boldsymbol{u}_w^g) = \boldsymbol{R} - \nabla p + \nabla \cdot \boldsymbol{\sigma}' \tag{3.1}$$

where $\boldsymbol{R}$ is the wind forcing term and $-\nabla p + \nabla \cdot \boldsymbol{\sigma}'$ the ice interaction term. The matrix and vectors can be written as follows:

$$A = \begin{pmatrix} C'_{dw} \cos\theta_w & -\rho_i h f - C'_{dw} \sin\theta_w \\ \rho_i h f + C'_{dw} \sin\theta_w & C'_{dw} \cos\theta_w \end{pmatrix} \qquad \boldsymbol{R} = \begin{pmatrix} C'_{da}(u_a \cos\theta_a - v_a \sin\theta_a) \\ C'_{da}(v_a \cos\theta_a + u_a \sin\theta_a) \end{pmatrix}$$

$$\boldsymbol{F} = \begin{pmatrix} \dfrac{\partial}{\partial x}\left[\eta\left(\dfrac{\partial u}{\partial x} - \dfrac{\partial v}{\partial y}\right)\right] + \dfrac{\partial}{\partial y}\left[\eta\left(\dfrac{\partial u}{\partial y} + \dfrac{\partial v}{\partial x}\right)\right] \\ \\ \dfrac{\partial}{\partial x}\left[\eta\left(\dfrac{\partial u}{\partial y} + \dfrac{\partial v}{\partial x}\right)\right] + \dfrac{\partial}{\partial y}\left[\eta\left(\dfrac{\partial u}{\partial x} - \dfrac{\partial v}{\partial y}\right)\right] \end{pmatrix} .$$

where $\boldsymbol{F} = \nabla \cdot \boldsymbol{\sigma}'$. We now seek an ice velocity field satisfying equation 3.1, subject to the restrictions on the pressure field (equation 2.26). This is done in three steps. First, the free drift velocities[1] $\boldsymbol{u}_i^{fd}$ are calculated, and then used as an initial approximation to the solution

---

[1] the solution of 3.1 without the ice interaction term included

of the momentum equation 3.1. Second, the free drift velocities and associated pressure field ($p = 0$, everywhere) are corrected using equation 2.26 and considering the term $\nabla \cdot \boldsymbol{\sigma}'$ to be constant. Finally, the friction term is considered and the velocity field is calculated considering the pressure to be known. The resulting velocity field will not necessarily satisfy the restriction on pressure, and iteration between the second and the third step is therefore necessary.

The free drift velocity can be calculated directly using the B-grid (Figure 3.1b), where both components of the ice velocity are co-located, with knowledge of the wind and ocean currents at each node of the domain. In addition, the part of the forcing which is independent of the ice velocities can be calculated from the free drift velocities in the following manner:

$$\boldsymbol{R}' = \boldsymbol{R} + A\boldsymbol{u}_w^g = A\boldsymbol{u}_i^{fd}.$$

$\boldsymbol{R}'$ and $\boldsymbol{u}_i^{fd}$ are then interpolated onto the C-grid for subsequent use in the numerical scheme. The momentum equations now take the form:

$$A\boldsymbol{u}_i = \boldsymbol{R}' - \nabla P + \nabla \cdot \boldsymbol{\sigma}'. \qquad (3.2)$$

As a second step, the free drift solution is modified to satisfy both the equation of motion (3.2) and the restriction equation 2.26. More generally, any initial guess ($\overline{\boldsymbol{u}}_i$ and $\overline{p}$) satisfying equation 3.2 can be used as a starting point. Substituting the corrected fields ($\boldsymbol{u}_i = \overline{\boldsymbol{u}}_i + \boldsymbol{u}_i'$ and $p = \overline{p} + p'$) into the equation of motion (3.2) and subtracting the basic state, the equation for the velocity correction can be written as:

$$A\boldsymbol{u}_i' = -\nabla p', \qquad \text{or} \qquad \boldsymbol{u}_i' = -\frac{\nabla p'}{C_{dw}' \cos\theta}. \qquad (3.3)$$

The frictional term ($\nabla \cdot \boldsymbol{\sigma}'$) and the off-diagonal terms of matrix A are considered temporarily constant and therefore are not part of the perturbed solution. Their effect will be considered later in the solution. Upon substituting (3.3) into (2.26), the pressure field can be calculated by solving

$$\nabla \cdot \left(\frac{\nabla p'}{C_{dw}' \cos\theta} \right) = -\nabla \cdot \overline{\boldsymbol{u}}_i + \dot{\gamma} \tan\delta.$$

For a simplified situation where δ is set equal to zero, this scheme will adjust the pressure p in order to obtain a non-divergent velocity field. In the limit where the ice is infinitely strong in tension and compression, the final solution would be non-divergent. In practice, the ice has a finite strength in compression and little or no resistance in tension; for these reasons, regions of convergence and divergence will exist in the solution domain. If dilatation is considered ($\delta \neq 0$), the flow field can be divergent and the pressure still positive. This would be observed when shearing occurs along sliding lines due to the rearrangement of the floes. In finite-difference form, the left hand side of the above equation is written in the following manner:

$$\nabla \cdot \left(\frac{\nabla p'}{C'_{dw} \cos\theta} \right) = \frac{1}{\Delta^2} \left[\frac{p'_{i+1,j} - p'_{i,j}}{\zeta^x_{i+1,j}} - \frac{p'_{i,j} - p'_{i-1,j}}{\zeta^x_{i,j}} \right. \tag{3.4}$$

$$\left. + \frac{p'_{i,j+1} - p'_{i,j}}{\zeta^y_{i,j+1}} - \frac{p'_{i,j} - p'_{i,j-1}}{\zeta^y_{i,j}} \right] \tag{3.5}$$

where Δ is the grid size and, $\zeta^x_{i,j} (= C'_{dw} \cos\theta)$ and $\zeta^y_{i,j}$ the diagonal components of the matrix A evaluated on the vertical and horizontal side of the grid, respectively. This equation is solved using a relaxation technique where the pressure p is considered zero except at the point of interest (i,j). From these considerations, the correction on $p_{i,j}$ can be written as follows:

$$p'_{i,j} = \Delta^2 \ (-\nabla \cdot \overline{\boldsymbol{u}}_i + \dot{\gamma} \ \tan\delta) \left(\frac{1}{\zeta^x_{i+1,j}} + \frac{1}{\zeta^x_{i,j}} + \frac{1}{\zeta^y_{i,j+1}} + \frac{1}{\zeta^y_{i,j}} \right)^{-1}$$

The correction on the velocities follows from equation 3.3:

$$u'_{i,j} = -\frac{1}{\zeta^x_{i,j}} \frac{p'_{i,j}}{\Delta}, \qquad u'_{i+1,j} = \frac{1}{\zeta^x_{i+1,j}} \frac{p'_{i,j}}{\Delta},$$

$$v'_{i,j} = -\frac{1}{\zeta^y_{i,j}} \frac{p'_{i,j}}{\Delta}, \qquad v'_{i+1,j} = \frac{1}{\zeta^y_{i,j+1}} \frac{p'_{i,j}}{\Delta}.$$

In the above expressions the subscript i for ice was omitted to make the notation clearer.

The current value of pressure p or velocity $\boldsymbol{u}_i$ is the sum of the initial value and the correction p' or $\boldsymbol{u}'_i$. However, certain restrictions must be imposed on the pressure p (see equation 2.26). If the pressure exceeds the maximum value in compression (P_{max}), the correction must be set equal to $P_{max} - p$ to avoid exceeding the maximum allowable value. This will result in convergence in that grid cell. If the pressure p becomes negative (tensile stress), the correction must be set equal to $-p$, resulting in a zero final pressure and divergence in that grid cell. Note that the friction term was not considered in the computation of the pressure or velocity fields. Consequently, a new correction to the velocity field is required taking into account the newly computed pressure field. This is done using the following finite-difference form of the ice interaction term. For instance, the two terms in the x-component of the F term can be written as follows:

$$\begin{aligned} F_1 &= \frac{1}{\Delta}\left[\eta^c_{i,j}\left(\frac{u_{i+1,j}-u_{i,j}}{\Delta}-\frac{v_{i,j+1}-v_{i,j}}{\Delta}\right)-\eta^c_{i-1,j}\left(\frac{u_{i,j}-u_{i-1,j}}{\Delta}-\frac{v_{i-1,j+1}-v_{i-1,j}}{\Delta}\right)\right], \\ F_2 &= \frac{1}{\Delta}\left[\eta^n_{i,j+1}\left(\frac{u_{i,j+1}-u_{i,j}}{\Delta}+\frac{v_{i,j+1}-v_{i-1,j+1}}{\Delta}\right)-\eta^n_{i,j}\left(\frac{u_{i,j}-u_{i,j-1}}{\Delta}+\frac{v_{i,j}-v_{i-1,j}}{\Delta}\right)\right], \end{aligned}$$

where η^c and η^n are the coefficients of friction evaluated at the center of the grid cell and the node respectively. Similar expressions can be derived for the F_y component. Writing the complete momentum equation in finite-difference form, the velocity field can be calculated from the following:

$$A\begin{pmatrix} u_{i,j} \\ v_{i,j} \end{pmatrix} = \boldsymbol{R}'',$$

where $\boldsymbol{R}''$ comprises all the forcing terms and the off-diagonal velocity terms independent of $\boldsymbol{u}_{i,j}$. Again, this is solved using a relaxation technique on the above equation. Since the resulting velocity field will not satisfy the restriction on pressure imposed by the closure scheme 2.26, it is necessary to iterate a few times (about 3) between the two algorithms.

3.2 Energy equations

The ocean temperature is updated from the various atmosphere-ocean and ice-ocean heat fluxes using a simple forward-in-time finite difference method. The atmosphere and ice surface temperatures are then calculated using the new ocean temperature field. The forcing terms for the atmosphere are linearized about their values at the previous time step and can all be written in terms of the atmospheric temperature T_a, the ocean temperature T_o, the ice and land surface temperatures T_i and T_l, and the ice base temperature T_{ib}. In the following, the ice base temperature is assumed to be equal to the ocean temperature. As a result, sensible heat transfer between the ice and the ocean only occurs when the ocean temperature rise above the ice melting point. Furthermore, the ice surface temperature can be expressed in terms of the atmospheric temperature as follows (see equation 2.10):

$$\begin{aligned} -K_i \frac{T_i - T_o}{h/A} &= Q_{ia} = a_o + a_1 T_i - a_2 T_a, \\ T_i &= \frac{-a_o + a_2 T_a + K_i A T_o / h}{K_i A/h + a_1}. \end{aligned} \tag{3.6}$$

A similar expression can be derived for the land surface temperature. The atmosphere energy equation now constitutes a linear advection-diffusion equation in T_a of the form:

$$\boldsymbol{A T_a} = \boldsymbol{R}''''$$

where $\boldsymbol{R}''''$ represents the total heat fluxes from the surface to the atmosphere. This equation is solved using the Alternating Direction Implicit (ADI) method (see Press *et al.* (1990)). In the first substep, we solve for the temperatures in the even rows (x-direction) of the physical domain assuming the odd row (y-direction) temperatures are known. The same approach is then used for the odd row, even column and odd column temperatures. The advantage of this method is that each substep requires only the solution of a tri-diagonal matrix which, can be easily solved by standard techniques. After a few iterations, the solution converges to the required accuracy (0.1°). Once the atmospheric temperature is known, the ice and land surface temperature can be easily calculated (eg., see equation 3.6).

Chapter 4

Results

Results from a simulation of the sea-ice cover over a seasonal cycle in the Arctic Ocean and surrounding seas using this model are presented in this section. A Cartesian mesh with a grid resolution of 111 km is used on a polar stereographic projection of the physical domain (see Figure 4.1). At high latitudes, the variation of the Coriolis parameter with latitude is small and the f-plane approximation is used. The model is forced with prescribed climatological monthly mean wind stresses, obtained from the 1959-89 NMC sea level pressure analysis. These stresses are assumed to represent the mid-month situation. The wind stress field at a particular day is calculated from a linear interpolation of the two closest mid-month values. Figure 4.2 shows the annual mean climatology for this period as an example. Spatially varying, but steady ocean currents (see figure 4.3) were calculated from a single layer reduced gravity model, appropriate for large scale flows, in which the acceleration term in the momentum equation is ignored, friction is represented using a linear drag law and, the normal velocity component is specified at open boundaries (see appendix B for more details). In the Bering Strait, the normal velocity was chosen so as to obtain a constant inflow of 1 SV into the Arctic, and the velocity field in the North Atlantic was specified from Levitus sea surface elevation data and scaled in such a way as to obtain no accumulation of water in the Arctic domain. Finally, the solar forcing is the daily averaged value corrected for an 80 % cloud cover (Laevastu, 1960).

The boundary conditions for the ice dynamic equations are zero normal and tangential velocity at a solid boundary and free outflow at an open boundary (Hibler, 1979). For the

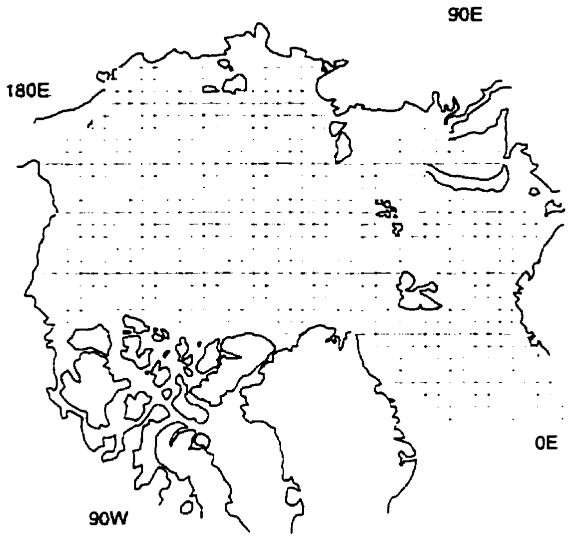

Figure 4.1: Computational grid used in the simulation.

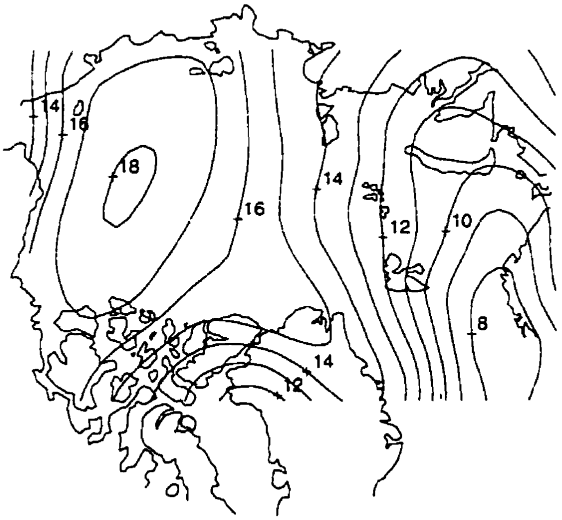

Figure 4.2: Sea level pressure annual mean climatology (minus 1000mb).

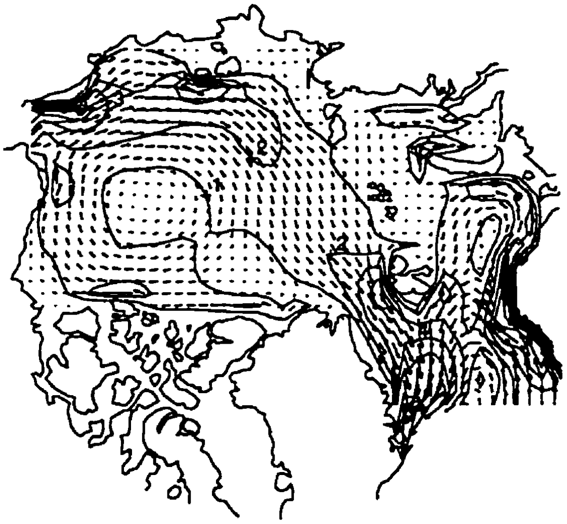

Figure 4.3: Upper ocean currents used in the simulations

atmospheric thermodynamic equations, the temperature at the boundary is specified from monthly climatology. The temperature at a given day is calculated as a weighted average of the mid-month climatological values. These temperatures were calculated from the NMC 850 mb height and temperature fields, assuming a linear temperature profile from the 1013 mb and 850 mb levels. For the ocean, the temperatures at open boundaries are also specified from monthly climatologies extracted from the Levitus data. At continental boundaries, the ocean heat flux is considered zero (a continent is regarded as a perfect insulator).

In this study, an attempt was made to include the effect of surface roughness in the drag coefficients. Quadratic drag coefficients ranging from 1 to 6 $\times 10^{-3}$ were measured in the last 30 years with the more recent measurements being at the upper end of this range. This is explained by the fact that the measurements have been made over increasingly rough surfaces and perhaps under increasingly unstable stratifications conditions (Smith, 1990). Since the surface roughness depends on ridging intensity, which in turn influences ice thickness, both the air-ice and ocean-ice drag coefficient are assumed to vary linearly with ice thickness (Tremblay and Mysak, 1997 in press). The latter paper has been included in appendix D. A list of all the physical parameters and constants used in the simulations are given in appendix A. Finally, the internal angle of friction is considered constant and equal to 30 degrees.

The model was integrated for 10 years to reach a stable seasonal cycle using a 1-day time step. The results shown are the simulated March lead pattern, the annual mean climatological ice velocity field, the mid-month March and September ice thickness distributions, which also include the ice edge position for these months. The effect of dilatation, associated with shearing deformation, on ice thickness distribution is also discussed for the mid-March results. Calculated atmosphere and ocean mid-March temperature fields are also presented. The model results are compared with sonar data for ice thickness, buoy data for ice velocity fields, satellite data for ice extent, NMC data for the atmosphere temperature and Levitus data for the ocean temperature. It should be noted that the observations are often limited or not of perfect quality, as in the case of ice thickness data and, air and ocean temperatures data.

4.1 Lead pattern and ice velocity field

In the continuum approach used here, we do not keep track of the exact position of each ice floe for all time, and consequently, the exact position of leads and sliding of groups of floes relative to one another cannot be resolved. Instead leads will appear as regions where large shear strain rates are present. In order to evaluate the ability of the model to reproduce the observed large scale lead patterns (figure 2.2b), a shear strain rate map is shown in figure 4.4 for mid-March. Of particular interest is the shear band extending from the western Canadian Arctic Archipelago (Prince Patrick Island) to the north pole. This modelled feature agrees extremely well with the observed lead seen in the SSMI satellite observations (figure 2.2-c). North of Greenland, no shear lines are present. There, the flow is unbounded to the east and the shear force required to induce sliding motion is much smaller. For this reason, it does not show up as a distinct feature in the observations and model results.

The simulated annual mean velocity field is shown in figure 4.5-a, along with an annual climatological velocity pattern derived from buoy drift measurements from the Arctic Buoy Program (figure 4.5-b). Qualitatively speaking, the Beaufort Gyre and the Transpolar Drift Stream are well simulated, with however, the center of the Gyre positioned slightly westward from its climatological location. Model results obtained with the Bering Strait closed (not shown here) depict the Beaufort Gyre centre to be quite westward of its observed

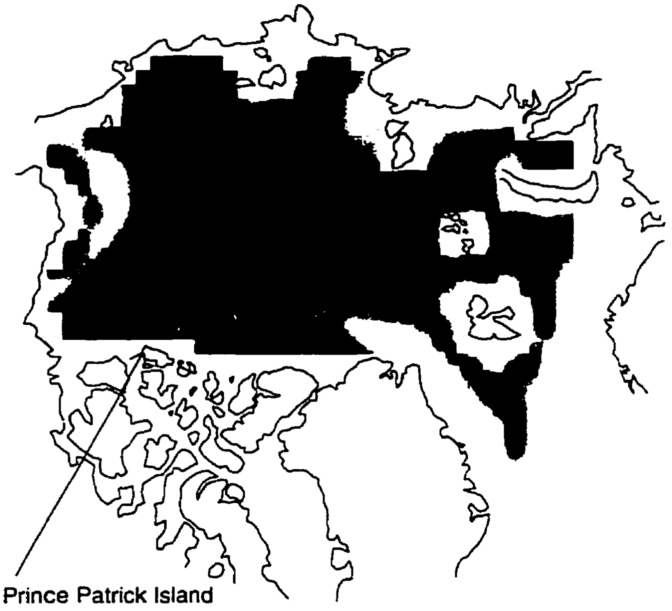

Figure 4.4: Shear strain rate color map. Regions of high shear strain rate are indicated by the lightly shaded area.

position. The opening of the Bering Strait significantly improves the simulation and plays an important role in determining the velocity field in the east Siberian side of the Gyre. It is important to note that the model produces a wedge of very slowly moving ice at the dividing line between the ice caught in the Beaufort Gyre and that leaving the Arctic through Fram Strait. In this region, we often have creeping flow which occurs when only small deformations in the ice field are present. In this figure, the region of high shear strain rate is also apparent at the interface between the relatively fast moving ice of the Beaufort Gyre and the relatively still ice north of Greenland. The ice velocity in the gyre is of the order of 2 to 3 cm/sec in agreement with measurements by Colony and Thorndike (1984), who quote an average value of about 2.5 cm/sec. The ice coming out of the Arctic through Fram Strait has a typical velocity of 5 cm/sec, which is also in good agreement with observations.

4.2 March ice thickness and concentration fields

Figure 4.6 shows the simulated mid-March thickness distribution in the Arctic, which can be compared with the sonar measurements reported by Bourke and Garrett (1987).

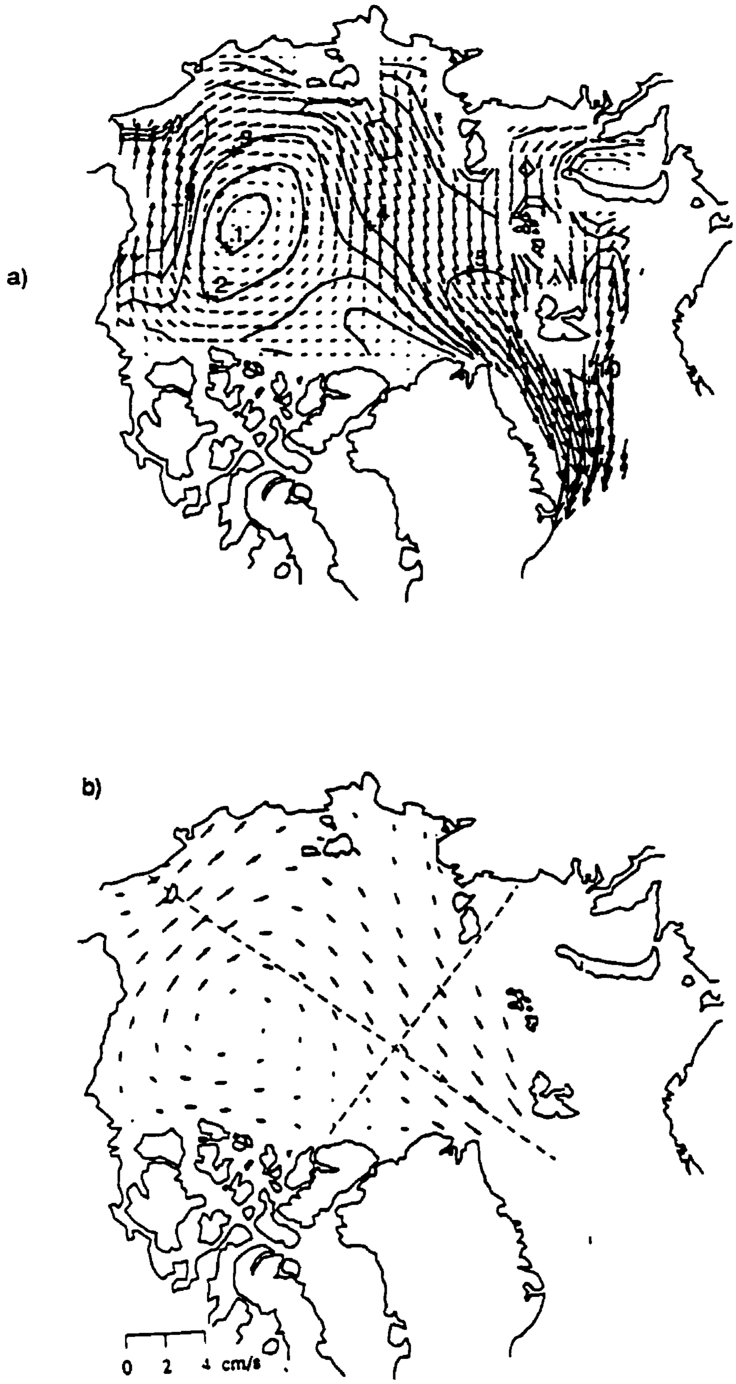

Figure 4.5: Simulated, (a), and observed (adapted from Colony and Thorndike, 1984), (b), annual mean velocity field.

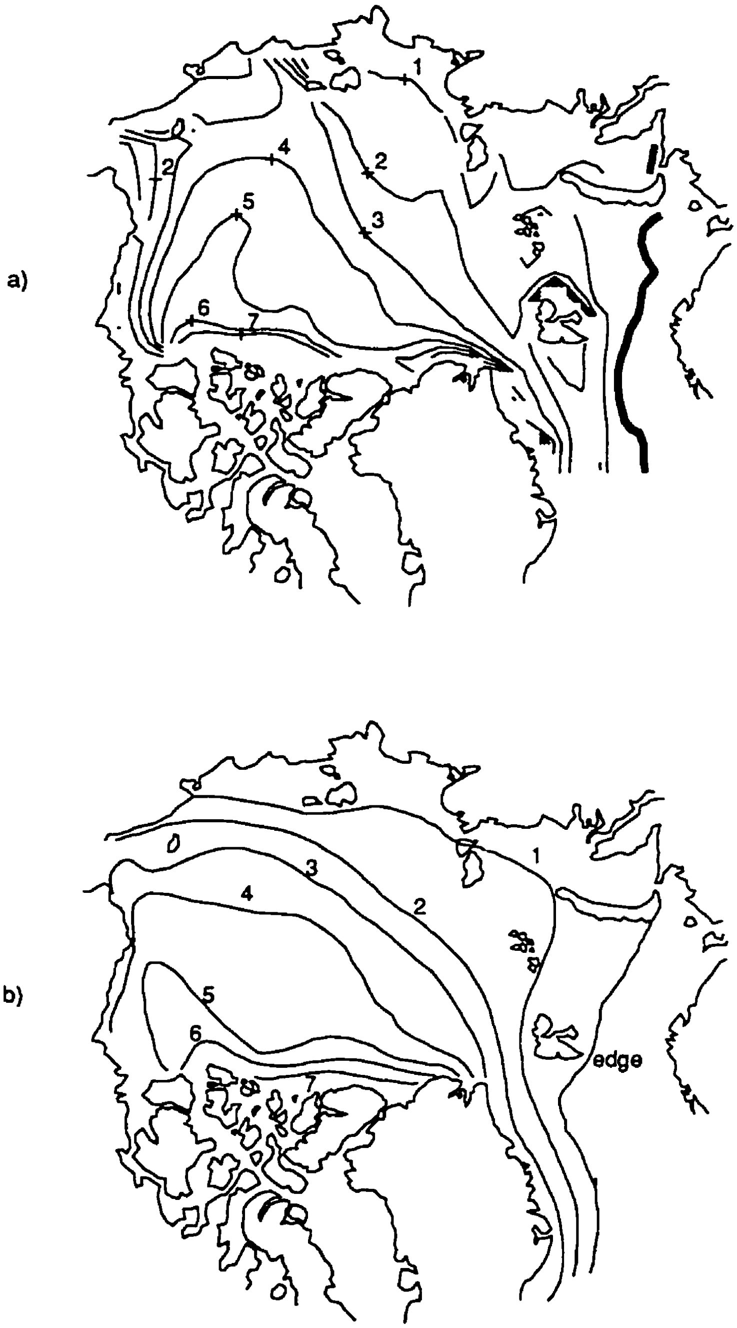

Figure 4.6: Simulated March ice thickness distribution in meters, (a), and observed ice thickness from sonar data (redrawn from Bourke and Garrett, 1987), (b). The heavy dark line denotes the ice edge.

The ice edge position, defined as the 5/10th ice concentration contour, is also included in these figures. Before discussing figure 4.6, it is useful to review the model results without ice dynamics. Runs with a thermodynamic-only model (not shown here) show thickness contours more or less concentric about the North Pole, with a bias of thicker ice towards the Canadian Arctic Islands, where the coldest temperatures are registered. Also, the heat transported by the North Atlantic Drift distorts the model thickness contours in the GIN (Greenland-Iceland-Norwegian) seas, keeping the Norwegian and a good part of the Barents Sea clear of ice. Finally, in a model without ice dynamics, the maximum ice thickness in the central Arctic is smaller than the observed values due to the absence of mechanically ridged ice. As can be seen upon comparing figures 4.6a and 4.6b, the inclusion of ice dynamics significantly improves the solution. The ice thickness contour patterns reproduce the observations well, including the double-humped distribution poleward of the northern Canadian islands, where there is a maximum ice thickness of 7 m. One-meter ice thicknesses are also present in the model near the Asian continent except in the Laptev and Siberian Sea where thicker than observed ice is present. The modelled ice free region in the North Atlantic now extends over the whole Norwegian and Barents Seas due to the prevailing wind blowing ice eastward. In the winter, whether the Bering Strait is open or closed has a strong influence on the ice thickness distribution in the Chukchi Sea. When open, the prescribed ocean velocity profile produces significantly thicker ice poleward of the Bering Strait. However, the temperature of the water entering the domain is very close to freezing point and does not have a significant influence on the growth of ice in this region.

In the Barents Sea, the ice margin is very well reproduced; however, in the Greenland Sea the ice edge is too far east. This is due to the nature of the prescribed ocean currents, which are characterized by a weak recirculation of water in the Greenland Sea. This discrepancy can also be seen by comparing the model and observed ocean temperature patterns (figure 4.7) where colder temperatures are generally present south of Svalbard, in the Greenland Sea. The generally well-positioned ice-edge in the model is remarkable, given that the atmospheric and ocean temperatures are calculated rather than prescribed. For the atmosphere, the model and observed temperatures for the month of March are shown on figure 4.8. The model air temperature in the central Arctic (figure 4.8a) is slightly too cold

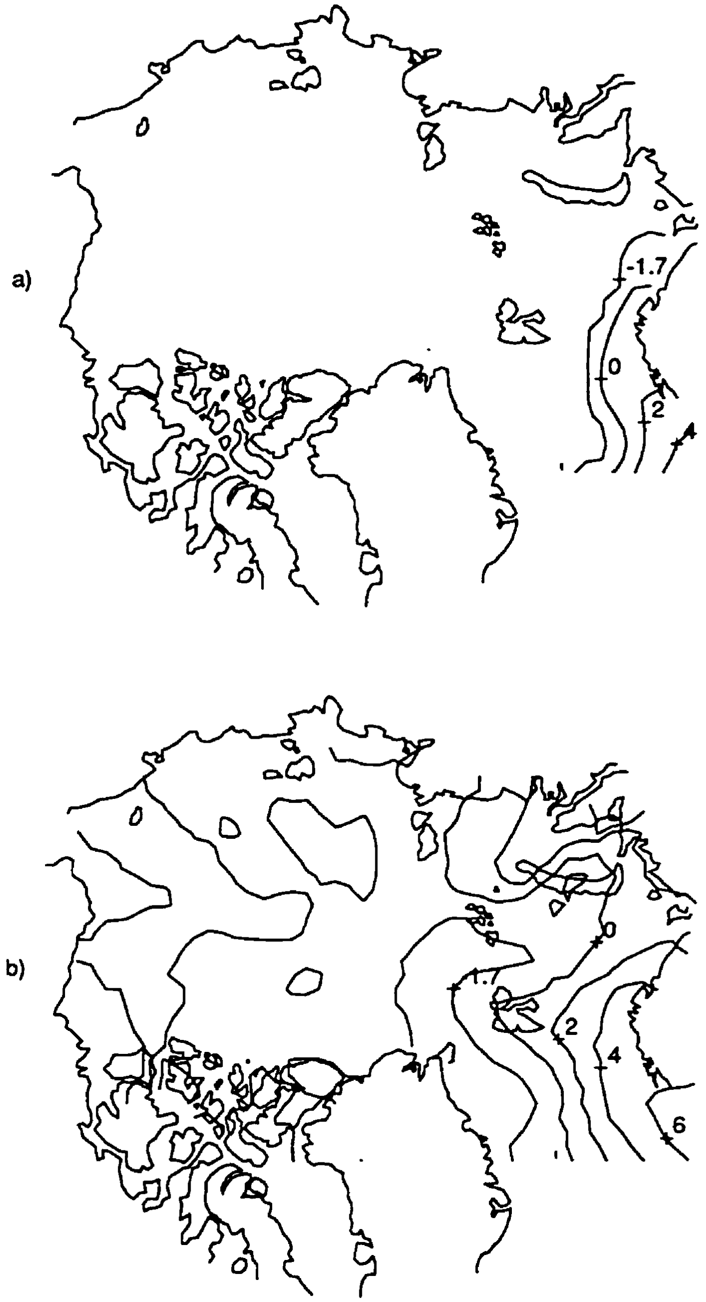

Figure 4.7: Simulated March ocean temperature distribution (Celsius), (a), and observed ocean temperature distribution from Levitus. (b).

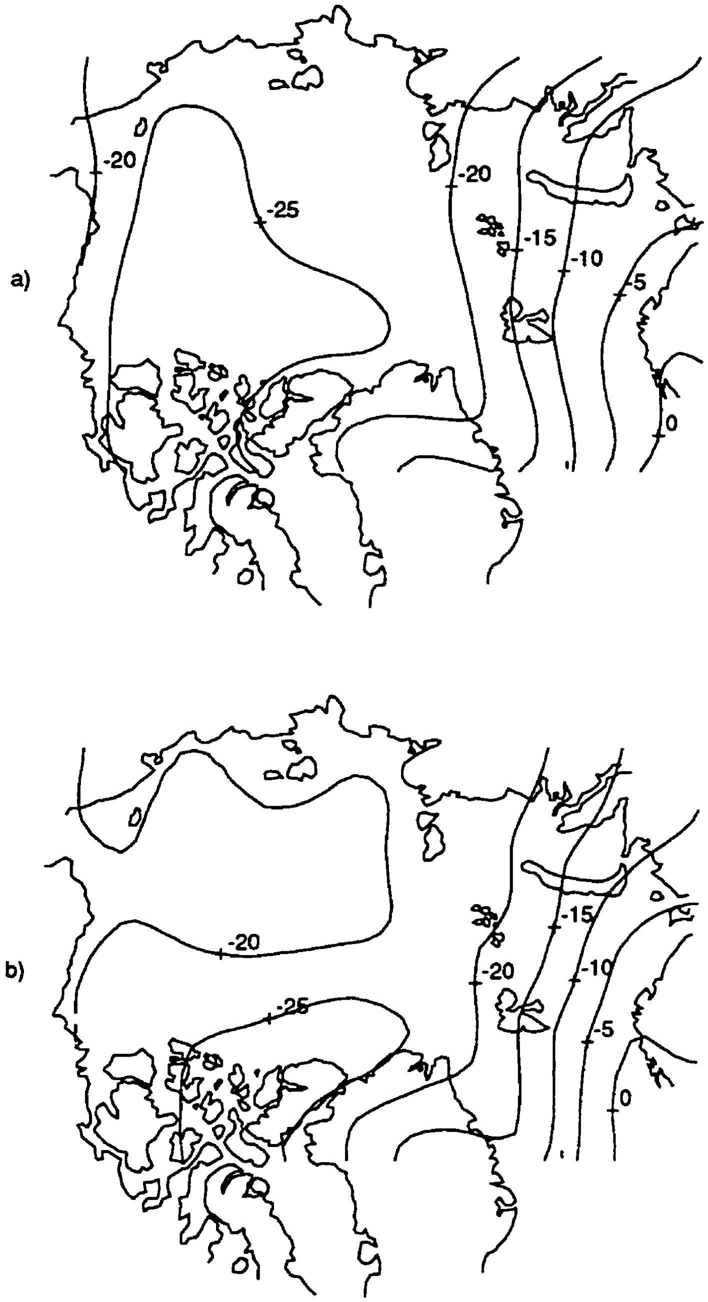

Figure 4.8: Simulated March atmosphere temperature distribution (Celsius), (a), and NMC derived atmosphere temperature distribution, (b).

due to the thicker ice present in the Laptev and East Siberian Seas. However, the model temperature contours are in very good agreement with the NMC analysis in the Barents, Norwegian and Greenland Sea where a tongue of warm water keeps the region ice free and the overlying air warm.

4.3 March ice thickness distribution with dilatation

A key quantity to be able to predict in climate studies at high latitudes is the heat lost by the ocean to the atmosphere. To obtain a good estimate of this quantity, both a realistic ice thickness distribution and a good representation of the lead distribution is necessary. Although the lead area represents a very small fraction of the total Arctic domain (typically 1 or 2 %), the amount of heat lost through the leads is of the same order of magnitude as the heat lost through the ice by conduction. Observations of the Arctic cover show that regions of open water are always present even in the central Arctic and far inside the ice margin. In some previous modelling studies, the ice concentration was capped at 99 % to account for this fact in an *ad hoc* manner. In this study a constant angle of dilatancy of 20 degrees is used, to account for the opening of leads along sliding lines. In reality, when a lead is formed, large heat loss from the ocean is present and thin ice reforms rapidly. This thin ice is very weak in compression and will ridge easily once it is subjected to compression. In this manner ice thickness can build up easily even in regions where thick multi-year ice is present. In this model, this is simulated by shear deformation with a small amount of divergence. This will cause the ice concentration to drop below 100 % and will result in an increased heat loss to the atmosphere. Finally, the reduction in ice concentration will result in a smaller ice strength in compression, which will make it easier to ridge. Figure 4.9 shows the mid-March ice thickness difference field with and without dilatation after a 2-month integration starting from the mid-January dilatation-free results. We observe that the ice thickness is larger in the high-shear region north of the Canadian Islands when dilatation is considered. After a 2-month integration, differences of 20 cm in ice thickness are obtained. The effect of dilatation will play a larger role poleward of the Canadian Islands, where observations show high lead activity, and in coastal regions where shear deformations are induced by the

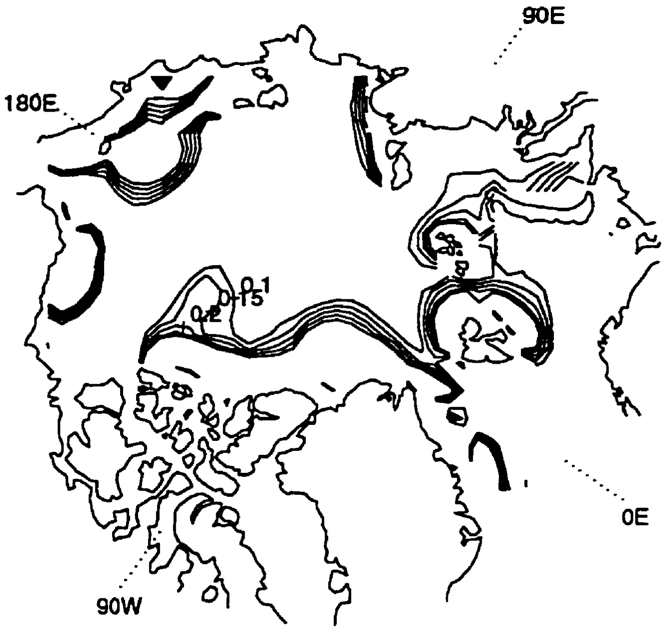

Figure 4.9: Ice thickness difference field with and without dilatation

presence of boundaries.

4.4 September ice thickness and concentration fields

Figures 4.10-a and 4.10b show the simulated and observed ice thickness distribution for the month of September. Again the ice edge is indicated in these figures. The calculated ice thicknesses are in reasonably good agreement with the measurements. However, the ice thickness peak is too far west, being north of the Canadian Archipelago instead of north of Greenland. The climatological wind pattern reverses in the summer (McLaren *et al.*, 1987) and is partly responsible for the observed shift; this seems to be under-represented in the model results. In the summer, the open boundary condition at the Bering Strait has an influence on the ice thickness distribution in the Chukchi Sea, both through the advection of warm waters from the North Pacific and the different ocean current pattern beneath the ice.

Simulated results from a thermodynamic only model (not shown here) show an ice edge position in the Barents Sea which is slightly too far south, and all of the Kara, Laptev and

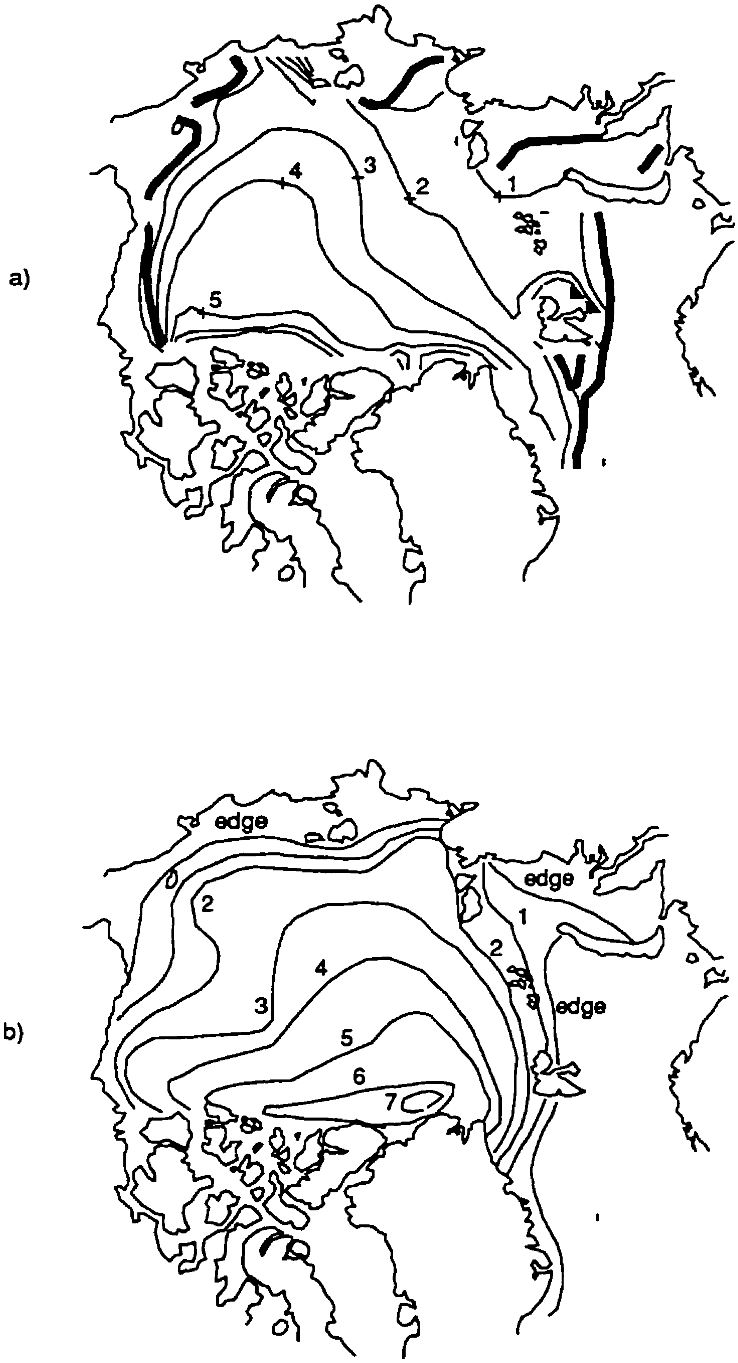

Figure 4.10: Simulated average September ice thickness field in meters, (a), and observed ice thickness (redrawn from Bourke and Garrett, 1987), (b). The heavy dark line denotes the ice edge.

East Siberian sea remain ice covered, unlike in the observations. The Beaufort and Chukchi seas are partly ice free but the ice edge is not well positioned. Including ice dynamics in the model yields a much improved modelled ice edge position. In the North Atlantic, much less ice accumulates in the winter due to the prevailing south-westerly winds present in the cold months. Consequently, the whole Barents Sea becomes ice free in the summer, as shown in figure 4.10a. Moreover, the Kara and Laptev seas are ice free, and the ice edge position at the edge of the Beaufort Sea agrees very well with observations. The position of this ice edge coincides with the demarcation line between first year and multi-year ice at the edge of the Beaufort Sea. As a result, the Beaufort Sea fills with first year ice in the winter, which melts away in the summer. Finally, the East Siberian Sea remains ice covered in the summer unlike in the observations. The details of the ocean current pattern are believed to play a large role in the position of the ice edge in this area.

Chapter 5

The origin and evolution of sea-ice anomalies in the Beaufort Sea

5.1 Introduction

Large interannual and decadal-scale variability exists in the Arctic sea-ice areal extent, especially in the summer, when large parts of the peripheral seas are relatively free of ice. This results in very different positioning of the ice margin from one year to the next. In the following sections, these variations, or ice cover anomalies[1], are described and modelled.

In a study of interdecadal climate variability in the Arctic, it has been hypothesized (Mysak *et al.*, 1990) that the ice anomalies originating in the Beaufort Sea travel out of the Arctic into the Greenland Sea via the Beaufort Gyre and the Transpolar Drift Stream. This hypothesis was further explored in Mysak and Power (1992) who showed from a cross-correlation analysis that Beaufort Sea ice concentration anomalies propagated into the Greenland Sea in about 2 to 3 years. This process would contribute to variations in the transport of sea ice (fresh water) into the Greenland Sea and could potentially affect the local ocean circulation. The input of fresh water into the Greenland Sea is accomplished mainly by ice export and the advection of low saline surface waters from the Arctic, with the advection of sea ice being the dominant process (Aagaard and Carmack, 1989). At these latitudes,

---

[1] The difference between the sea-ice cover for a given month in a particular year and the climatological value for that month.

the stratification of the ocean is mainly determined by the vertical salinity structure and is only slightly influenced by changes in temperature. In fact, close to the ocean freezing point, large temperature changes (eg. due to cooling) can be offset by very small inputs of fresh water.

In the North Atlantic, deep convection occurs in the Greenland Sea and in the Labrador Sea, and the input of substantial amounts of fresh water from the Arctic could thus possibly stabilize the water column and suppress or reduce convection. This in turn could reduce deep water formation in the northwest North Atlantic and consequently decrease the poleward heat transport via the thermohaline circulation (Broecker *et al.*, 1985). Hence, sea-ice conditions in the peripheral seas and variations in sea-ice export from the Arctic are important factors to consider in climate studies of high latitude regions. In the Beaufort Sea, the sea-ice conditions are also important for oil and gas industries operating in this region. Thick ice moving towards the shore can cause scouring of the ocean bed, a potential hazard for buried pipelines; extensive ice cover is also a hazard for shipping in the Beaufort, Chukchi and Bering Seas. Finally, propagation of these anomalies around the Beaufort Gyre could potentially be of importance for navigation in the Arctic in general (Mulherin, 1996).

Over two decades ago, the anomalous ice export into the Greenland Sea was explained by the forcing from local wind anomalies (Dickson *et al.*, 1975). More recently, the importance of large scale wind anomalies over the central Arctic in generating ice anomalies was recognized (Walsh and Chapman, 1990). Simulation results from a coupled sea ice-ocean model (Häkkinen, 1993) show that a large part of the fluctuations in ice export out of the Arctic can be explained by regional and large scale anomalous wind patterns, which supports the latter hypothesis. Other sources of fluctuations in the fresh water budget for the Greenland Sea include the variation of surface Arctic Ocean salinity caused by fluctuations in the river runoff into the Arctic (Mysak *et al.*, 1990) and the input of relatively fresher water through Bering Strait (Goose *et al.*, 1996).

A number of studies have set out to identify the main factors responsible for the presence of ice anomalies in the Beaufort Sea. From a cross-correlation analysis, Manak and Mysak (1989) found that ice anomalies in the Beaufort Sea could be linked to fluctuations of fresh water input from Mackenzie River runoff. Such runoff, it was argued, would raise the freezing point of ocean water and thus increase ice growth during the cold season. Recent simulation results from a coupled sea ice-ocean model reported by Weatherly and Walsh (1996), however, showed that the doubling of Arctic river runoff has little effect on sea-ice formation. These results are open to debate, though, because of the relatively coarse resolution in the model which does not allow an accurate representation of river runoff-sea ice interactions.

The effect of high latitude warming due to a doubling of atmospheric CO_2 concentration on ice conditions in the Beaufort Sea and the possible impact on the oil and gas industry operating in this region were studied by McGillivray et al. (1992). Using an atmosphere general circulation model coupled to a simple slab ocean and a thermodynamic sea ice model, they showed that warmer air temperatures significantly influence sea ice conditions in the Beaufort Sea. Thermodynamic-only sea ice models, however, are usually more sensitive to changes in atmospheric forcing than thermodynamic-dynamic sea ice models. Manak and Mysak (1989) also showed a significant correlation between the 25-month running mean atmospheric temperature and the extent of the sea ice cover in the Beaufort-Chukchi Seas, Hudson Bay and Baffin Bay.

Rogers (1977) found that the ice anomalies in the Beaufort Sea were correlated with anomalous atmospheric temperature and wind patterns, with wind forcing being the dominant factor. Chouinard et al. (1995) studied the relation between Beaufort Sea ice anomalies and sea surface temperature, anomalous wind patterns and discharge from the Mackenzie River using empirical orthogonal analysis (EOF). The data used come from Beaufort Sea ice charts produced by the Atmospheric Environment Service of Canada. The first sea-ice EOF (explaining 45 % of the total variance), showing a north south displacement of the ice edge, was interpreted to be due to anomalous air temperature conditions, whereas the second (explaining 35 % of the total variance), showing an east-west structure, was believed to be due to anomalous ice conditions produced by winds. The third and fourth components, showing an ice anomaly shaped like a river plume at the mouth of the Mackenzie delta, account for less than 10 % of the total variance and is believed to be associated with river runoff.

In this chapter, we use data and the sea-ice model developed earlier to determine the relative importance of anomalous ocean surface salinities, atmospheric temperatures and winds, in creating ice anomalies in the Beaufort Sea region. Since the model described in chapter 2 does not include a fresh water budget, the possible influence of river runoff on ice anomalies will be estimated from simple calculations and relevant observations. The influence of temperature and wind anomalies is assessed from large scale temperature and wind stress data together with a simulation of the Arctic sea ice cover for the year 1965, when one of the largest positive ice anomalies was observed in the Beaufort Sea. The sea-ice model is also used to track a Beaufort Sea ice anomaly around the Beaufort Gyre and determine whether it can survive a few seasonal cycles and still cause a significant fluctuation in ice export to the Greenland Sea. Section 5.2 presents various mechanisms that could lead to the formation of ice anomalies in the Beaufort Sea. In section 5.3, the space-time evolution of an ice anomaly in the Beaufort Sea is described. The main conclusions drawn from this study are summarized in chapter 7.

5.2 Origin of ice anomalies in the Beaufort Sea

During a given year, the surface area covered by sea ice in the Beaufort Sea can differ substantially from climatology. In this region, one of the largest ice anomalies, inferred from satellite measurements made over the second half of this century, was present in 1965. The reported positive ice anomaly signal in the Beaufort and Chukchi seas together was 150×10^3 km^2 (Mysak and Power (1992); sea also figure 5.2 below), which was approximately 25 % of the total climatological uncovered area. For an ice thickness of 1 m, typical for first year ice in the Beaufort Sea, this corresponds to an ice volume anomaly of 150 km^3. However, for the ice thickness representative of thick multi-year ice, the volume anomaly could be much larger.

Sea ice thickness can vary because of both thermodynamic and dynamic processes, as indicated by the sea ice continuity equation 2.4. To better understand the influence of these two factors on the growth of sea ice, the time scale associated with each of these processes is determined. Since we are interested in sea-ice anomalies, we analyze the linearized continuity equation for the perturbation fields (see equation 2.4 as a reference):

$$\frac{\partial h'}{\partial t} + \nabla \cdot (\boldsymbol{u}'_i \overline{h} + \overline{\boldsymbol{u}}_i h') = S'_h,$$

where the primed quantities are the perturbations and the overbarred quantities are the mean values.

To estimate the time scale involved in the growth of ice perturbations due to thermodynamic processes, we assume the first term is in balance with the forcing term. This yields

$$[t]_{temp} = \frac{[H']}{[S'_h]} = \frac{1 \text{ m}}{0.1 \text{ cm/day}} \approx 3 \text{ years},$$

assuming the ice anomalies are typically 1 m thick and that the ice growth anomaly is 0.1 cm/day (Maykut and Untersteiner, 1971). Similarly, the time scale for an ice anomaly to be produced by dynamical process (anomalous winds) can be found by balancing the second term with the first term, in which $\boldsymbol{u}'_i$ would represent an anomalous ice drift speed due to wind anomalies. This gives

$$[t]_{wind} = \frac{[L][H']}{[U][H]} = \frac{300 \text{ km}}{5 \text{ cm/s}} \approx 2 \text{ months},$$

where $[L]$ is the Beaufort Sea half width, [U] is a typical ice drift speed anomaly (5 cm/sec) and the anomalous $[H']$ and mean [H] ice thicknesses in the Beaufort Sea are assumed to be comparable (1 m). From the above estimates it appears that wind anomalies will contribute more rapidly to interannual variability of the sea ice cover than atmospheric temperature anomalies.

The time scale for salinity changes associated with river runoff is more difficult to estimate since it has an effect on both ocean stratification and ocean surface salinity. This is discussed in detail in the next section.

5.2.1 Salinity hypothesis

To estimate the effect of reduced sea surface salinity on ice formation in the fall, two situations are considered: first, a reference ocean with climatological sea surface salinity ($\overline{S}$), and second, a perturbed ocean with reduced sea surface salinity (S') due to increased river runoff. The initial temperature of the ocean mixed layer in the fall is considered to be $T_0 = 0°$ C.

A reduction of sea surface salinity results not only in a higher freezing point temperature (Manak and Mysak, 1989), but also in a stronger upper ocean stratification. These two factors contribute to an enhanced ice formation in the fall. In the following, we present a first order calculation to quantify the combined effect of these two factors.

In the reference case, the total heat released by the mixed layer to reach its freezing point temperature is equal to $\rho_w A_{BS} H_{ml} C_{pw}[T_0 - T_{fp}(\overline{S})]$, where ρ_w is the density of water, A_{BS} the Beaufort Sea surface area (300 × 10^3 km^2), H_{ml} the reference case mixed layer depth (20m), C_{pw} the specific heat of water (4 KJ/Kg K) and $T_{fp}(\overline{S})$ the freezing point of water with salinity $\overline{S}$ (-1.8 C° and 31 ppt). To provide an upper bound on the ice anomaly estimate, we assume the fresher ocean has lost the same amount of heat to the atmosphere at that time (i.e. the insulating effect of ice is ignored). This heat lost is made of two components, the heat required to cool the ocean mixed layer from 0° C to its freezing point temperature, and the latent heat released during ice formation. Thus, the thickness of the ice anomaly can be calculated as follows:

$$\rho_w A_{BS} H_{ml} C_{pw}[T_0 - T_{fp}(\overline{S})] \quad = \quad \rho_w A_{BS} h_{ml} C_{pw}[T_0 - T_{fp}(S')] + \rho_i A_{BS} L_f h_{ia},$$

which yields

$$h_{ia} \quad = \quad \frac{\rho_w C_{pw}}{\rho_i L_f}\left\{H_{ml}[T_0 - T_{fp}(\overline{S})] - h_{ml}[T_0 - T_{fp}(S')]\right\}, \tag{5.1}$$

where h_{ml} is the fresher ocean-mixed layer depth, ρ_i the density of ice, L_f the latent heat of fusion of water and h_{ia} the ice anomaly formed due to the freshening of the surface layer. It remains to estimate the modified mixed layer depth (h_{ml}) and sea surface salinity (S') resulting from an abnormally high river runoff (see appendix C). Both of these will strongly depend on the amount of horizontal and vertical mixing taking place during the summer months.

The amount of horizontal mixing is assessed from the ocean surface salinity (Levitus, 1994) for the months of May and September respectively (see figure 5.1a-b). In the spring, the high river runoff produces a tongue of fresh water extending from the Mackenzie River mouth to the edge of the Beaufort Sea; in the fall, this fresh water signal is advected westward and much mixing occurrs, resulting in surface salinities varying between 25 to

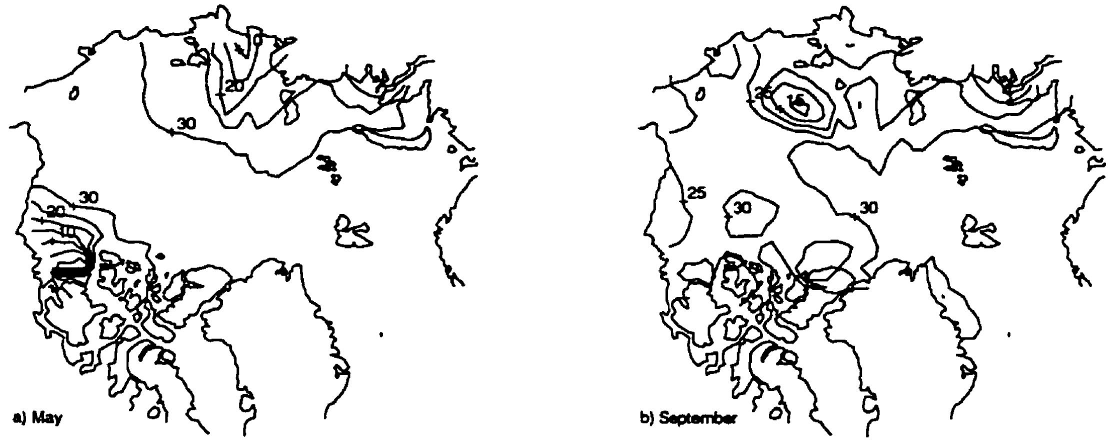

Figure 5.1: Climatological ocean surface salinity field for the month of May, (a), and September, (b) (from Levitus data (1994)).

30 ppt. Accordingly, we assume that both river runoff and melted sea ice are well mixed horizontally in the ocean surface layer. On average, the annual river runoff (300 km^3) and melting of sea ice (300×10^3 km^2 $\times$ 1 m) contribute equally to the input of fresh water into the Beaufort Sea. It is assumed that mixing of this fresh water with the saltier ocean water due to the winds, tides and waves produces a 20 m deep mixed layer (H_{ml}) and a 3.1 ppt salinity difference between the surface and the deep water (see figure C.2). Assuming the same amount of energy input into the fresher ocean mixed layer due to mixing, a 50 km^3 river runoff anomaly (8 % anomaly in fresh water input), as observed in the 1965, will produce a 1.2 m reduction in mixed layer depth (equation C.2) and a 0.48 ppt reduction in mixed layer salinity (equation C.1). Detailed calculations for these numbers are presented in appendix C. Considering a linear dependence of the ocean freezing point temperature on salinity, this reduction in sea surface salinity results in a 0.028° C increase in freezing point temperature ($T_{fp}(S')$) relative to the reference case ($T_{fp}(\overline{S})$).

Upon substituting these values into equation 5.1, we obtain an ice anomaly of 3.7 cm. For typical winter conditions, 3.7 cm thick ice can be formed in a day. Integrated over the whole summer, an ice anomaly of 3.7 cm with a persistence of 1 day does not constitute a significant contribution in the calculation of summer sea ice anomalies. It would, on the other hand lead to a slightly thicker winter ice cover preventing complete melting the following summer[2]. However, a 3.7 cm ice thickness anomaly only constitutes a 4 % increase over the mean Beaufort Sea ice thickness in winter (1 m) and is considered of second order importance in explaining interannual variability in this region. This agrees with the conclusion drawn from an EOF analysis of Beaufort Sea ice data (Chouinard and Garrigues, 1995), where the third and fourth modes (believed to be related to the discharge of the Mackenzie River), explains less than 10 % of the total variance. Also, the influence of reduced fresh water input into the Arctic seems to be more important than an increased input (see appendix C). Its influence on the freezing point temperature of the ocean water is negligible compared with its influence on the stratification of the upper ocean, a necessary condition to have significant ice formation in the deep ocean (Aagaard and Carmack, 1989). The fluctuations in the input of fresh water over longer time scales (> 10 years), however, could have a substantial influence on the Arctic stratification and consequently on the average thickness of the ice cover.

5.2.2 Atmospheric temperature and wind stress hypotheses

The possible influence of atmospheric temperature and wind stress anomalies on the formation of sea ice anomalies in the Beaufort Sea is now examined. In principle, colder years result in thicker ice which prevents complete melting in the next summer, while anomalous wind patterns can advect ice southward or northward, resulting in a very different ice edge position the next summer. The anomalous years used in this study are chosen based on an ice concentration anomaly time series shown in figure 5.2. An approximately 10-year oscillation is seen as the dominant signal in this figure (see also Mysak and Power (1992)) although secondary peaks are seen in between the higher peaks. These peaks also correlate with the peaks in the Mackenzie river runoff, as shown in Bjornsson et al. (1995).

To quantify the relative importance of atmospheric temperature and wind stress anomalies in creating ice anomalies, the sea ice model is run from October 1964 to September 1965 (see figure 5.2) and the ice anomaly field at the end of the integration is calculated. The initial conditions used for this run are the ice drift speed, thickness and concentration for the

---

[2] The maximum correlation between river runoff and sea ice extent is found at a lag of 1 year (Manak and Mysak, 1989; Chouinard and Garrigues, 1995)

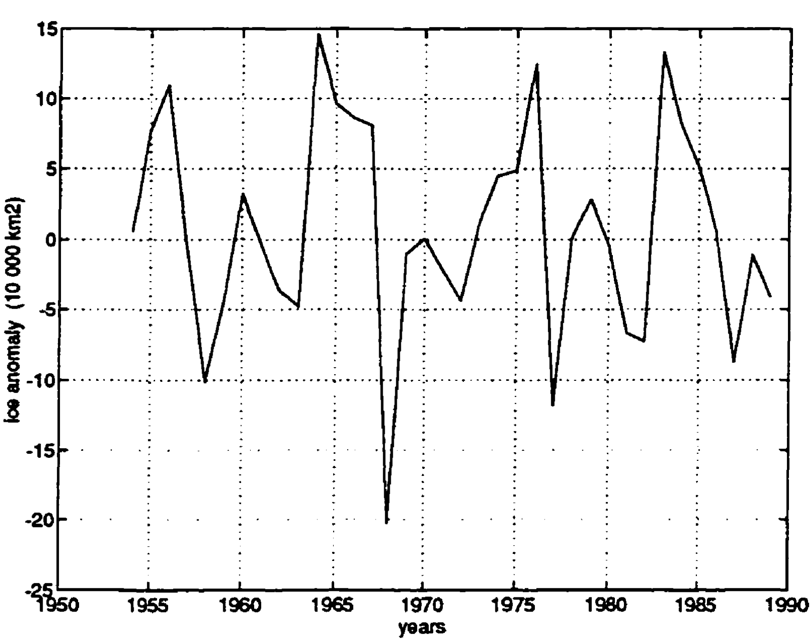

Figure 5.2: Summer sea-ice anomaly time series for the Beaufort Sea (data from Walsh and Chapman (1995), personal communication).

September climatology. The model is run for 1 year in the uncoupled mode, first with the climatological atmospheric temperature field and the anomalous wind stress prescribed, and then with the prescribed anomalous temperature field and the climatological wind pattern. In this manner, that part of the ice anomaly explained by the temperature anomaly can be differentiated from that part explained by the anomalous wind-driven transport of ice in the Beaufort Sea.

Figure 5.3 shows the observed summer sea ice edge position from the data compiled by John Walsh (University of Illinois) for the climatology, (a), and the year 1965, (c). In this figure, the dividing line (ice edge) between ice and no-ice was set at 75 % ice concentration in order to increase the contrast between the anomalous year and the climatology. On the same figure, the simulated summer ice margin using climatological wind stresses and air temperatures (b), 1965 wind stresses and climatological air temperatures (d) and climatological wind stresses and 1965 air temperatures (e) are presented. The results for the climatology (figure 5.3b) show that the simulated ice edge position in the Beaufort-Chukchi Seas is in excellent agreement with the observations. This gives us confidence in the model's ability

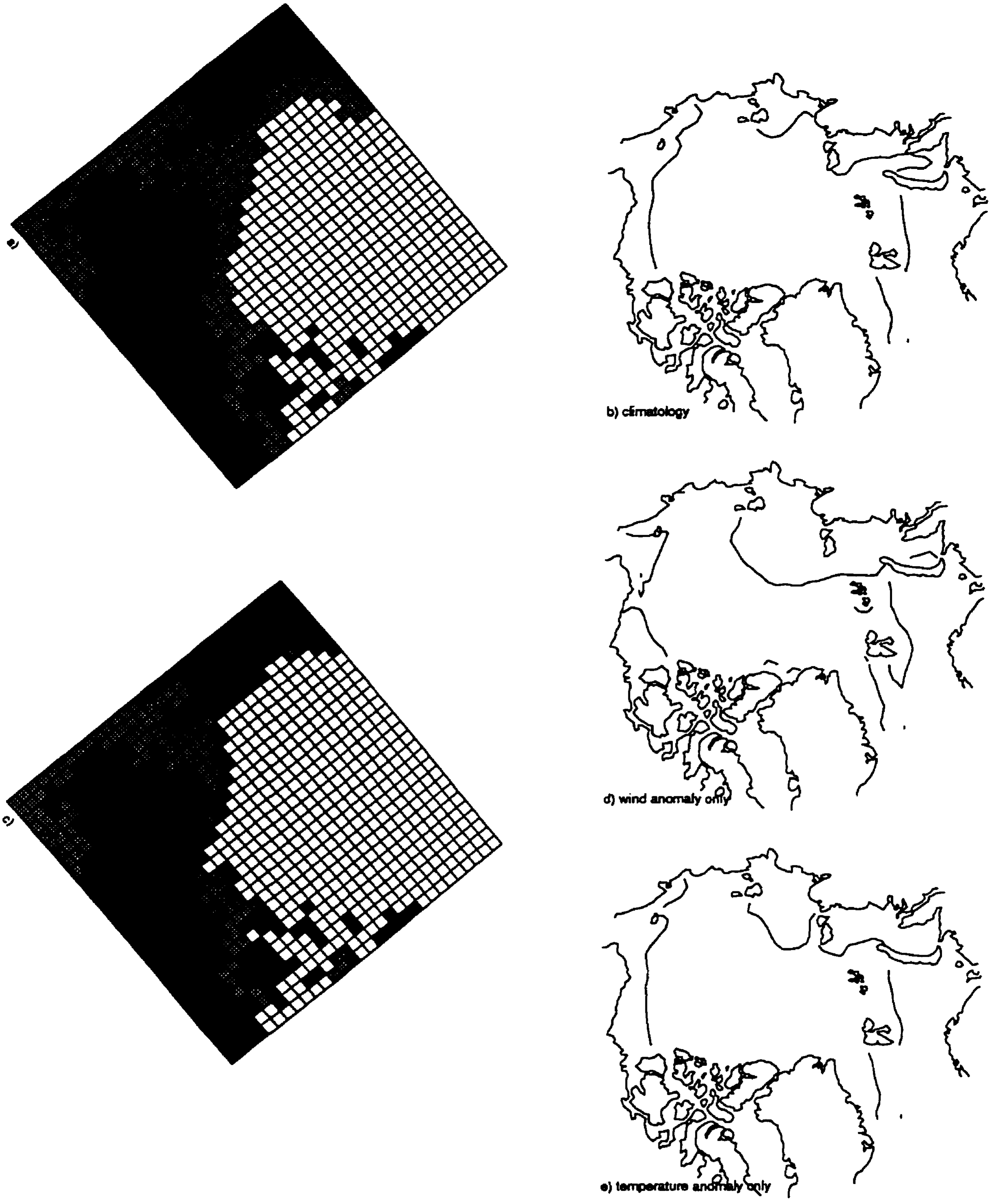

Figure 5.3: Observed (a,c) and simulated (b,d,e) ice edge position for the climatology (a,b) and the year 1965 (c,d and e). In (d), the model is forced with 1965 wind stress and climatological atmospheric temperature and in (e) the model is forced with climatological wind stress and 1965 atmospheric temperature. To increase the contrast between climatology and the anomalous year, the ice edge position is defined as 75 % ice concentration

to reproduced observed sea ice condition for a particular year. In figure 5.3-d, where the model is forced with prescribed climatological monthly mean temperature and 1965 wind stresses, the observed ice margin is well reproduced by the model, with anomalous ice conditions in both the western Beaufort and Chukchi Seas. On the other hand, the results using prescribed climatological monthly mean wind stresses and 1965 temperature field resembles the climatology runs 5.3-e; this indicates that anomalous winds are mainly responsible for the formation of the 1965 anomalous ice conditions and that the atmospheric temperature anomalies only played a minor role. The results using both 1965 wind stresses and air temperatures (not shown here) are very similar to the the one in figure 5.3-d.

To verify that these conclusions are applicable to other years where anomalous Beaufort Sea ice conditions were present, eight events of abnormally high ice concentration or abnormally low ice concentrations (including 1965) are studied in more details (1956-high, 1958-low, 1964-high, 1968-low, 1976-high, 1977-low, 1983-high and 1987-low). The wind stress anomaly fields for those eight years are shown in figure 5.4a-h. The wind stress fields are constructed from the spring (April-June) and summer (July-September) months; the fall and winter values are not considered since we focus on summer ice anomalies and the time scale associated with sea ice advection is about 2 months (see section 5.2). In previous studies, the influence of winds on ice conditions was assessed using the mean sea level pressure anomaly fields ($\propto |\overline{u}_a^2|$) rather than the mean wind stress ($\propto |\overline{u_a^2}|$) anomaly fields. These two fields can be significantly different, especially in the summer, when large wind events are usually associated with the passage of cyclones.

The results show that years with positive ice anomalies are generally associated with anomalous northerly or westerly wind stresses which tend to push ice into the Beaufort Sea while years with negative ice anomalies are generally associated with anomalous southerlies or easterlies carrying ice away from the Beaufort Sea. Note that the ice drift direction is to the right of the wind stress vector. The year 1987 stands as an exception, but the anomalous ice conditions that year were not as severe (see figure 5.2). Also, the anomalous air temperature fields (not shown here) show no distinct pattern between yearly averaged air temperature and anomalous ice conditions. These results support the conclusions from the detailed 1965 sea ice simulations.

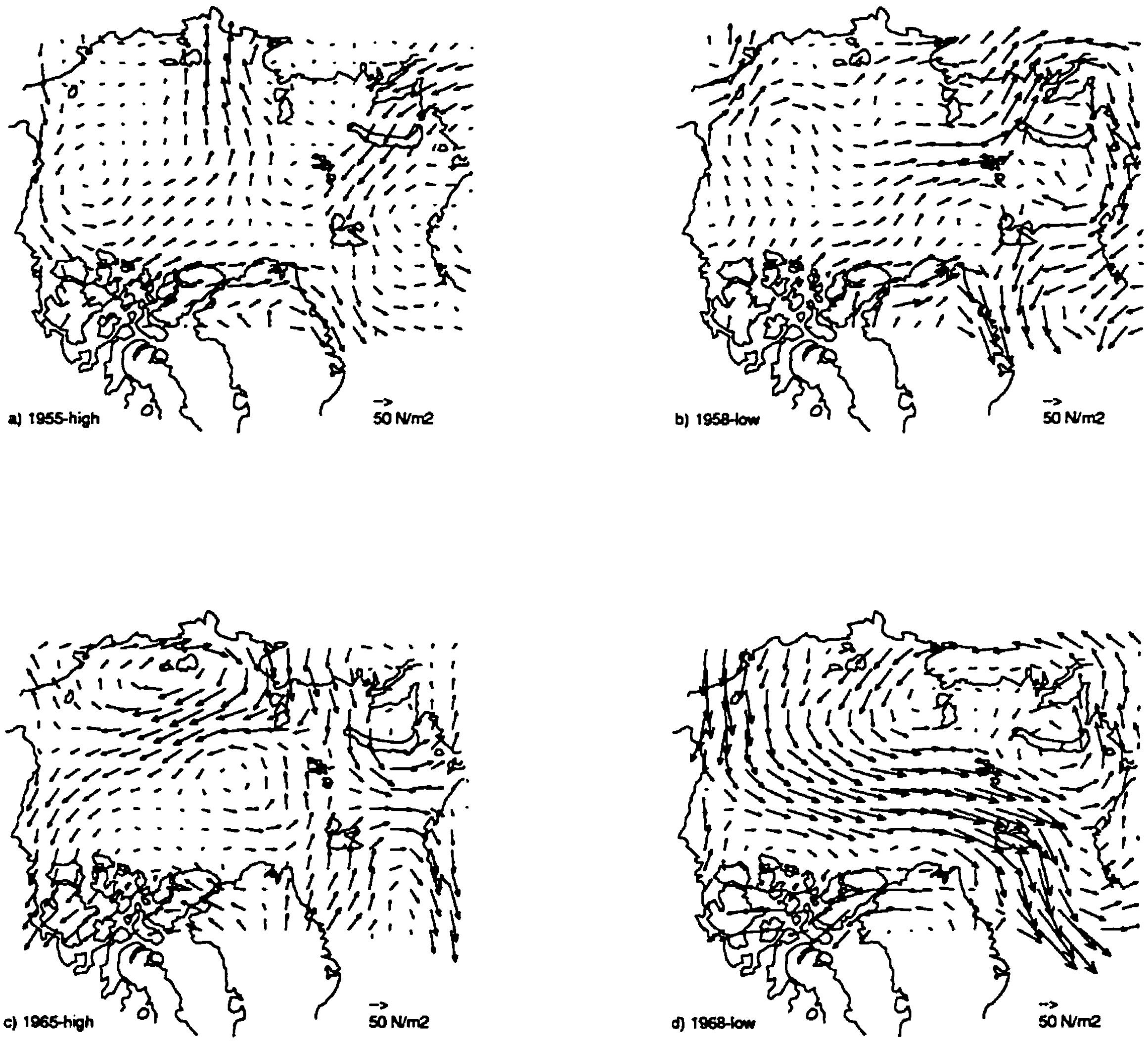

a) 1955-high

b) 1958-low

c) 1965-high

d) 1968-low

Figure 5.4: Wind stress anomalies (spring-summer) for the years 1955 (a), 1958 (b), 1965 (c), 1968 (d), 1976 (e), 1977 (f), 1983 (g) and 1987 (h). The climatological wind stresses were calculated from those 8 years.

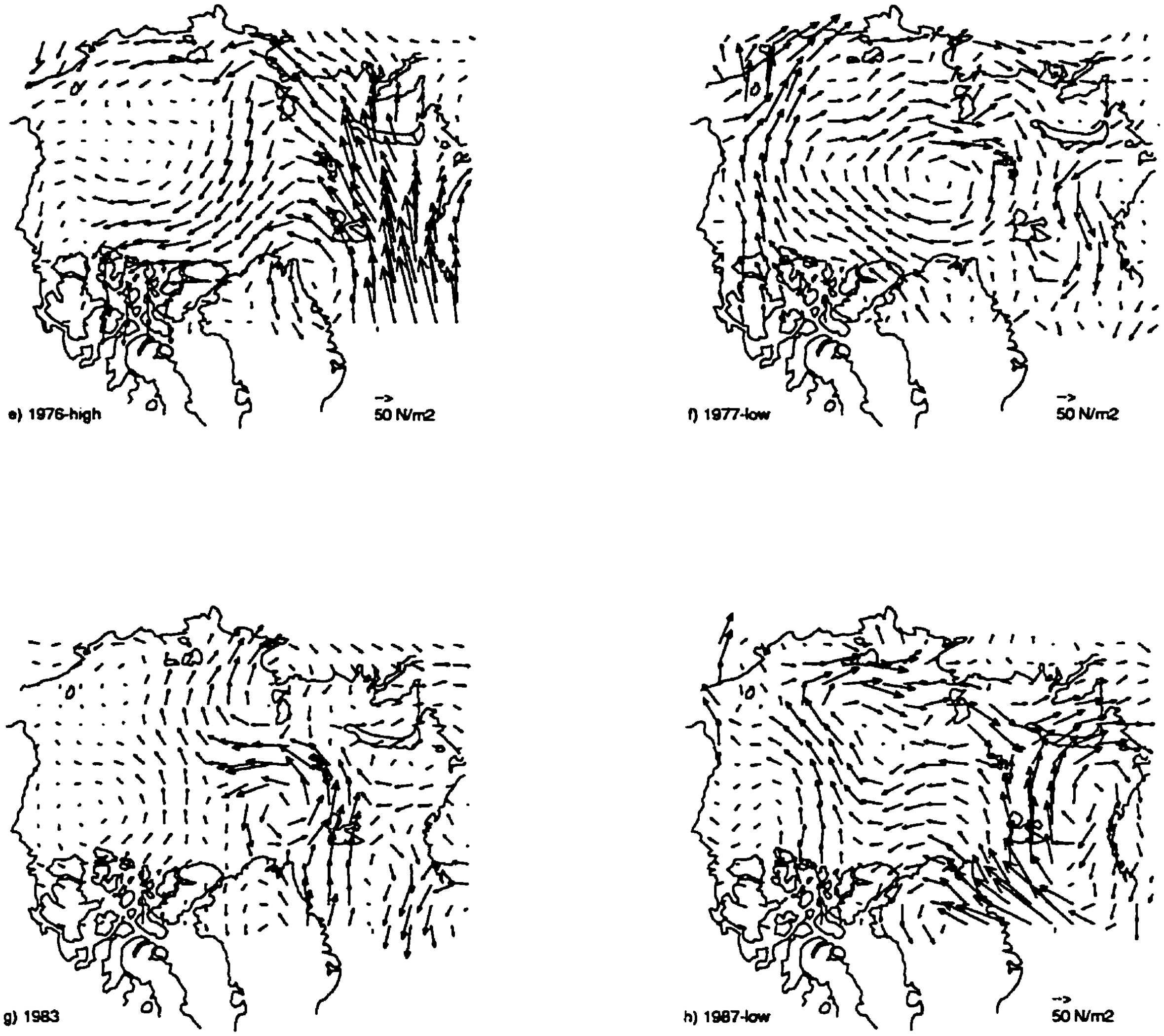

Figure 5.4: Continued

These conclusions are also in accord with the results of Rogers (1977) who showed that ice concentration had a large correlation coefficient with local winds and a smaller correlation with temperature. On longer time scales (2-3 years), however, it has been shown that the atmospheric temperature and ice anomalies are significantly correlated (Manak and Mysak, 1989; Rogers, 1977).

5.3 Evolution of Beaufort Sea ice anomalies

In the previous section, it is argued that the ice concentration anomalies observed in the western Beaufort and Chukchi seas in 1965 are mainly due to anomalous winds advecting ice into those region. Since the ice advected towards these seas would also include multi-year ice, the anomaly near the coast would show up for both sea ice concentration and thickness data. Below, we examine the evolution in time of the Beaufort Sea ice anomaly observed in 1965 as it is advected around the Beaufort Gyre. At first, the model is run for a period of 3 years starting in October 1965 with an ice anomaly of 2 m in mean thickness and 20 % in ice concentration as the initial conditions (see figures 5.5a and 5.3c), and with 1965 wind stress and atmospheric temperature forcing fields. In a second calculation, the model is run with the same forcing but with the September climatological ice thickness and concentration field as the initial conditions. The anomaly signal is constructed by subtracting the output from the two runs at a given time.

Figure 5.5 shows the difference ice thickness fields between the two runs at time intervals of 6 months. The ice anomaly is advected anti-cyclonically around the Beaufort Gyre and is still apparent 2.5 years later (1968) in the Fram Strait region. Similar conclusions were drawn by Mysak and Power (1992) who traced ice **concentration** anomalies around the Beaufort Gyre and Transpolar Drift Stream. In the peripheral seas, the ice anomaly signal decreases in amplitude as it is in contact with warmer waters from the ice free area; in the central Arctic, summer melting is more important than winter ice growth for thicker ice, which leads to a further reduction in the amplitude of the signal. From the Beaufort Sea to the Fram Strait, the ice anomaly has decreased from 2 m to approximately 20 cm. Considering a mean ice thickness of 2 m in the Fram Strait region, this can account for a 10

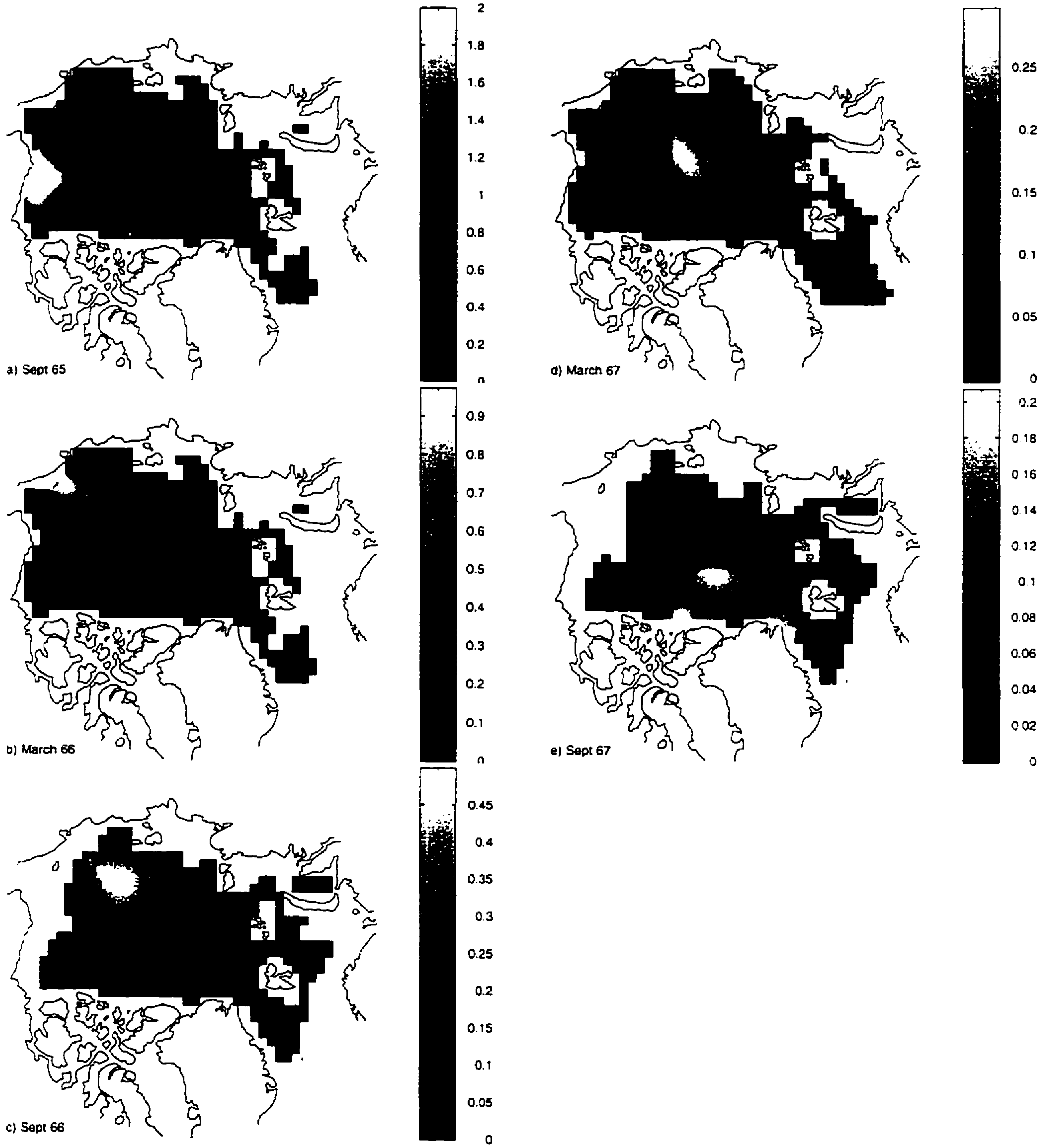

Figure 5.5: Sea ice thickness difference fields starting in October 1965. The time interval between two figures is 6 months. Scales are in meters: note that each colorbar has a different scale.

% ice volume anomaly. In 1968, an ice concentration anomaly of 300 000 km^2, attributed to local and large scale wind anomalies in the high Arctic, constituted a 25 % increase in the ice export over the climatological value. According to the simulation results, the export of Beaufort Sea ice anomalies out of the Arctic contributes a smaller (10% compared to 25%) but significant amount to the fluctuation in fresh water input to the Greenland Sea.

Chapter 6

Driftwood experiment

6.1 Introduction

It has been proposed by Dyke et al. (1997) that by analyzing driftwood collected on the raised beaches of the Canadian Arctic Archipelago, it may be possible to infer the mean ice drift and upper ocean circulation patterns over century time scales in the Arctic Ocean during the Holocene epoch. Driftwood enters the Arctic Ocean from the bank erosion of the major North American (NA) and Eurasian rivers, is transported away from its sources by sea ice, and eventually strands on the coastlines of Svalbard, Greenland, Iceland, Alaska or the Canadian Arctic Archipelago (CAA). Therefore, changes in the amount and type of driftwood stranding in one region through time, could be interpreted as a change in wood delivery route and hence a change in sea ice drift pattern.

The pattern of annual mean sea ice drift in the Arctic Ocean comprises two distinct features, namely, the anticyclonic Beaufort Gyre in the Canada Basin and the Transpolar Drift Stream (TDS) in the central Arctic, extending from the Siberian coast to Fram Strait. The present source regions for ice exported from the Arctic Ocean to the Greenland Sea include the Chukchi, East Siberian, Laptev, Kara and Barent Seas. Ice formed in the Beaufort Sea can either leave the Arctic via the Beaufort Gyre and the Transpolar Drift Stream or recirculate for many years as part the Beaufort Gyre. The peripheral seas mentioned above have a relatively thin ice cover ($\approx$ 1m) and are partly ice free in the summer season, whereas

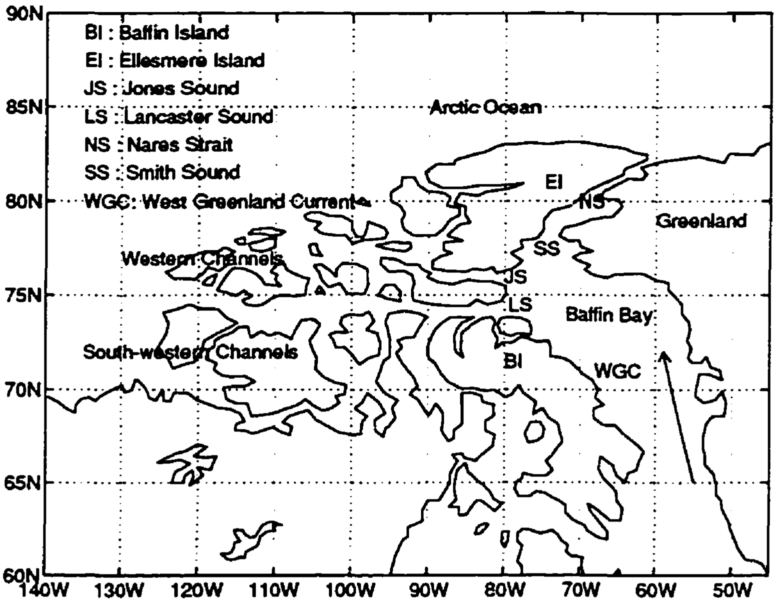

Figure 6.1: Map of the Canadian Arctic Archipelago (CAA).

ice caught in the Beaufort Gyre can remain there for several years before leaving the Arctic basin and can have thicknesses of several meters (Bourke and Garrett, 1987).

Driftwood samples of various ages from the Holocene collected in the CAA show three distinct modes of wood delivery to this region (Dyke *et al.*, 1997): a first mode, where driftwood of North American and Eurasian origin is found in regions of the CAA only accessible by sea ice entering from the north and northwest of the CAA (see figure 6.1); a second mode, where driftwood of North American origin is found on the shores around the head of Baffin Bay, a region mainly accessible via the East and West Greenland currents, and also where driftwood of Eurasian origin is found in Svalbard; finally, a third mode, where North American driftwood is found in the central and north part of the CAA and Eurasian driftwood is found on the Baffin Bay coastlines and in Svalbard. Dyke et al. hypothesized that eastward and westward shifts in the TDS could be responsible for the observed variation in the type and amounts of wood delivered through time in the various regions. Thus they argued that there was a westward shift in the TDS which helped produce an extended Beaufort Gyre for mode one, an eastward shift in the TDS together with a reduced Beaufort Gyre for mode two, and a split TDS for mode three which is believed to have been in existence for the past few hundred years.

In the next section, descriptions of the driftwood data and delivery routes are presented (further details can be found in Dyke et al. (1997)). In section 6.3, simulation results from the sea-ice model described in chapter 2 are presented for different atmospheric forcings in an attempt to assess the hypothesis of postglacial oscillations of the TDS (Dyke *et al.*, 1997). From these simulations, we can infer something about the nature of century and millenial scale changes in Arctic atmospheric circulation. The main conclusions are summarized in chapter 7.

6.2 Data description and incursion history

A total of 299 driftwood samples from raised beaches of the CAA are used by Dyke et al. (1997). The dates of the wood samples, performed mainly at the Radiocarbon Dating Laboratory of the Geological Survey of Canada, range from 9 ka BP to the present and have typical two standard-deviation error bars of 40 to 50 years. The two main types of driftwood found are spruce and larch, occasionally pine and rarely hemlock, willow, birch and aspen. The present wood identification method, based on cell morphology, determines the wood genus, but not species of conifers, except pine. Therefore, it is not yet possible to distinguish between wood of North American and Eurasian origin. However, the relative abundance of the two main wood types (larch/spruce) is starkly different on the two continents and can be used to infer the origins of the driftwood, provided that the forest compositions remained constant during this part of the Holocene epoch. The western Canadian boreal forest achieved its modern composition about 6 ka BP (Ritchie, 1989). The boreal forest of North America, west of Hudson Bay, is dominated by spruce, whereas larch is dominant in eastern Siberia, followed by pine; spruce is absent. Spruce increases in abundance westward in Siberia, but it still accounts for less than 1 % of the forest south of the Laptev Sea. Spruce eventually dominates in western Siberia south of the Kara Sea, but little or no wood from there can reach the CAA today.

The driftwood enters the Arctic Ocean from bank erosion of the major rivers. The wood pieces will remain buoyant in the ocean for approximately 12 months for larch and 17 months for spruce (Hăggblom, 1982). Since the time required for the wood to cross the Arctic Ocean and get stranded on a coastline is typically several years, sea ice is the necessary transport mechanism for the recovered wood. For this reason, changes in quantity and type of wood delivery to a given region is interpreted as a change in sea ice drift pattern and upper ocean circulation pattern, which generally follows the sea ice motion (Holland *et al.*, 1996). The stranding potential of a given coastline depends upon its orientation with respect to the ocean current, and the presence or absence of perenial ice along its shore. These factors will result in regional differences in stranded wood abundance recorded in the raised beaches. Also, driftwood present on the unvegetated[1] raised beaches of the high Arctic islands is easily detectable, whereas fewer driftwood samples could be collected and dated from the well vegetated beaches of Baffin Island and the Arctic mainland. The wood on the latter beaches may blend too well with the vegetation or might rot with time. All of these factors contribute to geographical differences in wood abundance. However, variations in wood delivery at a given location through time are interpreted as a change in the wood delivery route.

Most of the CAA can only receive wood transported by sea ice entering from the north. In contrast, the eastern ends of Jones and Lancaster sounds, Smith Sound and eastern Baffin Island can receive wood either from the Arctic via Nares Strait or from Baffin Bay via the East and West Greenland currents (figure 6.1). Based on the relative abundance of spruce vs larch in North America and Eurasia, periods can be identified where the TDS was deflected westward, bringing wood of North American (NA) and Eurasian origin to the Canadian Arctic Archipelago, and periods where the TDS was deflected eastward, bringing Eurasian wood mainly to the shores of Svalbard and NA wood into the Baffin Bay region via the East and West Greenland currents. Between these two extreme situations, a split TDS may exist as is presently the case. Figure 6.2 shows a summary of the TDS excursions during the last 9 ka as derived by Dyke et al. (1997) from the driftwood-type ratios and dated abundances. The position of the TDS seems to have varied significantly during the Holocene with century to millenial scale stable periods between shifts. Of particular interest are the relatively large number of rapid changes around 5-6 kyr BP coincident with the climatic optimum (Wright

---

[1] This is due to the high alkalinity, aridity and cold climate present in these regions

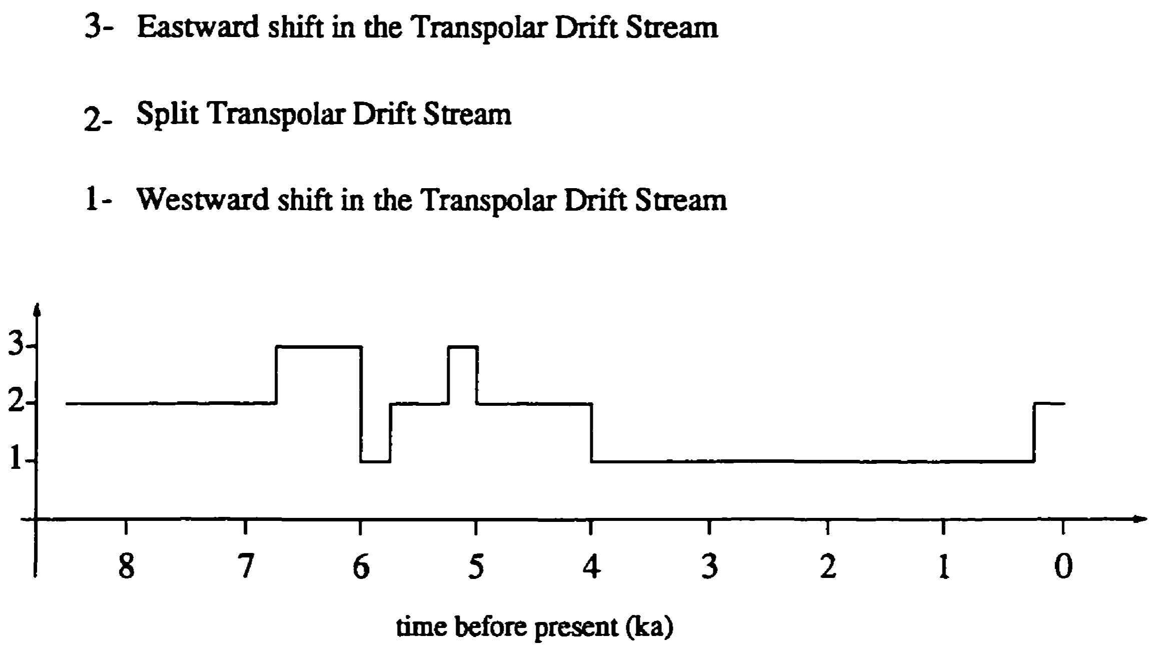

Figure 6.2: Excursions of the TDS during the last 9 kyr inferred from driftwood data collected in the Arctic Islands (data from Dyke et al. (1997)).

et al., 1993), and the relatively stable periods during the early Holocene and most of the Neoglacial period (4 ka to now). Another change in the TDS occured recently (about 250 years), which also appears to coincide with a rapid environmental change in high-Arctic ecosystems (Douglas *et al.*, 1994; Beltrami and Taylor, 1995).

6.3 Simulation results

In this section, the sea-ice model presented in chapter 2 is used to determine whether a westward, split or eastward ice delivery route can be reproduced using various atmospheric wind patterns that have been observed during the last 30 years. To do this, we analyze the situation for two anomalous years: 1968, a year with large ice export from the Arctic Ocean into the Greenland Sea; and 1984, a year with little ice export out of the Arctic. During these two years, the large-scale sea level pressure (SLP) fields were greatly different (see figure 6.3a-c). In this manner, source regions for wood caught in the Beaufort Gyre and for wood leaving the Arctic through Fram Strait can be identified.

The sea-ice model is applied to the Arctic Ocean and surrounding seas using a grid resolution of 1 degree latitude. The model is forced with prescribed monthly mean wind stresses, air temperatures and steady but spatially varying ocean currents, calculated from the single layer reduced gravity model (appendix B). The boundary conditions used for the sea ice, ocean and atmospheric models are described in section 4.

The sea-ice-ocean model was integrated for two periods of 30 years, first with 1968 and then with 1984 forcing fields to reach a stable periodic seasonal cycle for each type of forcing using a 1-day time step. The September conditions produced in these 2 simulations are then used as initial conditions for a 6-year run with a passive tracer (representing driftwood) positioned at the center of each grid cell. The tracer positions are recalculated at each time step, from the interpolated ice or upper ocean velocity vector at the tracer location. For ice concentrations in a grid cell below 50 %, the tracers are assumed to be carried by the water, and for ice concentrations above 50 %, they are assumed to be carried by the ice.

The results shown in figure 6.3 include the winter SLP patterns for winter 1968 and 1984, spaghetti[2] plots for these two forcing fields over 6 years, from which the general sea ice drift pattern can be inferred for a given atmospheric forcing field, and a detailed map of the source regions for driftwood found in the North Baffin Bay (a region only accessible by the east and west Greenland current) and the driftwood found in the central Canadian Arctic Islands (a region only accessible for driftwood entering from the Arctic Ocean). In winter 1968, the Icelandic Low had two centers, one south of Greenland (not shown here) and one in the northern part of the Norwegian Sea (figure 6.3a). This pattern coincided with a large negative North Atlantic Oscillation index (NAO) (Hurrel, 1995) and produced surface winds north of Greenland which carried large quantities of ice out of the Arctic through Fram Strait (see figure 6.3c). During this time, the Transpolar Drift Stream was far to the east and the Beaufort Gyre was confined to the western Arctic. This feature is well illustrated by the tracer trajectories shown in figure 6.3c. With this mode of atmospheric circulation, driftwood originating from the Mackenzie Delta, the Alaskan, Siberian and Russian coasts will be carried out of the Arctic by the Beaufort Gyre and the TDS (figure 6.3e). A few years later, the specimen would be found in Northern Baffin Bay, after being transported by the East and West Greenland Currents. In 1984, the NAO index was strongly positive and

---

[2] A plot of all the passive tracer trajectories during the 6-year integration.

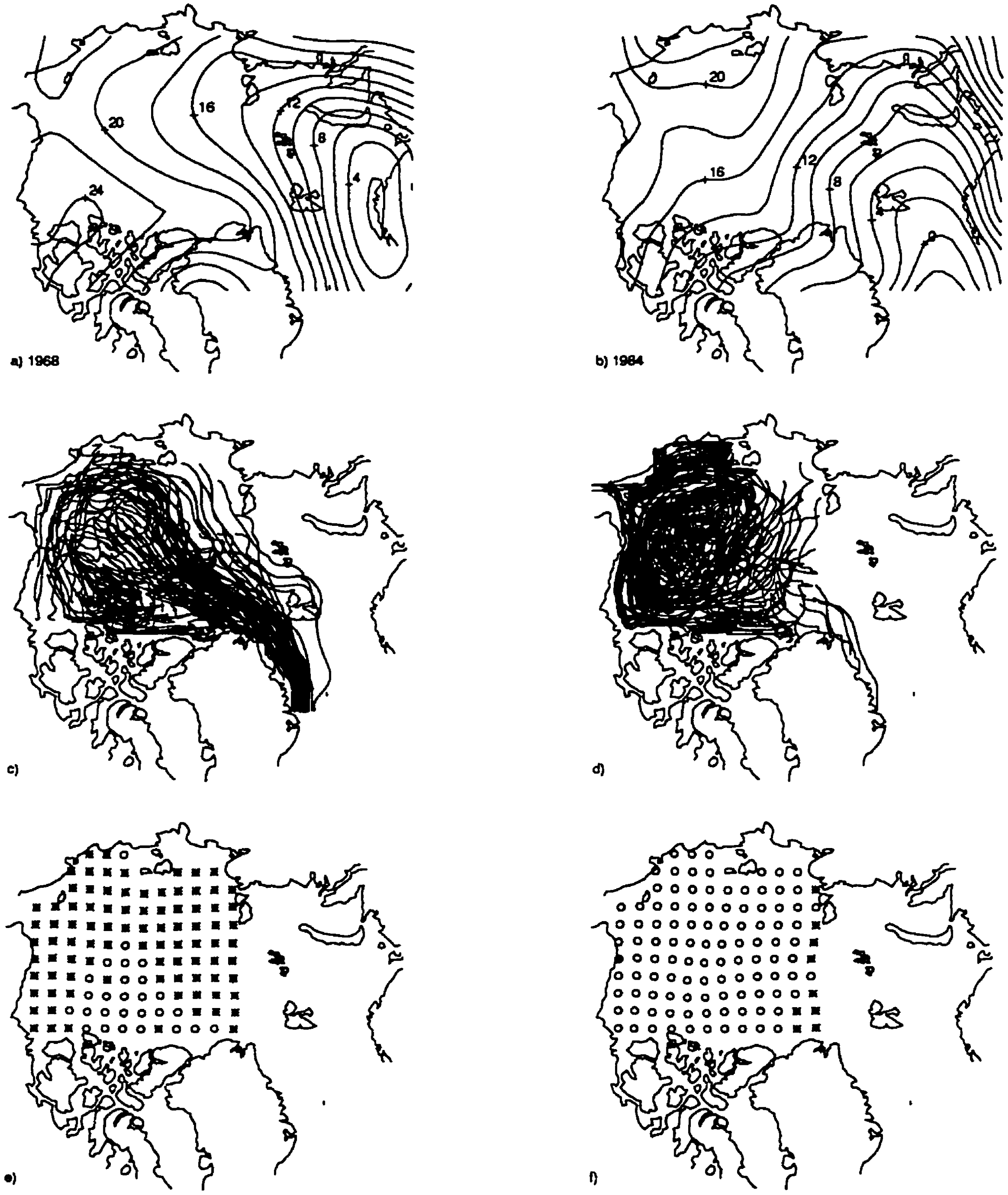

Figure 6.3: Sea level pressure pattern, spaghetti plot and driftwood sources for the years 1968 (a,c,e) and 1984 (b,d,f). In (e) and (f), the circles indicate source regions of driftwood for the central Arctic Islands (CAA) and the stars indicate the source regions for northern Baffin Bay.

the Icelandic Low had a single deep center situated around Iceland (figure 6.3b), and the isobars in the central Arctic were oriented towards the CAA. This resulted in an expanded Beaufort Gyre and a very weak TDS (figure 6.3d). With this mode of atmospheric circulation, driftwood emanating from North American and East Siberian rivers would get caught in the Beaufort Gyre and eventually strand on the beaches of the Arctic Islands, which are only accessible from the north via the various western and south-western straits and channels. The driftwood emanating from west Siberian rivers would be found in northern Baffin Bay and Svalbard. These results show that the two sea ice drift patterns could account for the two different driftwood delivery routes as hypothesized by Dyke et al., and furthermore, the sea ice drift pattern could be driven by atmospheric wind forcing that has occurred during the past few decades. Finally, an SLP pattern in between that represented in figure 6.3a and 6.3b (similar to today's climatology) could produce a split ice delivery route.

Chapter 7

Conclusions

A thermodynamic-dynamic sea-ice model is coupled to both a mixed-layer ocean and a one-layer thermodynamic atmospheric model. In the sea-ice component of this model, the ice is considered as a large-scale granular material, i.e., a collection of ice floes. The deformation in the ice field is considered slow enough that the floes remains in contact during deformation, allowing frictional forces to act and retard the sea-ice drift. At a point, this frictional force is considered proportional to the normal force keeping the floes together. This situation is analogous to the case of dynamic friction between two dry surfaces. The model also allows for a variable internal angle of friction and a certain amount of dilatation in the granular media which depends on the distribution of the ice floes and the deformation history. This dilatation causes leads to open and consequently always maintain a small percentage of the ocean surface ice free, which is commonly observed in the Arctic. This behaviour arises naturally from the simple assumption made in the derivation of the constitutive relation based on the behaviour of sea ice on the microscopic level, and eliminates the need to rely on parameterization of lead opening. In this study, the angle of friction is considered constant and the amount of dilatation is proportional to the shear deformation. The drag coefficient used in this study is proportional to ice thickness in order to account for the fact that thick ice is formed by ridging and is usually rougher.

A long term (10-year) integration of the thermodynamically coupled ocean-ice-atmosphere model could reproduce many observed features of the Arctic sea-ice cover, both in winter and in summer. Regions of large-scale sliding observed along leads extending from the Beaufort Sea to the central Arctic are well reproduced by the model. In addition, the observed opening of leads associated with this shear deformation is well simulated. The ice thickness distribution over the entire Arctic agrees quite well with sonar measurements, for both winter and summer, with maximum and minimum ice thicknesses of 7 and 1 meter respectively. This is partly due to the linear dependance of the drag coefficients on ice thickness (Tremblay and Mysak, 1997 in press). The ice edge position in summer also agrees well with satellite observation. In particular, the model produces ice free regions in the marginal seas during this season.

The possible causes of interannual variability of the sea-ice cover in the Beaufort-Chukchi seas is investigated. The three factors considered include the effects of Mackenzie river runoff (and upper ocean stratification), atmospheric temperature and wind stress anomalies. Based on simple first order calculations, analysis of sea level atmospheric temperature and wind stress data, and sea ice model simulations, we conclude that anomalous wind patterns in the western Arctic are the principal cause of interannual variability in the Beaufort-Chukchi seas. In particular, a simulation of the 1964-65 sea ice cover forced with 1964-65 wind stresses and climatological atmospheric temperature could reproduce very well the observed anomaly signal. In contrast, when forced with the climatological wind stress and 1964-65 atmospheric temperature, the Beaufort sea ice conditions are very similar to climatology. The influence of anomalous atmospheric temperature on anomalous ice condition is believed to play an important role for slightly longer time scale fluctuations (2-3 years). Regarding the influence of sea surface salinity on ice conditions, an analysis shows that a reduction in river runoff causing a decrease in stratification will have a larger influence on sea ice conditions than an increase river runoff. Although fluctuations in the input of fresh water into the Arctic is not dominant in creating interannual variations in the sea ice cover, it could play an important role for longer time scales (> 10 years).

The possibility that ice anomalies in the Beaufort Sea could be advected around the Beaufort Gyre and lead to a significant anomaly in the sea ice export out of the Arctic through Fram Strait is also studied. A simulation of the time evolution of an ice anomaly representative of the one observed in the western Beaufort Sea in 1965, was performed with a three years integration. The results show that, at the end of the simulation, the ice anomaly had reached the Fram Strait and still had 20 % of its original magnitude. For a typical ice thickness in the Fram Strait of 2 meters this constitute a 20 % ice volume anomaly, which is smaller but certainly not negligible as compared with the ice concentration anomalies of 35 % observed in this region from satellite observations. It is generally concluded that ice conditions in the peripheral seas in the Arctic basin can contribute to the variability in ice export from the Arctic into the Greenland Sea.

Based on the age and type of drifwood samples collected on the raised beaches of the Canadian Arctic Islands, postglacial oscillations of the Transpolar Drift Stream were hypothesized (Dyke *et al.*, 1997). In the last 9 000 years, long periods (from centuries to a few ka) existed when wood of North American and Siberian origin was mainly found on the beaches of northern Baffin Bay, a region mainly accessible via the East and West Greenland Current, or on the beaches of the western and south-western part of the Canadian Arctic Archipelago, which are only accessible from the north through various channels and straits. From these observations, it was hypothesized that periods with a weak Beaufort Gyre and broad TDS, or a large Beaufort Gyre and a narrow TDS were mainly responsible for the observed change in wood delivery route.

Results from a 6 year integration of a coupled ocean-sea-ice model using widely different observed atmospheric wind forcings confirm this hypothesis. For wind forcing typical of 1968, a year with a strong negative North Atlantic Oscillation (NAO) index, large quantities of sea ice are exported out of the Arctic into the Greenland Sea. Under these conditions, driftwood of North American, Siberian and Russian origin is transported by sea ice out of the Arctic and eventually can strand on the beaches of northern Baffin Bay. For winds typical of 1984, a year with a strong positive NAO index, driftwood of North American and Siberian origin is caught in the Beaufort Gyre and stranded on the beaches of the central Arctic. The driftwood record suggests that for long periods of the Holocene, the atmospheric circulation ressembled that of a negative or positive NAO index and abruptly changed from one to the other.

Bibliography

Aagaard, K. and Carmack, E. C. (1989). The role of sea ice and other fresh water in the Arctic circulation. *Journal of Geophysical Research*, 94:14485–14498.

Anderson, R. J. (1987). Wind stress measurements over rough ice during the 1984 marginal ice zone experiment. *Journal of Geophysical Research*, 92:6933–6941.

Babic, M., Shen, H. H., and Shen, H. T. (1990). The stress tensor in granular shear flows of uniform, deformable disks at high solids concentrations. *Journal of Fluid Mechanics*, 219:81–118.

Balendran, B. and Nemat-Nasser, S. (1993). Double sliding model for cyclic deformation of granular materials, including dilatancy effects. *Journal of the Mechanics and Physics of Solids*, 41:573–612.

Beltrami, H. and Taylor, A. E. (1995). Records of climatic change in the Canadian Arctic: towards calibrating oxygen isotope data with geothermal data. *Global and Planetary Change*, 11:127–138.

Bjornsson, H., Mysak, L. A., and Brown, R. D. (1995). On the interannual variability of precipitation and runoff in the Mackenzie drainage basin. *Climate Dynamics*, 12:67–76.

Bourke, R. H. and Garrett, R. P. (1987). Sea ice thickness distribution in the Arctic Ocean. *Cold Regions Science and Technology*, 13:259–280.

Broecker, W. S., Peteet, D. M., and Rind, D. (1985). Does the ocean-atmosphere system have more than one stable mode of operation? *Nature*, 315:21–26.

Campbell, C. (1990). Rapid granular flows. *Annual Review of Fluid Mechanics*, 22:57–92.

Campbell, W. J. (1965). The wind-driven circulation of ice and water in the polar ocean. *Journal of Geophysical Research*, 70:3279–3301.

Campbell, W. J. and Rasmussen, L. A. (1972). A numerical model for sea ice dynamics incorporating three alternative ice constitutive laws. In KARLSSON, T., editor, *Sea Ice: Proceedings of an International Conference*, pages 176–187, National Research Research Council of Iceland, Reykjavik, Iceland.

Chouinard, L. E. and Garrigues, L. (1995). Interannual variability of the ice cover in the Chukchi and Beaufort seas. In *Proceeding of the Fifth (1995) International Offshore and Polar Engineering Conference, The Hague, The Netherlands*, pages 357–363. The International Society of Offshore and Polar Engineering.

Colony, R. and Thorndike, A. S. (1984). An estimate of the mean field of Arctic sea ice motion. *Journal of Geophysical Research*, 89:10623–10629.

Coon, M. D., Maykut, S. A., Pritchard, R. S., Rothrock, D. A., and Thorndike, A. S. (1974). Modelling the packice as an elastic plastic material. *AIDJEX Bulletin*, 24:1–105.

Dickson, R. R., Lamb, H. H., Malmberg, S.-A., and Colebrook, J. M. (1975). Climatic reversal in northern North Atlantic. *Nature*, 256:479–482.

Doronin, Y. P. (1970). On a method of calculating the compactness and drift of ice floes (english translation). *AIDJEX Bulletin*, 3:22–39.

Douglas, M. S. V., Smol, J. P., and Blake Jr, W. (1994). Marked post-18th century environmental change in high-Arctic ecosystems. *Science*, 266:416–419.

Dyke, A. S., England, J., Reimnitz, E., and Jetté, H. (1997). Changes in driftwood delivery to the Canadian Arctic Archipelago: the hypothesis of postglacial oscillations of the transpolar drift. *Arctic*, (in press).

Erlingsson, B. (1988). Two-dimensional deformation pattern in sea ice. *Journal of Glaciology*, 34:301–308.

Flato, G. M. and Hibler, III, W. D. (1992). Modeling pack ice as a cavitating fluid. *Journal of Physical Oceanography*, 22:626–651.

Flemming, G. H. and Semtner, A. J. (1991). A numerical study of interannual ocean forcing on Arctic sea ice. *Journal of Geophysical Research*, 96:4589–4603.

Gill, A. E. (1982). *Atmosphere-Ocean Dynamics.* Academic Press Inc., 1 edition.

Glen, J. W. (1970). Thoughts on a viscous model for sea ice. *AIDJEX Bulletin*, 3:18–27.

Goose, H., Campin, J. M., Fichefet, T., and Deleersnijder, E. (1996). Sensitivity of a global ice-ocean model to the Bering Srait throughflow. *Climate Dynamics (submitted).*

Gray, J. M. N. T. and Morland, L. W. (1994). A two-dimensional model for the dynamics of sea ice. *Philosophical Transactions of the Royal Society of London*, 347:219–290.

Häggblom, A. (1982). Driftwood in Svalbard as an indicator of sea ice conditions. *Geografiska Annaler*, 64A:81–94.

Häkkinen, S. (1993). An Arctic source for the great salinity anomaly: A simulation of the Arctic ice-ocean system for 1955-1975. *Journal of Geophysical Research*, 98(C9):16,397–16,410.

Hibler, III, W. D. (1977). A viscous sea ice law as a stochastic average of plasticity. *Journal of Geophysical Research*, 82:3932–2938.

Hibler, III, W. D. (1979). A dynamic thermodynamic sea ice model. *Journal of Physical Oceanography*, 9:815–846.

Hibler, III, W. D. and Walsh, J. E. (1982). On modeling seasonal and interannual fluctuations of Arctic sea ice. *Journal of Physical Oceanography*, 12:1514–1523.

Holland, D. M. (1993). *Numerical Simulation of the Arctic Sea Ice and Ocean Circulation.* Ph.D. thesis, McGill University, Dept. of Atmos. and Ocean. Science, McGill University, Montreal.

Holland, D. M., Mysak, L. A., and Manak, D. K. (1993). Sensitivity study of a dynamic-thermodynamic sea-ice model. *Journal of Geophysical Research*, 98:2561–2586.

Holland, D. M., Mysak, L. A., and Oberhuber, J. M. (1996). Simulation of the mixed-layer circulation in the Arctic Ocean. *Journal of Geophysical Research*, 101:1111–1128.

Hopkins, M. A. (1994). On the ridging of intact lead ice. *Journal of Geophysical Research*, 99:16351–16360.

Hurrel, J. W. (1995). Decadal trends in the North Atlantic oscillation: Regional temperatures and precipitation. *Science*, 269:676–679.

Hutter, K. and Rajagopal, K. R. (1994). On flows of granular materials. *Continuum Mechanics and Thermodynamics*, 6:81–139.

Kozo, T. L., Fett, R. W., Farmer, L. D., and Sodhi, D. S. (1992). Clues to causes of deformation features in coastal sea ice. *Eos Transactions (American Geophysical Union)*, 73:385–389.

Laevastu, T. (1960). Factors affecting the temperature of the surface layer of the sea. *Commentationes physico-mathematicae*, 25(1).

Laikhtman, D. L. (1958). O dreife ledyanykh polei (the drift of ice fields). *Trudy Leningradskogo Gidrometeo*, 7.

Levitus, S. (1994). World ocean atlas 1994, cd-rom data sets.

Manak, D. K. and Mysak, L. A. (1989). On the relationship between Arctic sea-ice anomalies and fluctuations in northern canadian air temperature and river discharge. *Atmosphere-Ocean*, 27(4):682–691.

Marko, J. R. and Thompson, R. E. (1977). Rectilinear and internal motions in the ice pack of the western Arctic Ocean. *Journal of Geophysical Research*, 82:979–987.

Martinson, D. G. and Wamser, C. (1990). Ice drift and momentum exchange in winter Antarctic pack ice. *Journal of Geophysical Research*, 95:1741–1755.

Maykut, G. A. and Perovitch, D. K. (1987). The role of shortwave radiation in the summer decay of s sea ice cover. *Journal of Geophysical Research*, 92:7032–7044.

Maykut, G. A. and Untersteiner, N. (1971). Some results from a time-dependent thermodynamic model of sea ice. *Journal of Geophysical Research*, 76:1550–1575.

McGillivray, D. G., Agnew, T., Pilkington, G. R., Hill, M. C., McKay, G. A., Smith, J. D., McGonigal, D., and LeDrew, E. F. (1992). Impacts of climatic change on the Beaufort sea-ice regime: Implications for the Arctic petroleum industry. Technical Report 92-6, February, Atmospheric Environment Service, Climate Information Branch Canadian Climate Center, Atmospheric Service, 4905 Dufferin Sreet, Downsview, Ontario, Canada M3H 5T4.

McLaren, A. S., Serreze, M. C., and Barry, R. G. (1987). Seasonal variations of sea ice motion in the canada basin and their implications. *Geophysical Research Letters*, 14:1123–1126.

McPhee, M. G. (1975). Ice-ocean momentum transfer for the aidjex ice model. *AIDJEX Bulletin*, 29:93–111.

Mulherin, N. D. (1996). The northern sea route: its development and evolving state of operations in the 1990s. Technical Report 96-3, April, Cold Regions Research and Engineering Laboratory (CRREL), Corps of engineers, 72 Lyme Road, Hanover, New Hampshire, USA 03755-1290.

Mysak, L. A., Manak, D. K., and Marsden, R. F. (1990). Sea-ice anomalies observed in the Greenland and Labrador seas during 1901–1984 and their relations to an interdecadal Arctic climate cycle. *Climate Dynamics*, 5:111–113.

Mysak, L. A. and Power, S. B. (1992). Sea-ice anomalies in the western Arctic and Greenland-Iceland sea and their relation to an interdecadal climate cycle. *Climatological Bulletin*, 26(3):147–176.

Nansen, F. (1902). The oceanography of the North pole basin, the norwegian polar expedition. 1893–1896. *Scientific Results*, 3:357–386.

Nikiforov, Y. B., Gudkovitch, Z. M., Yefimov, Y. I., and Romanov, M. A. (1970). Principles of a method for computing ice redistribution under the influence of wind during the navigation period in Arctic seas. *AIDJEX Bulletin*, 3:40–64.

Overland, J. E. and Pease, C. H. (1988). Modeling ice dynamics of coastal seas. *Journal of Geophysical Research*, 93:15619–15637.

Parmerter, R. R. and Coon, M. D. (1973). Mechanical models of ridging in the sea ice cover. *AIDJEX Bulletin*, 19:59–112.

Popov, E. (1952). *Mechanics of materials.* Prentice Hall.

Press, W. H., Flannery, B. P., Teukolsky, S. A., and Vetterling, W. T. (1990). *Numerical recipes.* Cambridge university press, 2 edition.

Pritchard, R. (1988). Mathematical characteristics of sea ice dynamics models. *Journal of Geophysical Research*, 93(C12):15609–15618.

Ritchie, J. C. (1989). History of the boreal forest in Canada. In FULTON, R. J., editor, *Quaternary Geology of Canada and Greenland*, number 1, pages 508–512. Geological Survey of Canada, Geology of Canada.

Rogers, J. C. (1977). A meteorological basis for long-range forecasting of summer and early autumn sea ice conditions in the Beaufort sea. In MUGGERIDGE, D. B., editor, *Proceeding of the Fourth International Conference on Port and Ocean Engineering under Arctic Conditions*, pages 952–962, Memorial University, St-John's, Newfoundland.

Rothrock, D. A. (1973). The steady drift of an incompressible Arctic ice cover. *AIDJEX Bulletin*, 21:49–78.

Ruzin, M. I. (1959). The wind drift of ice in a heterogenous pressure field. *Arkticheskii i Antarckticheskii Nauchno-Issled. Inst., Trudy*, 226:123–135.

Shen, H. H., Hibler, W. D. I., and Leppäranta, M. (1986). On applying granular flow theory to a deforming broken ice field. *Acta Mech.*, 63:143–160.

Smith, W. O. (1990). *Polar Oceanography. Part A: Physical Science.* Academic Press.

Spencer, A. J. M. (1964). A theory of the kinematics of ideal soils under plane strain conditions. *Journal of the Mechanics and Physics of Solids*, 12:337–351.

Stern, H. L., Rothrock, D. A., and Kwok, R. (1995). Open water production in Arctic sea ice: Satellite measurements and model parameterizations. *Journal of Geophysical Research*, 100:20601–20612.

Stössel, A. and Claussen, M. (1993). On the momentum forcing of a large-scale sea-ice model. *Climate Dynamics*, 9:71–80.

Sverdrup, H. U. (1928). The wind-drift of the ice on the north siberian shelf. *The Norwegian North Polar Expedition With the "Maud", 1918-1925, Scientific Results*, 4:1077–1099.

Tremblay, L.-B. and Mysak, L. A. (1997). Modelling sea ice as a granular material, including the dilatancy effect. *Journal of Physical Oceanography*, (in press).

Tremblay, L.-B. and Mysak, L. A. (1997, in press). The possible effects of including ridge-related roughness in air-ice drag parameterization: a sensitivity study. *Annals of Glaciology*, (in press).

Tucker, W. B. and Westhall, V. H. (1973). Arctic sea ice frequency distribution derived from laser profiles. *AIDJEX Bulletin*, 21:171–180.

Ukita, J. and Moritz, R. E. (1995). Yield curves and flow rules of pack ice. *Journal of Geophysical Research*, 100:4545–4557.

Walsh, J. E. and Chapman, W. L. (1990). Arctic contribution to upper-ocean variability in the North Atlantic. *Journal of Climate*, 3:1462–1473.

Weatherly, J. W. and Walsh, J. E. (1996). The effects of precipitation and river runoff in a coupled ice-ocean model of the Arctic. *Climate Dynamics*, 12:785–798.

Wright, H. E., Kutzbach, J. E., Webb, T., Ruddiman, W. F., Street-Perrot, F. A., and Bartlein (1993). *Global climates since the last glacial maximum.* University of Minnesota Press.

Zillman, J. W. (1972). A study of some aspect of the radiation heat budget of the southern hemisphere oceans. Technical Report 26, Bureau of Meteorology, Department of Interior, Camberra, Australia.

Appendix A

Physical parameters and constants used in the simulation

Table A.1: Physical parameters and constants used in the simulation

Variable	symbol	value
Atmospheric albedo	α_a	0.26
Ice albedo	α_i	0.70
Land albedo	α_l	0.20
Ocean albedo	α_o	0.17
Angle of dilatancy	δ	20 degrees
Atmospheric emissivity	ϵ_a	0.88
Ice emissivity	ϵ_i	0.97
Land emissivity	ϵ_l	0.90
Ocean emissivity	ϵ_o	0.96
Planetary emissivity	ϵ_p	0.50
Internal angle of friction	ϕ	30 degrees
Maximum ice viscosity	η_m	1×10^{12} kg/m/s
Air density	ρ_a	1.3 kg/m^3
Ice density	ρ_i	900 kg/m^3
Land density	ρ_l	13×10^3 kg/m^3
Water density	ρ_w	10^3 kg/m^3
Stefan-Boltzmann constant	σ	5.67×10^{-8} W/(m^{2}K^4)
Air and water turning angle	θ_a, θ_w	25 degrees

Table A.2: Physical parameters and constants used in the simulation, (continued)

Variable	symbol	value
Saturation vapour pressure constants	A_1, A_2	7.5, 35.86
Ice strength parameter	C	20
Air drag coefficient	C_{da}	1.2×10^{-3}
Water drag coefficient	C_{dw}	5.5×10^{-3}
Latent heat transfer coefficient	C_{lat}	1×10^{-3}
Specific heat of air	C_{pa}	1×10^{3} J/(Kg K)
Specific heat of ice	C_{pi}	2×10^{3} J/(Kg K)
Specific heat of land	C_{pl}	0.7×10^{3} J/(Kg K)
Specific heat of water	C_{pw}	4×10^{3} J/(kg K)
Sensible heat coefficient	C_{sens}	1×10^{-3}
Atmospheric scale height	H_a	7×10^{3} m
Land thickness	H_l	6 m
Ocean mixed layer depth	H_o	60 m
Diffusion coefficient for A	K_A	50 m^2/ s
Atmospheric diffusion coefficient	K_a	5×10^{12} m^2/ s
Diffusion coefficient for h	K_h	50 m^2/s
Ice thermal conductivity	K_i	2 W/(m^2K)
Land thermal conductivity	K_l	2 W/(m^2K)
Ocean diffusion coefficient	K_o	1×10^{10} m^2/s
Latent heat of evaporation	L_e	2.50×10^{6} J / kg
Latent heat of fusion	L_f	3.30×10^{5} J / kg
Latent heat of sublimation	L_s	2.83×10^{6} J / kg

Table A.3: Physical parameters and constants used in the simulation, (continued)

Variable	symbol	value
Ice strength in compression	P_{max}	7×10^3 N/m^2
Sea level pressure	P_s	101.3×10^3 Pa
Solar radiation constant	Q_0	1×10^3 W/m^2
Ocean freezing point	T_{fp}	-1.8 C°
Fresh water freezing point	T_{fi}	0 C°
Land base temperature	T_{lb}	6.0 C°
Atmospheric absorptivity	a_a	0.25
Coriolis parameter	f	1.5×10^{-4} s^{-1}
Gravitational acceleration	g	9.81 m/s^2

Appendix B

1-layer reduced gravity ocean model

In this section, the governing equations for the 1-layer reduced gravity ocean model are presented. Consider an active ocean layer of mean depth h overlying the deeper ocean (assumed at rest), as shown in figure B.1. For this system, the continuity and momentum equations can be written as follows:

$$\begin{aligned} \frac{\partial \eta}{\partial t} + \nabla \cdot [\boldsymbol{u}_w (h + \eta)] &= 0, & \text{(B.1)} \\ \rho_w f \boldsymbol{k} \times \boldsymbol{u}_w &= -\rho_w g' \nabla \eta + A \frac{\boldsymbol{\tau}_{iw}}{h + \eta} + (1 - A) \frac{\boldsymbol{\tau}_{aw}}{h + \eta} - \frac{\boldsymbol{\tau}_b}{h + \eta}, & \text{(B.2)} \end{aligned}$$

where η is the pycnocline displacement, $\boldsymbol{u}_w$ the ocean horizontal velocity vector, ρ_w the active ocean layer density, f the Coriolis parameter, g' the reduced gravity $g(\rho_2 - \rho_w)/\rho_w$, $\boldsymbol{\tau}_{iw}$ and $\boldsymbol{\tau}_{aw}$ the ice-ocean and atmosphere-ocean stresses and $\boldsymbol{\tau}_b$ the bottom drag. Note that in B.1, there is no term on the right-hand side which represents entrainment from below the ocean mixed-layer. The ice-ocean and atmosphere stresses are written as (see 2.2 and 2.3):

$$\begin{aligned} \boldsymbol{\tau}_{iw} &= \rho_w \underbrace{C_{d,iw} |\boldsymbol{u}_i - \boldsymbol{u}_w^g|}_{C'_{d,iw}} [(\boldsymbol{u}_i - \boldsymbol{u}_w^g) \cos \theta_w + \boldsymbol{k} \times (\boldsymbol{u}_i - \boldsymbol{u}_w^g) \sin \theta_w], & \text{(B.3)} \\ \boldsymbol{\tau}_{aw} &= \rho_a \underbrace{C_{d,aw} |\boldsymbol{u}_a|}_{C'_{d,aw}} [\boldsymbol{u}_a^g \cos \theta_a + \boldsymbol{k} \times \boldsymbol{u}_a^g \sin \theta_a], & \text{(B.4)} \\ \boldsymbol{\tau}_b &= \rho_w C_{dw} \boldsymbol{u}_w^g, & \text{(B.5)} \end{aligned}$$

where $C_{d,iw}$, $C_{d,aw}$ and C_{dw} are the ice-ocean, atmosphere-ocean and bottom drag coefficients, $\boldsymbol{u}_a^g$ and $\boldsymbol{u}_w^g$ the geostrophic winds and ocean currents, $\boldsymbol{u}_i$ the ice velocity vector, θ_w and θ_a

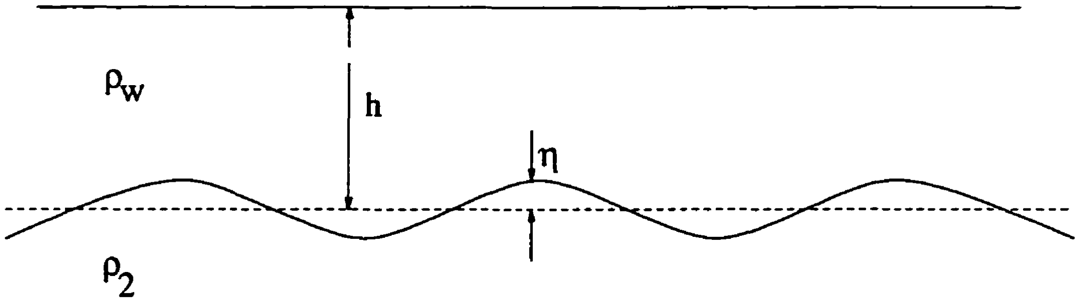

Figure B.1: 1-layer reduced gravity ocean model

the wind and ocean turning angle and ρ_a the air density. In the following, the f-plane approximation is used (f = const, $\beta = 0$) and $h = 200$ is chosen since this gives an internal Rossby radius of deformation of about 20 km, which is typical for high latitudes.

Upon replacing the geostrophic ocean currents $\boldsymbol{u}_w^g$ by

$$g'/f\boldsymbol{k} \times \nabla\eta, \tag{B.6}$$

in the right hand side of the momentum equation B.2, we can then write it in terms of η only as follows:

$$\begin{aligned}(h+\eta)\boldsymbol{u}_w &= -\frac{g'}{f^2}\begin{bmatrix} C'_{d,iw}\cos\theta_w A + C_{dw} & -C'_{d,iw}\sin\theta_w A + f(h+\eta) \\ C'_{d,iw}\sin\theta_w A - f(h+\eta) & C'_{d,iw}\cos\theta_w A + C_{dw}\end{bmatrix}\begin{pmatrix}\frac{\partial\eta}{\partial x} \\ \frac{\partial\eta}{\partial y}\end{pmatrix} \\ &+\frac{1}{f}\begin{pmatrix} C'_{d,iw}A(v_i\cos\theta_w + u_i\sin\theta_w) + C'_{d,aw}\frac{\rho_a}{\rho_w}(1-A)(v_a\cos\theta_a + u_a\sin\theta_a) \\ C'_{d,iw}A(-u_i\cos\theta_w + v_i\sin\theta_w) + C'_{d,aw}\frac{\rho_a}{\rho_w}(1-A)(-u_a\cos\theta_a + v_a\sin\theta_a)\end{pmatrix}\end{aligned} \tag{B.7}$$

Substituting in the continuity equation B.1, we obtain an evolution equation for η

$$\begin{aligned}\eta_t &= \frac{g'}{f^2}(C'_{d,iw}A\cos\theta_w + C_{dw})\nabla^2\eta - \frac{C'_{d,iw}}{f}A(\nabla\times\boldsymbol{u}_i\cos\theta_w + \nabla\cdot\boldsymbol{u}_i\sin\theta_w) \\ &-\frac{C'_{d,aw}}{f}\frac{\rho_a}{\rho_w}(1-A)\ \nabla\times\boldsymbol{u}_a\cos\theta_a\end{aligned} \tag{B.8}$$

In this model, the ocean layer thickness η is defined at the corners of the grid cell and the geostrophic ocean current are defined on the B-grid (figure 3.1). The finite difference form of the above equation is:

$$\frac{\eta_{i,j}^{t+1}-\eta_{i,j}^{t}}{\Delta t}=\alpha\left(\frac{\eta_{i+1,j}^{t}-2\eta_{i,j}^{t}+\eta_{i-1,j}^{t}}{\Delta x^2}+\frac{\eta_{i,j+1}^{t}-2\eta_{i,j}^{t}+\eta_{i,j-1}^{t}}{\Delta y^2}\right)+F_{i,j}^{t},$$

where Δt is the time step, Δx and Δy the grid size in the x and y-directions, α the constant in front of the Laplacian (equation B.8) and F the forcing term. From the new η field, the geostrophic ocean current can be updated from equation B.6.

The adjustment time scale for the η field is:

$$[T]\approx\frac{f^2[L]^2}{g'C_{d,iw}}\approx 10\text{years},$$

where $[L]$ is a typical basin width (1000 km). Since the time scale is long compared to a year, the ocean current does not have time to adjust to the seasonal variations in the wind forcing and are calculated once and considered constant for all simulations.

The boundary conditions used for the ocean model are no normal flow on continental boundaries and a specified normal component of velocity at open boundaries. To first order, the ocean currents are in geostrophic balance and the above constraint on velocity is written in terms of η as follows

$$\frac{\partial\eta}{\partial s}=\begin{cases}0, & \text{closed boundary}\\ u_n, & \text{open boundary}\end{cases}$$

where s is the direction parallel to the coast and u_n the normal component of current at an open boundary. In this manner, the η field is known to within a constant (set to zero) on the boundaries.

Appendix C

The influence of river runoff on ocean surface salinity and mixed-layer depth

In this section, we provide a more complete analysis of the effect of river runoff on the sea surface salinity and mixed layer depth. In the spring, fresh water from river runoff and sea ice melt mixes with deeper saltier ocean water under the action of waves, winds and tides, resulting in a rise in the potential energy of the system. Keeping the energy input (or rise in potential energy) constant from year to year, the influence of variable river runoff on the mixed layer depth and sea surface salinity can be isolated.

Figure C.1 shows the ocean surface layer before and after mixing of fresh water from river runoff and sea ice melt has occured. The rise in the potential energy of the system per unit area after mixing, can be written as follows (see Gill (1982), p 139):

$$\rho_1 H_{ml} g \frac{H_{ml}}{2} - \left[\rho_2 (H_{ml} - h_f) g \frac{H_{ml} - h_f}{2} + \rho_w h_f g (H_{ml} - h_f/2) \right]$$

where ρ_1 is the average density of the water below the mixed layer, ρ_1 and ρ_w are the mixed layer and fresh water densities, g the gravitational acceleration, H_{ml} the mixed layer depth, h_f the thickness of the fresh water layer $(Q_M + Q_{im})/A_{BS}$, where Q_M and Q_{im} are the average volume input of fresh water from the Mackenzie River and sea ice melt, and A_{BS} is the Beaufort Sea surface area. In the above equation, the reference level for the calculation

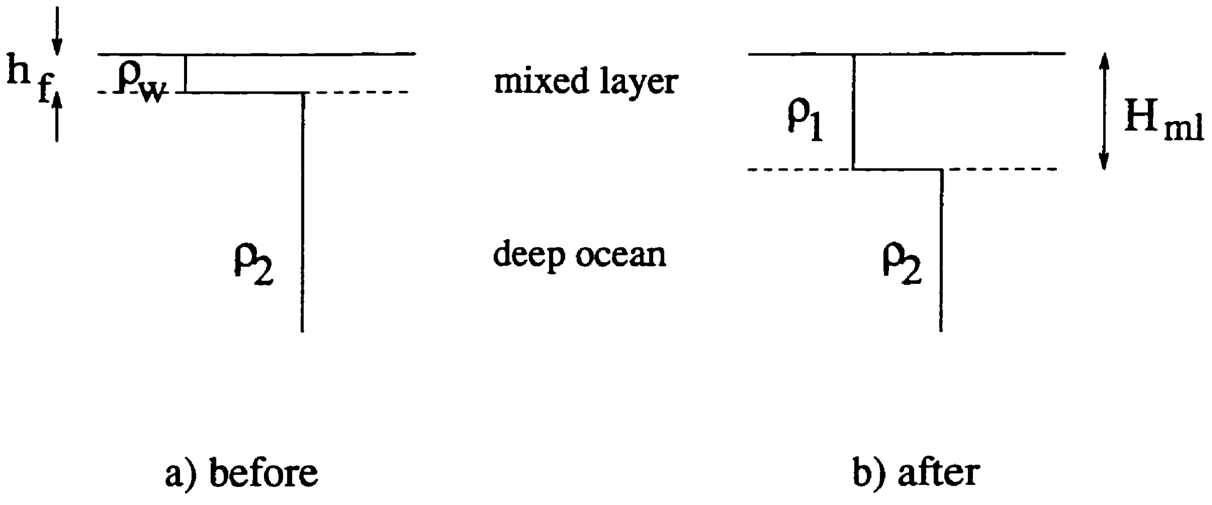

Figure C.1: Schematic of the ocean surface layer before, (a), and after, (b), mixing with the deeper ocean took place.

of the potential energies is taken at the base of the mixed layer (figure C.1b). From the conservation of mass principle, the density of the mixed layer, ρ_1, can be written in terms of the fresh water layer thickness h_f and other constants (ρ_2,ρ_w and H_{ml}) as follows:

$$\rho_1 = \rho_2 - (\rho_2 - \rho_w)\frac{h_f}{H_{ml}},$$

and the rise in potential energy of the system per unit area is finally written as

$$\frac{1}{2}(\rho_2 - \rho_w)gh_f(H_{ml} - h_f).$$

The salinity of the surface layer after mixing has occurred can be written as follows:

$$S_1 = \frac{H_{ml} - h_f}{H_{ml}}S_2, \tag{C.1}$$

where S_1 is the mixed layer salinity and S_2 is an average salinity below the mixed layer. For a mixed layer depth of 20 m (figure C.2), S_2 of 31 ppt, a Mackenzie River runoff of 300 km^3 spread uniformly over the Beaufort Sea area (300 × 10^3 km^2) and a sea ice melt thickness of 1 meter, the thickness of the fresh water layer (h_f) is 2 meters and the salinity difference between the top and bottom layer calculated from equation C.1 is 3.1 ppt. This is in general agreement with measurements made in the western Beaufort Sea (see figure C.2). Assuming the rise in the potential energy of the system remains the same from year to year, we have

$$h'_f(H'_{ml} - h'_f) = h_f(H_{ml} - h_f),$$

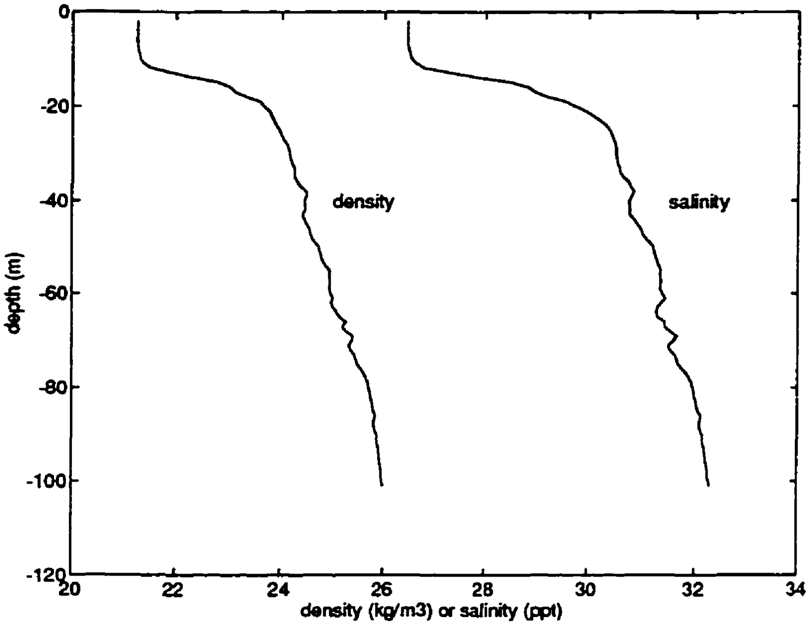

Figure C.2: Density and salinity profiles with depth in the western Beaufort Sea. This data was kindly provided by E.C. Carmack.

and thus the new mixed layer depth (H'_{ml}) for an increase river runoff (h'_f) is

$$H'_{ml} = \frac{h_f}{h'_f}(H_{ml} - h_f) + h'_f. \tag{C.2}$$

Figure C.3 shows the variation of the mixed layer depth and salinity for a Mackenzie River runoff varying between 0 and twice the climatological value, as calculated from equation C.2 and C.1. We can see from this figure that increasing the river runoff has a smaller influence on the stratification than a reduction in river runoff. Also, for a 17 % increase in MacKenzie River runoff, as observed in 1965, the reduction in mixed layer depth is approximately 1.2 meters (figure C.3); this results in a 0.48 ppt reduction in sea surface salinity (figure C.3).

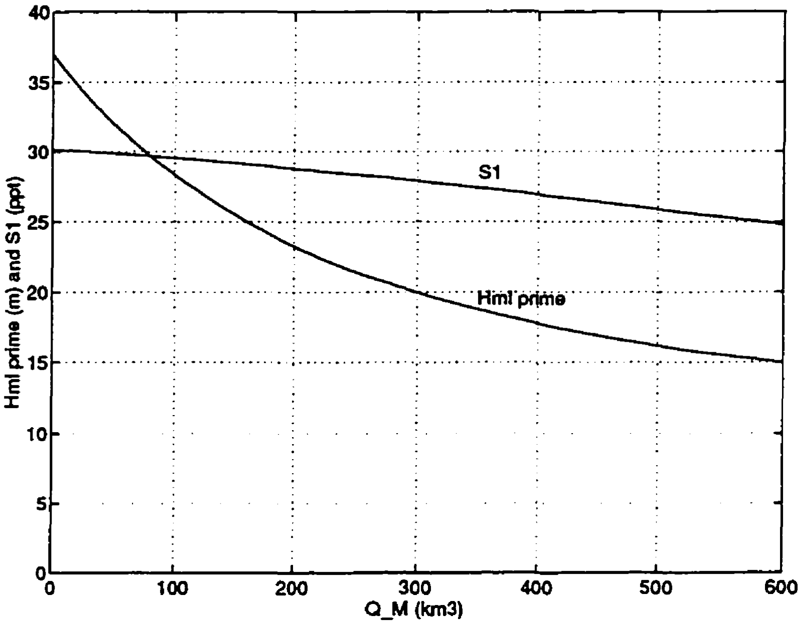

Figure C.3: Mixed layer depth and salinity as a function of Mackenzie River runoff.

Appendix D

The possible effects of including ridge-related roughness in air-ice drag parameterization: a sensitivity study[1]

L.-B. Tremblay[1] and L.A. Mysak[2]

(Annals of Glaciology, accepted for publication, September 1996)

The effects of including ridge-related roughness in the drag parameterization on the ice thickness distribution is investigated using a sea-ice dynamic and thermodynamic model. A long-term integration of the sea ice model forced by the 5-day running mean of daily geostrophic winds and steady but spatially varying ocean currents was performed to construct climatological thickness fields. Compared to the case of a constant drag coefficient, the results including the roughness have a significantly different spatial distribution with much thicker ice in the western Arctic; this is in better agreement with observations.

---

[1] References quoted in this paper are incorporated in the reference list in the thesis (see pp 78–84)

[2] Department of Atmospheric and Oceanic Sciences and Centre for Climate and Global Change Research, McGill University, 805 Sherbrooke St. West, Montreal, Quebec Canada, H3A 2K6.

D.1 Introduction

The presence of sea ice in the polar regions has a substantial influence on the global climate. In particular, the sea ice acts as an insulator, reducing the amount of ocean heat lost to the atmosphere. In turn, the ability of ice to insulate is a strong function of its thickness. Since the ice thickness distribution can be altered by the opening of leads, in regions of divergence, or ridging, in regions of convergence, ice dynamics should be properly included in climate model studies of the Arctic.

Of the terms in the ice momentum equation, most of the uncertainty lies in the formulation of the internal ice stress term and in the wind and ocean forcing on the pack ice. A lot of attention has been placed (and still is) on the proper modelling of the internal ice stress term (rheology) which involves the derivation of constitutive relations that try to capture the important features of sea-ice deformation under applied load (Hibler, 1979; Flato and Hibler, 1992; Tremblay and Mysak, 1997). In this note, however, we will concentrate on the wind and ocean forcing terms. In most previous studies (Hibler, 1979; Flemming and Semtner, 1991; Flato and Hibler, 1992; Holland *et al.*, 1993), a square drag law with constant drag coefficient is used to model the air-ice and ice-water stresses. However, more recent measurements have demonstrated that the wind drag coefficient can vary widely depending on the ice surface roughness and presumably, also on the atmosphere stratification (Smith, 1990). Anderson (1987) also found large variations in the measured drag coefficient in the ice-edge region which depended on the ice concentration. In the present study, the effects of including ridging-related surface roughness in the air-ice and water-ice drag parameterization is presented.

In section 2, a brief description of the model used for this simulation is given, and in section 3, supporting evidence for using a variable drag coefficient for modelling studies in the Arctic is presented. In section 4, the sea ice thickness winter climatology obtained from a 10-year integration for both constant and roughness-dependent drag coefficients are compared with submarine sonar data. The main conclusions drawn from the simulation results are summarized in the last section.

D.2 Model description

The sea-ice model is forced with prescribed atmospheric temperatures, winds and ocean currents. In the ice momentum equation, the acceleration term is neglected, i.e., the ice is assumed to be in balance with the external forcing. For this reason, a 5-day running mean of the daily varying winds are used. The constitutive relations used in this model are derived assuming the ice behaves as a large-scale granular material with no cohesion (Tremblay and Mysak, 1997). In particular, ice is considered to have no resistance to tensile forces, a fixed resistance to a compressive load which is a function of ice thickness, and shear resistance proportional to the local internal ice pressure. A single-layer thermodynamic model with a linear internal temperature profile is used for the sea ice. The surface energy flux between the ice-ocean surface and the atmosphere includes latent and sensible heat components, as well as shortwave and longwave radiation. In the present model the ocean is allowed to warm up even though ice is present in a grid cell. The transfer of heat between the ocean and the ice is achieved through sensible heating in a similar manner as between the ice and the atmosphere. A detailed description of the model is given in Tremblay and Mysak (1997).

D.3 Drag law parameterization

The drag coefficients can be calculated from direct stress measurements (u'w') or from wind measurements assuming a specific structure of the planetary boundary layer. The air-ice and ocean-ice stresses are usually modelled as a quadratic law with constant turning angle (McPhee, 1975) as follows:

$$\begin{aligned}
\boldsymbol{\tau}_a &= \rho_a C_{da} |\boldsymbol{u}_a^g| \ (\boldsymbol{u}_a^g \cos\theta_a + \boldsymbol{k} \times \boldsymbol{u}_a^g \sin\theta_a), \\
\boldsymbol{\tau}_w &= \rho_w C_{dw} |\boldsymbol{u}_i - \boldsymbol{u}_w^g| \ \Big[(\boldsymbol{u}_i - \boldsymbol{u}_w^g) \cos\theta_w \\
&\quad + \boldsymbol{k} \times (\boldsymbol{u}_i - \boldsymbol{u}_w^g) \sin\theta_w\Big],
\end{aligned}$$

in which ρ_a and ρ_w are the air and water densities, C_{da} and C_{dw} the air and water drag coefficients, $\boldsymbol{u}_a^g$ and $\boldsymbol{u}_w^g$ the geostrophic wind and ocean current, $\boldsymbol{u}_i$ the ice velocity, θ_a and θ_w the wind and water turning angles and $\boldsymbol{k}$ a unit vector normal to the surface. Typical values for C_{da} and C_{dw} are 1.2×10^{-3} and 5.5×10^{-3}, respectively. In the above equation for the wind shear stress, the ice speed is considered small compared to the wind speed and is therefore neglected.

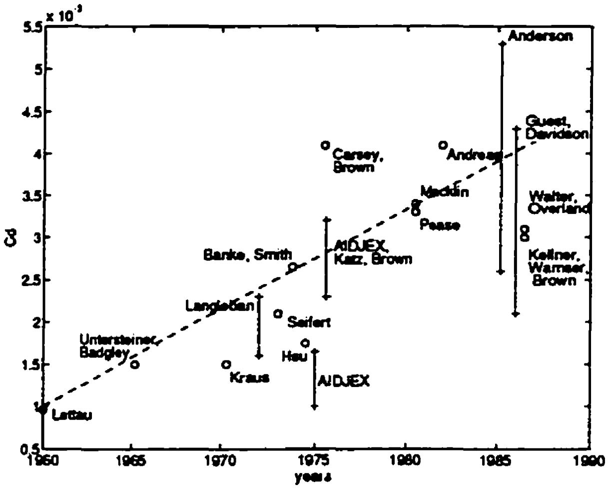

Figure D.1: Drag coefficients over ice from various experiments, reproduced from Smith (1990)

For the atmospheric case, various measurements made over the last 30 years yield drag coefficients ranging from 1 to 6×10^{-3}, with more recent measurements being higher (figure D.1). However, in most sea ice modelling studies, a lower-range C_{da} value of 1.2×10^{-3} is used instead (Hibler, 1979; Flato and Hibler, 1992; Holland *et al.*, 1993) . This choice is based on boundary layer measurements made during the AIDJEX project in 1972 (figure D.1). The increasing trend with time in the measured drag coefficients is due to the measurements being made over increasingly rough surfaces and perhaps under increasingly unstable stratification conditions (Smith, 1990).

In this study, we attempt to include the effect of surface roughness in the drag parameterization; however, we ignore the influence of atmospheric stratification. To zeroth order, we assume that sea ice surface roughness is determined by the ridging intensity. Since ridging results in the buildup of thicker ice, the sea ice surface roughness is assumed to depend on the ice thickness. Stössel and Claussen (1993) have also, among other factors, considered a dependence of the form drag on the ice-plus-snow freeboard. The relation between ice thickness and ridging intensity in the Arctic can be seen by comparing the observed ridging frequency distribution (figure D.2) with the measured ice thickness distribution in the Arctic (figure D.3-c). For the water-ice drag coefficient, the same dependence on surface roughness is assumed.

The lower range of measured drag coefficients (around 1×10^{-3}) commonly used in large-scale sea ice modelling studies are assumed characteristic of one-meter thick ice; the larger range values (around 5×10^{-3}) are assumed to apply to 5-meter thick ice (see figure D.1). Inside those bounds, the drag

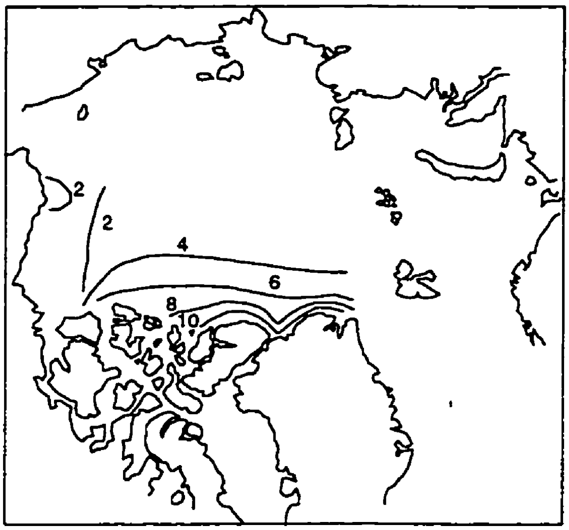

Figure D.2: Number of ridges (larger than 1.22 m) per kilometer in winter, reproduced from Tucker and Westhall (1973)

coefficients are assumed to vary linearly with ice thickness; outside those bounds, the drag coefficients are specified to have these minimum or maximum values. Mathematically, this parameterization can be written as follows:

$$C_{da,w} = C'_{da,w} \begin{cases} 1m, & \text{h} < \text{1m} \\ h, & \text{1m} < \text{h} < \text{5m} \\ 5m, & \text{h} > \text{5m}, \end{cases}$$

in which h is the sea ice thickness and, C'_{da} and C'_{dw} the base drag coefficients taken as 1×10^{-3} and 5.5×10^{-3}, respectively. The linear dependence of C_{dw} on ice thickness h also allows the momentum and continuity equations to be written in terms of the ice flux $u_i h$, which permits the use of more correct boundary conditions (i.e., no normal flux of ice at a solid boundary).

D.4 Results

Results from a 10-year simulation of the sea-ice cover in the Arctic Ocean and surrounding seas are presented in this section. A cartesian mesh with a grid resolution of 111 km is used on a polar stereographic projection of the physical domain. At high latitudes, the variation of the Coriolis parameter with latitude is small and the f-plane approximation is used. The model is forced with the prescribed 1961 5-day running mean of the daily geostrophic winds with its yearly mean replaced by the 1954-89 annual climatology obtained from the NMC sea level pressure analysis (Flato and Hibler, 1992). This provides winds representative of climatology with realistic weekly variability. There is no particular reason for choosing the year 1961 except that it was not an anomalous year in term of sea ice circulation, as were 1969 and 1984, for example. Spatially varying, but steady ocean currents were calculated from a single layer reduced gravity model, appropriate for large scale flows, where the acceleration term in the momentum equation is ignored, friction is represented using a linear drag law, and the normal velocity component is specified at open boundaries. In the Bering Strait, the normal velocity was set to obtain a constant inflow of 1 SV into the Arctic. The inflow and outflow velocity field in the North Atlantic was specified from Levitus sea surface elevation data and scaled in such a way as to obtain no accumulation of water in the Arctic domain. Finally, the solar forcing is the daily average value corrected for an 80 % cloud cover (Laevastu, 1960).

The boundary conditions for the ice dynamic equations are zero normal and tangential velocity at a solid boundary and free outflow at an open boundary (Hibler, 1979). For the sea ice thermodynamic equation, the atmospheric temperature is specified from monthly climatology. The temperature at a given day is calculated as a weighted average of the mid-month climatological values. These temperatures were calculated from the NMC 850 mb height and temperature fields, assuming a linear temperature profile between the 1013 mb and 850 mb levels. For the ocean, the temperatures at open boundaries are specified from monthly climatologies extracted from the Levitus data. At continental boundaries, the ocean heat flux is considered zero (a continent is regarded as a perfect insulator).

The model was integrated for 10 years to reach a stable seasonal cycle using a 1-day time step. To isolate the effects of the drag law parameterization on the simulated thickness distribution fields, the same ocean currents and atmospheric temperature fields are used in the simulations. The results shown are the simulated winter climatological thickness distributions using a constant and a thickness dependent drag coefficient. The model results are compared with sonar data for ice thickness.

D.4.1 March ice thickness and ice-edge position

Figure D.3-a shows the simulated winter climatological thickness distributions in the Arctic using a constant drag coefficient, which can be compared with the sonar measurements (figure D.3-c) reported by Bourke and Garrett (1987). The ice edge position, defined as the 5-tenth ice concentration contour, is also included in these figures. The model contour line patterns reproduce the observations reasonably well, with ice thickness ranging from 1 meter near the Asian continent, to 7 meters north of Greenland. In the Laptev and East Siberian seas, the simulated ice thickness (2-3 m) is larger than observed (< 1m). The modelled ice free region in the North Atlantic extends over the whole Norwegian and Barents seas due to the advection of warm water by the Norwegian Current. In the winter, whether the Bering Strait is open or closed has a strong influence on the ice thickness distribution in the Chukchi Sea.

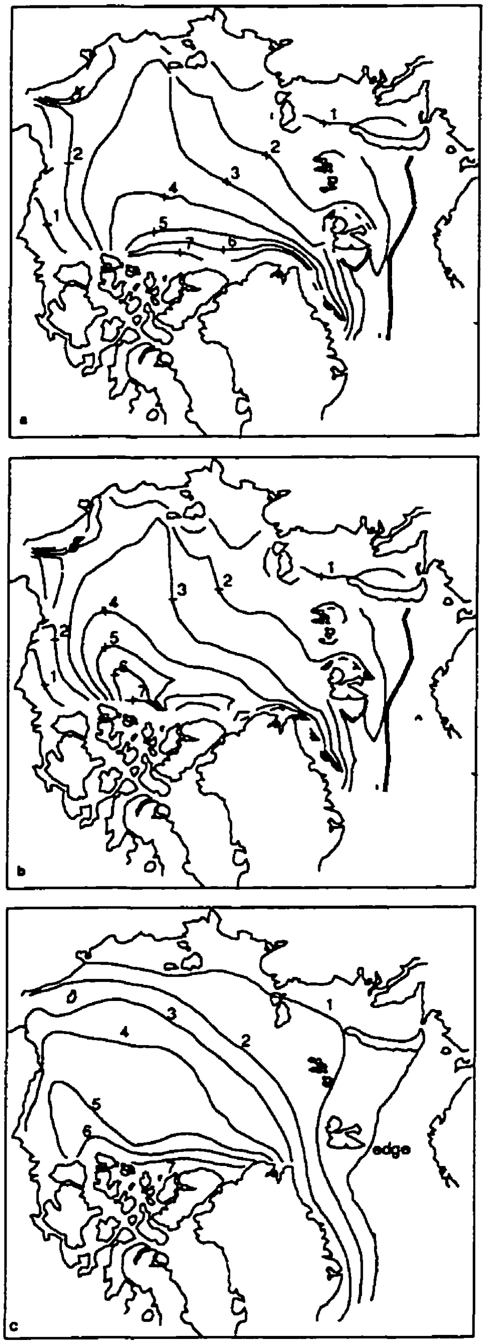

Figure D.3: Simulated March ice thickness distribution with constant (a) and roughness-dependent (b) drag coefficient, and observed ice thickness from sonar data (c), in meters. In (a) and (b), the ice edge is shown as a broad black line.

When open, the resulting ocean current pattern produces significantly thicker ice north of the Bering Strait. However, the temperature of the water entering the domain is very close to freezing point and thus does not have a significant influence on the growth of ice in this region. In the Barents Sea, the ice margin is very well reproduced; however, in the Greenland Sea the ice edge is too far east. This is due to the prescribed ocean currents which have a weak recirculation of water in the Greenland Sea.

Figure D.3-b shows the simulated mid-March thickness distribution in the Arctic using a roughness dependent drag coefficient as described in the previous section. In this simulation, the ice thickness also ranges from 1 to 7 meters, as before. However, now the ice thickness spatial distribution poleward of the northern Canadian Islands is significantly different and is in better agreement with the observations. In this region, the ridging activity is high and the ice is assumed rough; this results not only in a higher wind stress but also in ice drift following the wind more closely (ratio of water drag to Coriolis effect is higher). Both of these effects contribute to a higher ice buildup against the western part of the northern Canadian coast, as observed in the thickness field (figure D.3-c). In thinner ice regions the roughness-dependent drag coefficients approach the minimum value and little difference in the thickness distribution is found for the two models.

D.5 Conclusions

In the present study, ice surface roughness is assumed to increase with ridging intensity, which in turn is responsible for ice thickening. Consequently, the drag coefficients are considered proportional to ice thickness. The effects of the atmospheric stability on the air-ice momentum transfer, however, is not considered.

A long term integration of the sea ice model with both a constant and roughness dependent drag coefficient yield a range in ice thickness in good agreement with ice observations. However, the ice thickness spatial distribution in the Canada Bassin for the two simulations is significantly different. The results using a constant drag coefficient yield a more uniform thickness buildup against the northern Canadian islands whereas, the results using the roughness dependent drag coefficient results in an offshore tongue of thicker ice in the western Arctic; this is in better agreement with the thickness observations. In general, the simulations show that spatially varying drag coefficients, within the range of observed values, have a strong influence on the calculated ice thickness distribution, and an attempt to incorporate this effect into sea ice modelling studies is desirable.

IMAGE EVALUATION TEST TARGET (QA-3)

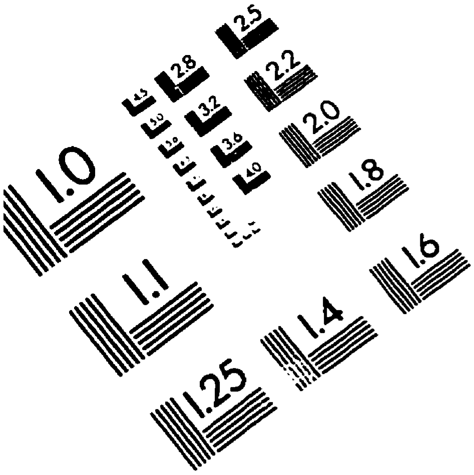

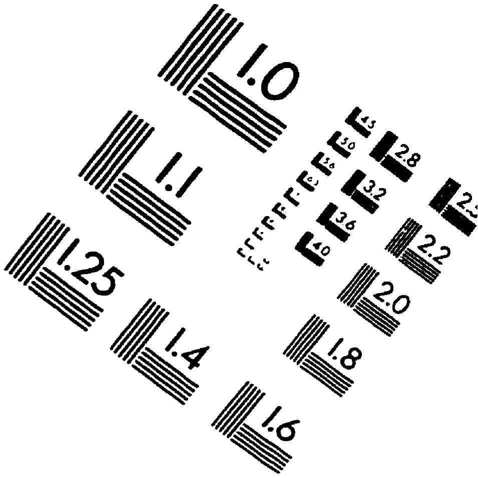

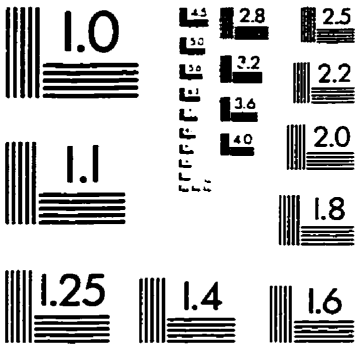

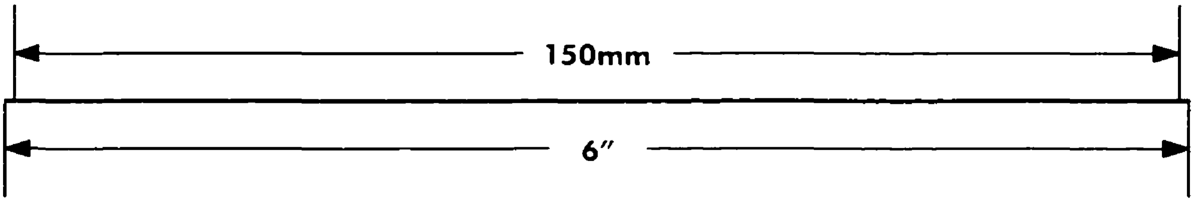

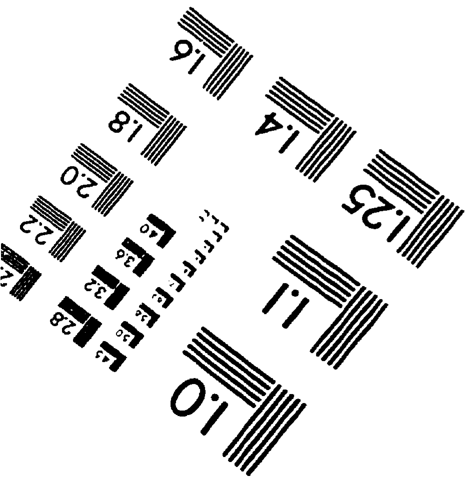

APPLIED IMAGE . Inc
1653 East Main Street
Rochester, NY 14609 USA
Phone: 716/482-0300
Fax: 716/288-5989